GENESIS AND EXPLORATION POTENTIAL FOR EOCENE AGE VEINS OF THE ORO FINO MINING DISTRICT, DEER LODGE COUNTY, MONTANA

Stanley L. Korzeb and Kaleb C. Scarberry

Montana Bureau of Mines and Geology, Butte, Montana

MBMG

Montana Bureau of Mines and Geology

GENESIS AND EXPLORATION POTENTIAL FOR EOCENE AGE VEINS OF THE ORO FINO MINING DISTRICT, DEER LODGE COUNTY, MONTANA

Stanley L. Korzeb and Kaleb C. Scarberry

Montana Bureau of Mines and Geology, Butte, Montana

Montana Bureau of Mines and Geology

TABLE OF CONTENTS

FIGURES

TABLES

PLATES

ABSTRACT

The Butte Granite of the Boulder Batholith hosts the Oro Fino mining district epithermal veins. Age dating indicates the veins developed 45.26 ± 0.11 Ma after Eocene Lowland Creek volcanism eruptions ended at 48.6 Ma. Lowland Creek volcanism and development of the epithermal veins took place in a back-arc environment. The veins have features found in both epithermal low and intermediate sulfidation systems. Alteration contains adularia, sericite, illite, kaolinite, and pyrite with quartz and chalcedony, which is characteristic of both low and intermediate sulfidation veins.

 Cathodoluminescence imaging revealed four quartz stages; electron microprobe analysis indicated a variable Al concentration. First and second stage vein quartz was found to have elevated Al concentrations (1,888–11,802 ppm), indicating acidic conditions found in higher sulfidation levels than low sulfidation systems. Third and fourth stage vein quartz had a variable Al concentration (0–3,441 ppm), indicating variable basic to acidic conditions expected in low sulfidation systems. Fluid inclusions from the third and fourth quartz stages showed the hydrothermal fluids evolved from the mixing of magmatic and meteoric fluids, boiling, and ranged from low to high salinity. Magmatic sourced fluids had an elevated CO_2 concentration, low salinity (1.6 wt% NaCl eq), and high temperature (442ºC). Mixing of the magmatic fluid with meteoric fluid and boiling drove out the CO_2, lowered the temperature (129º–346ºC), caused wide ranges in salinity (0.0–37.7 wt% NaCl eq), and varied the pH from acidic to basic. Fluid inclusion salinity and temperature ranges fell within the range for low to intermediate sulfidation systems. Lithostatic pressure estimated from fluid inclusion data ranged from 0 to 150 bars, indicating the hydrothermal system was shallow and formed up to 0.8 km below the paleo surface.

Base metal and silver–gold mineralization took place simultaneously with third and fourth stage vein quartz precipitation caused by boiling and changing pH conditions. Most bladed calcite in the veins is pseudomorphed by quartz, indicating a downward boiling front, which caused silver minerals to be telescoped over base metal minerals. Late stage mineralization characterized by fluorite and baryte followed silver–gold mineralization. The last mineralizing stage was supergene alteration of the primary minerals.

Trace elements from the altered host granite and quartz veins are characteristic of epithermal veins and indicate the veins were silver dominated. The presence of As, Sb, and Tl are conducive to a shallow low to intermediate sulfidation epithermal system. Sulfur isotope data from early pyrite and chalcopyrite showed a depletion to minor enrichment (-2.7‰ to 1.2‰), indicating a magmatic influence on the early hydrothermal fluids. Later pyrite and chalcopyrite showed an enrichment in $\delta^{34}S$ (3.6‰ to 8.5‰), indicating vein development from a hydrothermal fluid influenced by crustal contamination. A potential source for the enrichment of $\delta^{34}S$ could be Proterozoic Belt Supergroup sediments.

INTRODUCTION

The Oro Fino mining district is located 6 mi east of Galen and extends south to the boundary between Deer Lodge and Silver Bow Counties. The district was chosen for this investigation because the mineral resource genesis is not fully understood, the district was not studied in detail by past investigations, it has potential for future minerals exploration, and Elliot and others (1993) gave the district a moderate to high potential for undiscovered porphyry/stockwork copper–molybdenum deposits and disseminated/stockwork gold and silver deposits. The assessment by Elliot and others (1993) is based on published and unpublished sources and studies consisting of geologic mapping, geochemical and geophysical surveys, remote sensing, geochronologic studies, and examination of mines and prospects. Past mining produced gold and sapphires from placer deposits and gold, silver, copper, lead, and zinc from epithermal quartz veins. Some veins have not been fully explored or developed along strike and at depth.

The goal of this investigation was to update and generate new geologic data on the known mineral resources and assess the exploration potential for the district. New data were generated using stable isotope analyses, trace element and whole-rock geochemistry, geochronology, alteration petrography, fluid inclusion measurements, and cathodoluminescence analysis of vein quartz. From the geologic data, we developed genetic models of the mineral resources and assessed exploration potential.

METHODS

Methods used for this investigation involved sampling dumps and stockpiles of the existing mines because underground workings were inaccessible. Vein outcrops were mapped and sampled along with associated altered host rocks. Samples were analyzed for alteration types, fluid inclusions, stable isotopes, mineralogy, trace element, whole-rock geochemistry, and cathodoluminescence analysis. An aplite dike was dated by U/Pb in zircon. Altered host rock was dated by $^{40}Ar/^{39}Ar$ methods from sericite. Hand samples collected from past and present investigations were used for mineral identifications.

PREVIOUS INVESTIGATIONS

The first published account of the Oro Fino mining district was by Pardee and Schrader (1933). They described the Dry Cottonwood Creek gold and sapphire placer mines and the history of the Champion mine. Pardee and Schrader (1933) also described the Last Resort, St. Louis, and Jackpot mines, which were examined by J.T. Pardee in 1911. After Pardee and Schrader (1933) published their account, Williams (1951) completed a thesis covering the district. Williams (1951) described the geology, production, and history of the major mines and mapped the geology of the Oro Fino mining district. Following the work by Williams (1951), Berg (2007) published the results of a study on the sapphire placer mines located along South Fork of Dry Cottonwood Creek. Part of the Oro Fino mining district geology is included in the geologic map of the Lockhart Meadows quadrangle mapped by Hargrave and Berg (2013).

MINING HISTORY

Gold-bearing placers along Caribou, Oro Fino, and Dry Cottonwood Creeks were the first deposits to be discovered and mined in 1867. Placer mining continued until 1870 and started declining in favor of the newly discovered lode veins (Williams, 1951). Alluvial sapphires were discovered in 1889 in the upper portion of the South Fork of Dry Cottonwood Creek (Williams, 1951; Berg, 2007). Commercial operations began in 1907 with the construction of a dredge by the Variegated Sapphire Company of Butte (Williams, 1951; Berg, 2007). The dredge operated until 1911 and later in 1914 (Berg, 2007). The sapphires were sold to the American Gem Syndicate for watch bearings (Berg, 2007). Another dredge was operated in 1910 to 1911 by the Consolidated Gold & Sapphire Mining Company (Pardee and Schrader, 1933; Williams, 1951; Berg, 2007). These dredging operations produced mostly gold, which paid for the operating costs. The dredges operated on gravel deposits near the head of Dry Cottonwood Creek and in Grand Pre Flat (Pardee and Schrader, 1933).

Few of the recovered sapphires were suitable for gems, but they were suitable for instrument mechanisms. Pardee and Schrader (1933) reported that the predominant colors varied from deep to light aquamarine, and pale yellowish green. Other colors can be clear, smoky blue, light and dark topaz yellow, straw yellow, light and dark pink, and ruby red. When gold production began to decline and synthetic sapphires were introduced to the instrument market in the 1920s, the operations were shut down because the value and demand for sapphires could not maintain a profitable operation (Williams, 1951; Berg, 2007).

Interest in sapphires was renewed in 1994–1995 by American Gem Inc., who contracted with Watts, Griffis, and McQuat to test sapphire-bearing gravel

along the South Fork of Dry Cottonwood Creek (Berg, 2007). American Gem Inc. began mining sapphires in 1995 for the gemstone market and discontinued mining in 1996 (Berg, 2007). Gem River Corp. began mining sapphires for the gem trade in 1996 from Grand Pre Flat and continued until 1998 (Berg, 2007). Jim and John Rex mined sapphires from stockpiled gravel by American Gem Inc. during the summer of 2000 (Berg, 2007). Sapphire mining ended in the Oro Fino mining district with the termination of the American Gem Inc. operation in 2000.

The first lode deposit to be mined was the Champion mine located at the head of Oro Fino Creek near the Continental Divide. During 1886–1888, the Champion mine produced a small amount of ore that was processed at a mill on Peterson Creek near Deer Lodge (Pardee and Schrader, 1933; Williams, 1951). Operating the mine proved to be unprofitable due to the expense of hauling ore to the mill, causing the mine to close in 1888 (Pardee and Schrader, 1933; Williams, 1951).

Lode mining resumed in 1916 when a small quantity of gold and silver ore was shipped from the Independence mine. Later in 1918 and 1919, oxidized copper ore was shipped directly to the smelter from the Independence mine (Williams, 1951). Interest was renewed in the Champion mine in 1919 when the Butte Jardine Metals Company acquired the mine (Trauerman and Reyner, 1950; Williams, 1951). A 100 ton per day flotation mill was built in 1920 at the Champion mine and operated until 1923 (Pardee and Schrader, 1933; Trauerman and Reyner, 1950). The mill produced 30,000 tons of concentrate in 1922. Production for the years 1920, 1921, and 1923 was reported by Pardee and Schrader (1933) to be several hundred tons of either ore or concentrate. Williams (1951) reported that 9,000 tons of milling ore was shipped from the Champion mine in 1924. The mine was a predominant silver producer and shut down by 1926 due to low silver prices (Pardee and Schrader, 1933).

In 1924, ore was shipped from the Cashier claim for the first time. Three shipments of silver ore with minor amounts of gold were produced during 1927 and 1928 from the Oro Fino district (Williams, 1951). The Cashier and Independence mines were the only mines in production in 1929 and 1930. The Fairview Mining Company was operating the Independence mine in 1931 using a pan amalgamation process. Bullion being produced from this operation was sold as test lots. During the same year the Banker leasing company was shipping silver ore from the Joker Fraction group (Williams, 1951). The Independence mine was the only mine producing in 1933, shipping test lots of bullion (Williams, 1951). In 1938, the Champion mine was leased and reopened, and by 1940 the operating mines in the district were the American, Cashier, Grizzly Bear, Independence, and Champion (Williams, 1951).

Production

Production from 1867 to 1870 came from gold placers and was estimated to have a value of $80,000 (1800s gold price of $20.67; Williams, 1951) and was calculated to be approximately 3,870 oz. Production was not recorded from 1866 to 1911, but both lode and placer mines were operating. From 1916 to 1926, production was reported by Williams (1951) to be from the Champion, Independence, and Cashier Group mines and was estimated to total $350,000 (based on early 1900s prices for gold, silver, lead, zinc, and copper). Accurate production records were not reported until after 1933 and are summarized in table 1.

Table 1. Oro Fino production from 1933 to 1948 summarized by Williams (1951) from the Mineral Yearbook for the years 1933 to 1950.

Year	Producing Mines	Tons of Ore	Oz. Gold	Oz. Silver	Lbs. Copper	Lbs. Lead
1933	3	68	21	1,053	64	—
1934	3	22	9	2,183	16	—
1935	2	8	2	280	—	—
1936	8	158	83	3,854	265	200
1937	—	—	—	—	—	—
1938	3	105	21	1,383	112	—
1939	4	346	161	4,262	—	—
1940	4	1,429	131	16,252	—	—
1941	2	1,176	55	17,564	—	—
1942	2	518	10	4,815	1,000	—
1947	2	15	1	378	—	—
1948	1	3	—	94	—	—

Champion Mine

Historical records on the Champion mine are maintained at the Montana Bureau of Mines and Geology (MBMG) archives and are the source for the following. The largest mine in the district is the Champion mine, which was controlled by the Champion Silver Mining Company. The Champion mine was leased and operated by the Butte Jardine Metals Company until 1925, when an earthquake collapsed the underground workings, and by 1926 low silver prices caused the mine to close. At this time, the company owed the Anaconda Company $100,000; to cover the debt, the mine was quit-claim deeded to the Anaconda Company. The Anaconda Company did not operate the mine and leased the mine in 1938 for a few years. Interest was resumed in 1963 when the original owner leased the property from the Anaconda Company.

The Champion Silver Mining Company then began reopening the 600 level and drilled two diamond core holes. From the 600 level, they developed the vein to the 900 level. By 1966, new stope and drift development produced 3,966 tons of ore that was shipped to the Anaconda smelter. Grade of the ore varied from 2.8 to 31.56 oz/ton silver and from 0.015 to 0.127 oz/ton gold. The silver grade averaged about 10 to 15 oz/ton, which is similar to the ore shipped from 1918 to 1925. The Champion Silver Mining Company reported the mine was on standby in 1967 and could not ship ore to the smelter until the copper strike was settled. By 1969 the company was running short on funds and the last reported stockholders meeting was held that year. By 1973, the Orofino Mining Company operated the mine, and shipped 25.45 tons of ore from the dump to the Anaconda smelter, which assayed 3.04 oz/ton silver and 0.0191 oz/ton gold and 80.04 tons of ore that assayed 2.13 oz/ton silver. Anaconda remained the owner of the mine in 1975 and it was still under lease by the Champion Silver Mining Company. By the mid-1970s mining operations ended in the Oro Fino district. Today (2020), the patented mining claims covering the Champion mine and elsewhere in the district are owned by private individuals who use the properties for recreation. On some of the patented claims covering other veins in the district, vacation homes or cabins were constructed.

REGIONAL GEOLOGY

The mining district lies within the west side of the Boulder Batholith and is adjacent to the Lowland Creek volcanic field (fig. 1). The Boulder Batholith and Elkhorn Mountains volcanic field concurrently formed during crustal shortening near the end of Mesozoic Cordillera arc magmatism between about 85 and 76 Ma (Mahoney and others, 2015; Rutland and others, 1989). The eruption of the Elkhorn Mountains volcanic field was the first magmatic event in the region during continental arc magmatism and is preserved along the west and east flanks of the Boulder Batholith (fig. 1). Based on regional rock exposures, Smedes (1966) estimated the original thickness of the Elkhorn Mountains volcanic rocks to be 4.6 km. Elkhorn Mountains eruptions started with fissure eruptions of andesitic lava that filled and overflowed the edges of a broad N35°E-trending, regional syncline (Klepper and others, 1957; Smedes, 1966). Overlying the early andesite beds is a middle member consisting of two massive tuff and tuff breccia units on the west flank of the Boulder Batholith (Scarberry, 2016). On the east flank of the Boulder Batholith the middle member consists of three dacite ignimbrite sheets capped by two thin pyroclastic units (Scarberry and others, 2016). The upper unit is represented by bedded and water-laid tuff forming conglomerates and mudstones. Occurring locally are lenticular beds of fresh-water limestone and andesitic flows (Klepper and others, 1957). Diorite stocks, dikes, and sills fed the Elkhorn Mountains volcanic field, and some diorite bodies may be subvolcanic rocks recrystallized during emplacement of the Boulder Batholith (Klepper and others, 1957).

Plutonic intrusions that developed the Boulder Batholith began approximately 81 Ma and continued until approximately 74 Ma (Lund and others, 2002). From aluminum-in-hornblende barometry studies of Butte Granite, Houston and Dilles (2013) suggested the Boulder Batholith crystallized at a depth of 6–9 km where the Butte mining district is located. The batholith is elongate in a northeast–southwest direction, and is about 90 km long and 50 km wide. Depending on structural control of pluton emplacement, the plutonic rocks are subdivided into two groups, an early stage and a younger Butte Granite stage (Berger and others, 2011). The early stage plutonic rocks span an interval of about 81–76 Ma and the Butte Granite stage was emplaced about 75–74 Ma (Lund and others, 2002). Emplacement of the early stage magmas took place concurrently with superjacent thrust faulting and related folding. The Butte Granite was likewise structurally controlled and follows pre-Butte Granite thrust faulting (Berger and others, 2011). Butte Granite magmatism closed with the emplacement of pegmatite, alaskite, and aplite dikes (Berger and others, 2011).
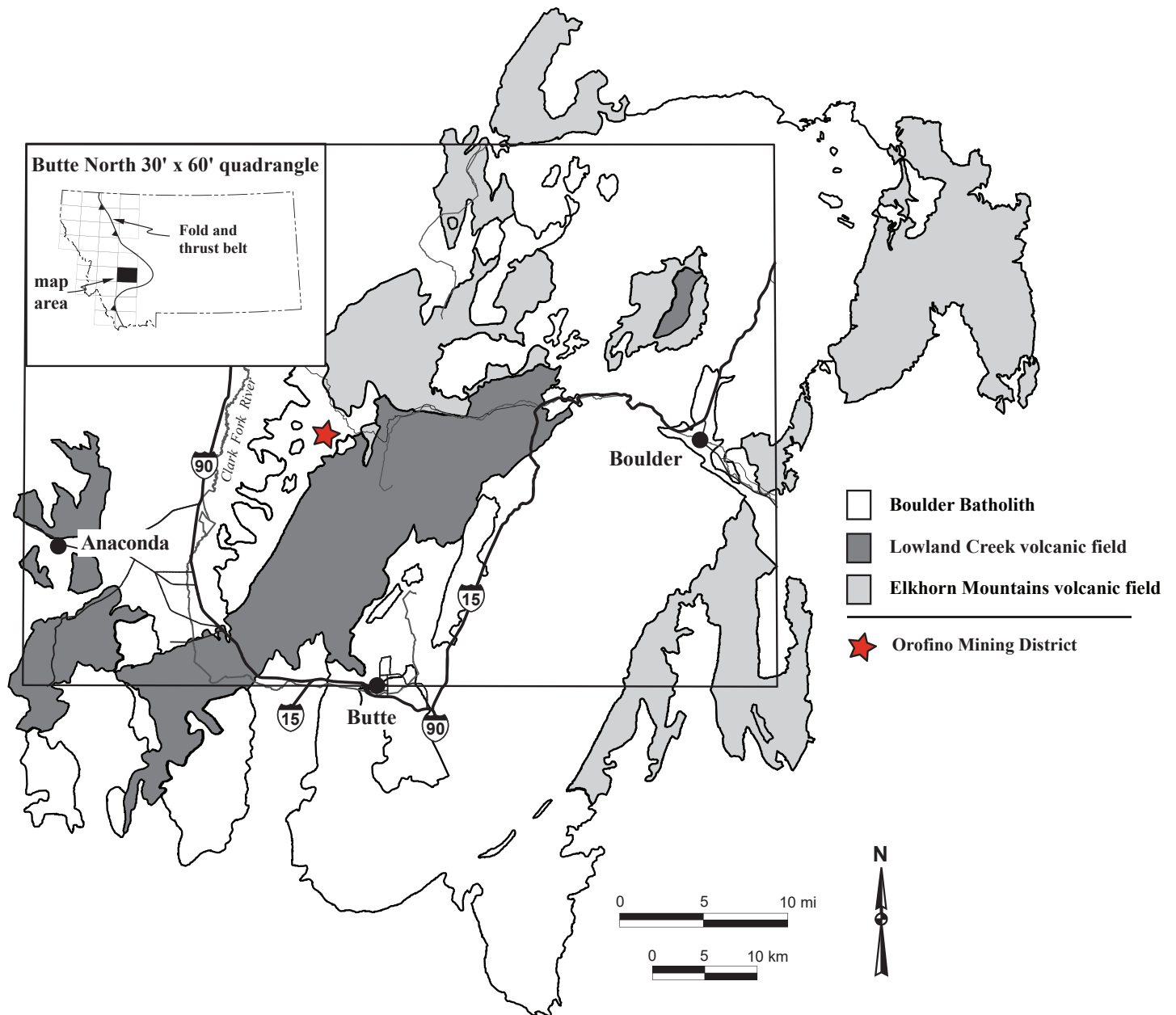
Figure 1. Generalized geologic map of the Boulder Batholith showing location of the Oro Fino Mining district and volcanic field locations.

After the Boulder Batholith was emplaced, a combination of Laramide, Eocene crustal extension, and Basin and Range faulting caused the Elkhorn Mountains volcanic field and Boulder Batholith to be uplifted, eroded, and exhumed. Between about 65 and 55 Ma, Laramide crustal shortening from the west occurred, forming grabens in the upper plate of the Anaconda Metamorphic Core Complex detachment. The grabens were later filled with the Lowland Creek volcanic field between 53 and 49 Ma (Scarberry and others, 2015; Dudás and others, 2010).

Back-arc volcanism started during the early Eocene, caused by the steepening of the subducting Farallon plate under the North American plate (Feely,

2003), and leading to the eruption of the Lowland Creek volcanic field. The Lowland Creek volcanic field was erupted in a northeast–southwest half graben traversing the Boulder Batholith (fig. 1; Sillitoe and others, 1985; Dudás and others, 2010). The volcanic field is bounded on the southeast by a normal fault that displaces the Boulder Batholith downward on the northwest side of the fault (Smedes, 1962; Foster, 1987). The eastern limit of the volcanic field is defined by Smedes (1962) to be a fault scarp barrier that formed during eruption of the volcanic rocks. The thickest portion of the Lowland Creek volcanic field accumulated in a depressed area west of the fault scarp (Smedes, 1962). A northeast-trending fault

mapped by Williams (1951) defines the west limit of the volcanic field. The northeastern end of the graben is defined by the Butte Granite, rhyolite, and quartz latite intrusions (Smedes, 1962).

The stratigraphy of the Lowland Creek volcanic field is complex and consists of assemblages of strata, lentils, tongues, and flows of similar lithology (Smedes, 1962; Hargrave, 1990; Hargrave and Berg, 2013). Smedes (1962) divided the Lowland Creek volcanic field stratigraphy into six laterally discontinuous units representing two depositional cycles. The lowest cycle is composed of volcanoclastic sedimentary rocks and tuffs and tuff breccias and the upper cycle is lava flows (Dudás and others, 2010). The volcanoclastic debris or basal unit is overlain by moderately welded ash-flow tuff. The lower tuff sequence is overlain by an upper densely welded ash-flow tuff unit. Foster (1987) suggests the upper ash-flow tuff sequence was erupted from a northeast-trending cauldron. Structures bounding the cauldron are high-angle, northeast-trending faults that juxtapose intra cauldron upper tuffs against the Boulder Batholith and lower tuff sequence. Later eruptions from single vent volcanos deposited intermediate-composition lavas over the upper ash-flow tuff unit (Foster, 1987).

During and after the Lowland Creek volcanism, core complex extension continued until about 35 Ma (Lonn and Elliott, 2010). Basin sedimentation began near the close of Lowland Creek volcanism at 50 Ma (Portner and others, 2011). The Lowland Creek volcanic field is overlain by lacustrine and fluvial sedimentary rocks in the Deer Lodge and Warm Springs Creek Valleys and is locally unconformable with the volcanic rocks (Dudás and others, 2010). Basin and Range block faulting (Reynolds, 1979) and related transfer faults (Scarberry and Smith, 2014) have controlled sedimentation in the Deer Lodge Valley since 15 Ma. Tertiary volcanism took place north of the study area about 46–30 Ma near Avon and is referred to as the Avon volcanic field (Mosolf, 2015). Pleistocene–Holocene alpine glacial deposits occur along many of the ridges adjacent to the Continental Divide (Derkey and others, 2004).

DISTRICT GEOLOGY

The entire Oro Fino district lies within the Butte Granite of the Boulder Batholith and is the host rock for the epithermal veins (fig. 2 and plate 1). The district was included in a geologic map east of Warm Springs, Montana produced by Williams (1951). The east half of the district is included in the 1:24,000-scale Lockhart Meadows geologic map

generated by Hargrave and Berg (2013). The following discussion is a compilation of these two maps, geologic investigations of the Boulder Batholith, and field observations.

On top of Cottonwood Mountain, Orofino Mountain, and at the head of Oro Fino Creek, the Butte Granite is overlain by rhyolite that is part of the Elliston volcanic field and attributed to the Avon volcanic event (plate 1; Hargrave, 1990; Hargrave and Berg, 2013; Mosolf, 2015). The veins occupy northeast and north–south-trending faults and fractures in the Butte Granite (fig. 2 and plate 1) that probably coincide with the formation of the northeast-trending partial graben and the eruption of the Lowland Creek volcanic field. The veins show evidence of the original faults being open fractures consisting of open space filling and altered brecciated Butte Granite assimilated into the quartz veins. Epithermal veins adjacent to aplite dikes likewise consist of open space filling with assimilated and altered brecciated aplite and Butte Granite.

GEOCHRONOLOGY

Zircons from an aplite dike adjacent to the Amanda vein at location OF-79 (fig. 2) were dated at the Boise State University Isotope Geology Laboratory. Conventional density and magnetic methods were used to separate the zircon crystals from the aplite hand sample. The zircon separate was annealed in a muffle furnace at 900°C for 60 hours. After annealing, individual zircon crystals were selected, mounted, polished, and imaged by cathodoluminescence (CL) on a scanning electron microscope. From the CL images, 54 locations for spot analysis by laser ablation-inductively coupled plasma mass spectrometry (LA-ICP-MS) were selected based on the crystals yielding Cretaceous ages. LA-ICP-MS analysis utilized an X-Series II quadrupole ICP-MS and New WaUp-213 Nd:YAG UV (213 nm) laser ablation system. An external standard AUSZ2 was used during the analytical session (Rivera and others, 2013: Kennedy and others, 2014).

Zircons extracted from the aplite are predominantly luminescent, sector and oscillatory-zoned crystals with variable thickness rims of non-luminescent zircon (fig. 3). A minority of grains are non-luminescent zircons. LA-ICP-MS analysis revealed several luminescent crystal cores as Proterozoic; the rest of the crystals yielded Cretaceous ages. Nine spot analyses were rejected as biased by inherited cores on the basis of CL imagery and high within-run variance in U content and Pb/U ratio. The remaining 54 spot analyses yielded a normal distribution with a weighted mean $^{206}Pb/^{238}U$ date of 74.5 ± 0.6 (1.6) Ma with an MSWD = 1.1.

Figure 2. Geologic map of the Oro Fino mining district showing sample and vein locations and rock types. Detailed rock type descriptions are in plate 1.
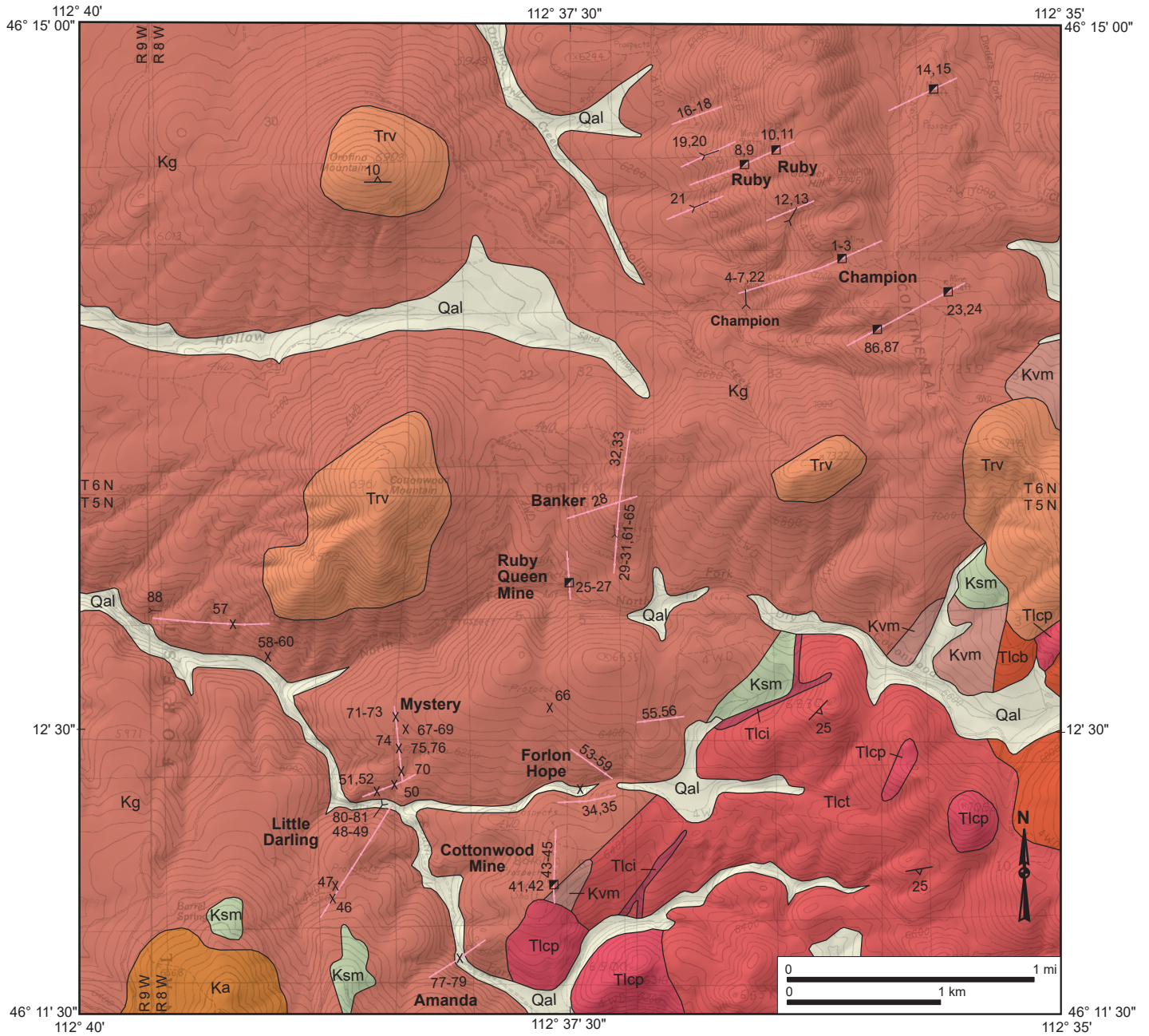
LEGEND

Qal	Alluvium and colluvium
Trv	Rhyolite, undifferentiated
Tlci	Dike
Tlcp	Rhyodacite porphyry lavas
Tlcb	Breccia
Tlct	Rhyolite Tuff
Ka	Aplite
Kg	Butte Granite
Kvm	Metamorphosed volcanic
Ksm	Metamorphosed sedimentary rocks

——	Contact
•—•—•—	Vein
◪	Shaft
⌐	Adit
X	Prospect pit
25 ⌐	Inclined compaction foliation—showing strike and dip

Numbers indicate sample identifiers (see appendix)

For more detailed information see plate 1.

OF-79   M row 2   Scarberry   Montana   March 23, 2015
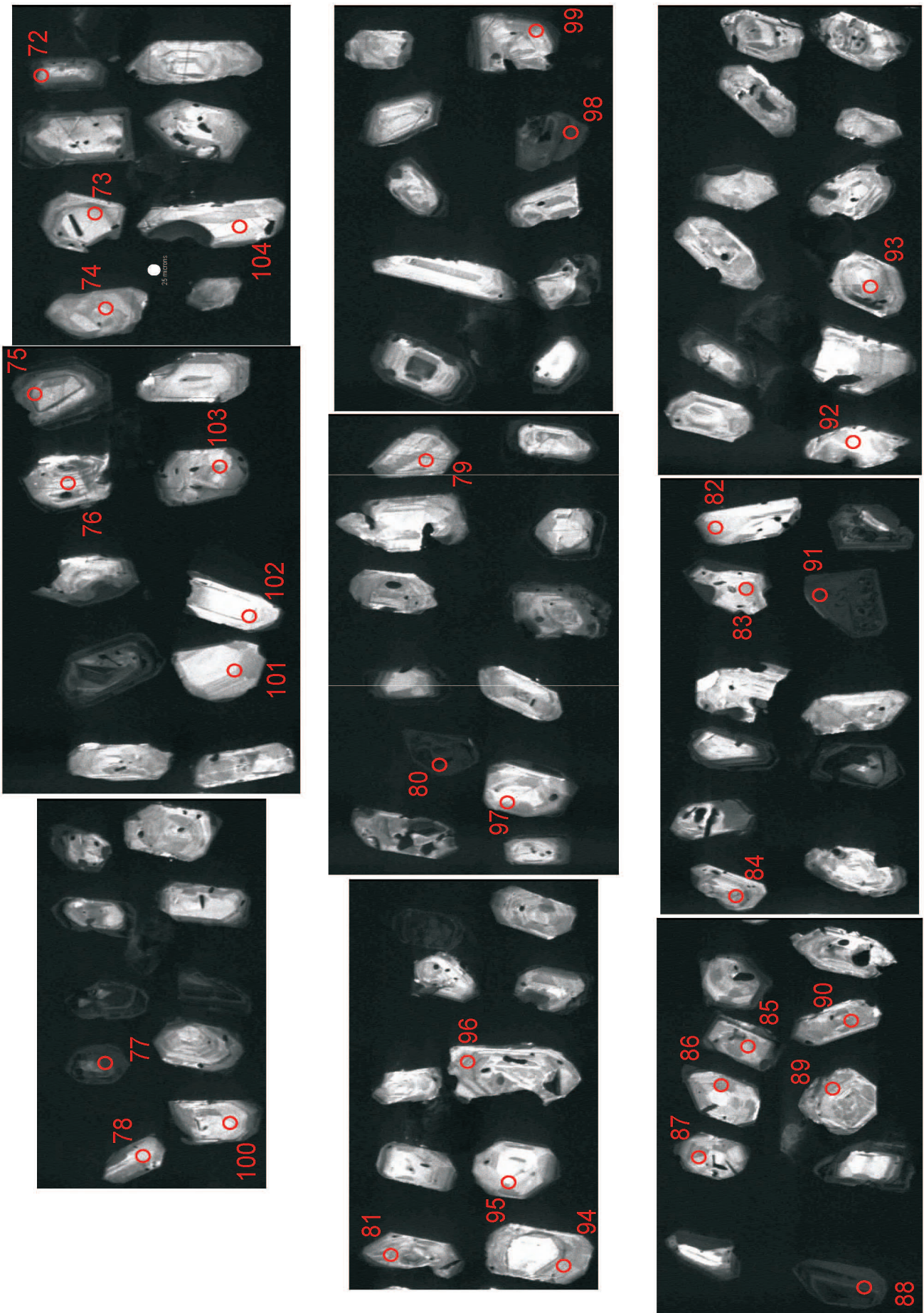
Figure 3. Cathodoluminescence images of zircons extracted from aplite (OF-79) and LA-ICP-MS points.

Hydrothermal muscovite (sericite) from altered Butte Granite host rock adjacent to a vein exposed in the Banker mine, at location OF-31, was dated by $^{40}Ar/^{39}Ar$ methods. Sericite analysis was conducted at the Oregon State University Argon Geochronology Laboratory, Corvallis, OR. Analysis was completed by standard incremental heating at 77-s intervals using an Argus-VI-D instrument. The $^{40}Ar/^{39}Ar$ plateau date for OF-31 was 45.26 ± 0.11 Ma (fig. 4) and is represented by more than five heating steps.

WALL ROCK ALTERATION

Alteration of the Butte Granite occurs adjacent to the quartz veins, consisting of sericite and clays identified from field observations, SEM-EDS analysis, X-ray diffraction analysis, and examination of hand specimens and thin sections. The SEM-EDS analysis was performed at the Center for Advanced Mineral and Metallurgical Processing, Montana Tech. X-ray diffraction analysis was performed at the College of Oceanic and Atmospheric Sciences, Oregon State University.

Silicic alteration is strongest adjacent to the veins incorporating the replaced host granite. Distal from the vein contacts, silicic alteration intensity decreases relative to sericitic-argillic alteration. Alteration extending the furthest from the veins shows minor silicification and sericitic-argillic alteration becomes the dominate alteration type. Sericitic-argillic alteration grades into unaltered granite or aplite host rocks.

Sericitic-Argillic Alteration

Sericitic and argillic alteration overlap and cannot be separated, suggesting they formed at the same time. Sericitic-argillic alteration decreases in intensity outward from the veins into unaltered granite. Adjacent to the veins, disseminated pyrite is concentrated in the sericitic-argillic altered granite along with silicified wall rock. Sericite, consisting of fine-grained muscovite, was identified by X-ray diffraction in the altered

15D34786.AGE >>> OF-31 >>> MONTANA | SCARBERRY

Ar-Ages in Ma
Weighted Plateau
45.26 ± 0.11
Total Fusion
45.87 ± 0.07
Normal Isochron
45.58 ± 0.24

Sample Info
Muscovite
Butte
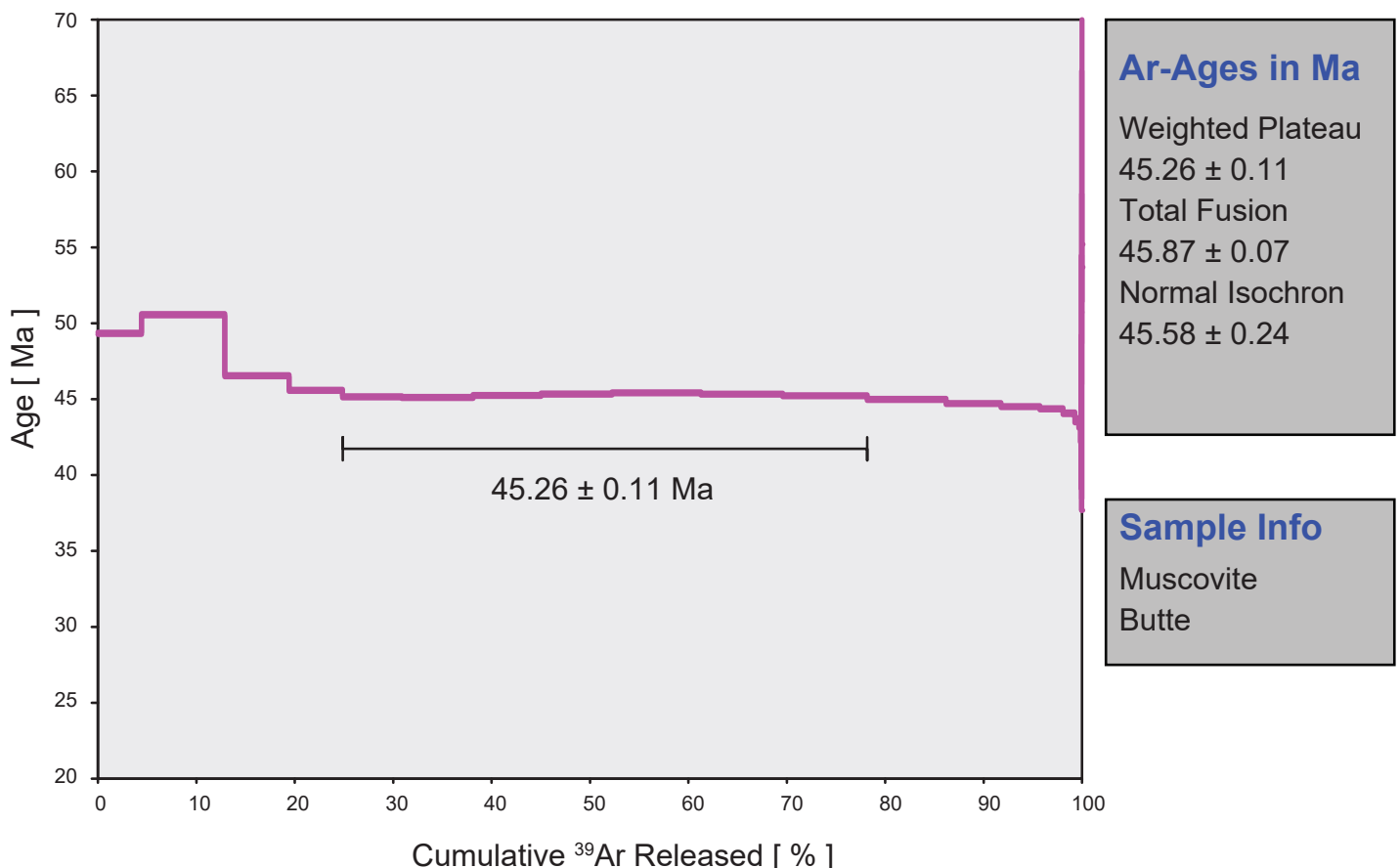
45.26 ± 0.11 Ma

Figure 4. $^{40}Ar/^{39}Ar$ plateau diagram showing heating steps for sample OF-31 from the Banker mine and plateau age of 45.26 ± 0.11 Ma with ±2 σ confidence limit.

granite along with hydrothermal potassium-feldspar (adularia). Illite was the most abundant mineral identified by X-ray diffraction. Identified clay minerals are kaolinite and montmorillonite. In thin section, primary muscovite and feldspar are completely to partially replaced by sericite/illite depending on the degree of alteration. In strongly altered granite, primary quartz grains are all that remains of the original granite.

Silicic Alteration

Adjacent to the veins, silicic alteration overlapping sericitic-argillic alteration is characterized by fine- grained quartz and disseminated pyrite replacing the granite host rock. The silicified host granite is cut by later numerous quartz veinlets. Granite breccia fragments that were incorporated into the quartz veins were also replaced by fine-grained quartz. The intensity of silicic alteration decreases outward from the vein contact into sericitic-argillic altered granite. In thin section, assimilated granite breccia fragments can be rounded with reaction rims of fine-grained quartz replacing the granite. Silicification intensity varies from partial to complete replacement of the host granite. In completely replaced samples, irregular primary brecciated quartz grains remain from the original granite. When partially silicified, the groundmass is replaced by fine-grained quartz, with remaining fractured primary quartz grains and feldspar being partially replaced by illite/sericite.

ALTERATION AND LITHOGEOCHEMISTRY

Samples of unaltered and altered host rock were analyzed for whole-rock oxides and trace elements. Thirteen samples were analyzed by fusion/X-ray fluorescence methods for oxides and 15 samples were analyzed for 48 trace elements by four acid digestion ICP-MS methods. ALS Minerals Inc. performed the whole-rock and ICP-MS analysis. The procedure for whole-rock analysis consisted of a lithium borate fusion followed by X-ray fluorescence analysis. Results are given in weight percent oxide, shown in table 2. For trace elements, the sample is subject to a four acid digestion followed by ICP-MS analysis for 48 elements with results reported in parts per million (ppm).

To delineate unaltered and altered rocks, the Ishikawa alteration index (AI) and chlorite–carbonate–pyrite index (CCPI) were determined. The AI defines the intensity of sericite and chlorite alteration such that fresh rock AI is about 50 and complete replacement of feldspars by sericite and/or chlorite is represented by an AI of 100 (Large and others, 2001). The CCPI measures the degree of chlorite alteration from replacement of albite, K-feldspar, and sericite (Large and others, 2001). Large and others (2001) determined the CCPI is increased by Mg-Fe carbonate alteration and pyrite, magnetite, or hematite enrichment. The CCPI is also strongly affected by magmatic fractionation and primary composition variations of rock types (Large and others, 2001), which can result in different values for granite and aplite.

Table 2. Whole-rock analysis for altered and unaltered granite and aplite.

Sample Number	Alteration Type	Al_2O_3 %	CaO %	Fe_2O_3 %	K_2O %	MgO %	MnO %	Na_2O %	P_2O_5 %	SiO_2 %	TiO_2 %
OF-7	Silicic	4.74	0.07	1.00	1.50	0.25	<0.01	0.03	0.01	92.09	0.12
OF-11	Silicic	7.13	0.05	1.76	4.64	0.18	0.01	0.17	0.07	86.07	0.14
OF-22	Unaltered	15.42	3.75	5.44	3.88	2.17	0.07	2.90	0.18	65.73	0.60
OF-31	Sericitic-argillic	14.66	0.08	1.23	3.85	0.37	0.01	0.07	0.04	79.80	0.34
OF-35	Argillic, aplite	14.35	0.43	9.45	0.89	3.36	0.03	1.02	0.03	70.80	0.14
OF-38	Unaltered	15.73	3.67	5.00	4.00	1.80	0.09	3.29	0.2	65.69	0.48
OF-40	Silicic	9.70	0.18	1.27	3.06	0.34	0.01	0.07	0.07	85.25	0.18
OF-42	Silicic	8.85	0.03	2.32	2.62	0.48	0.01	0.03	0.02	85.63	0.35
OF-60	Unaltered	15.28	4.02	5.16	4.16	1.97	0.08	3.04	0.18	65.92	0.54
OF-65	Sericitic-argillic	16.81	0.03	3.08	4.35	0.46	0.01	0.06	0.01	74.24	0.68
OF-76	Silicic, aplite	5.13	0.30	1.67	1.54	0.28	0.01	0.05	0.05	90.75	0.15
OF-79	Unaltered, aplite	11.48	0.61	2.24	6.10	0.30	0.02	1.85	0.03	77.48	0.16
OF-83	Sericitic-argillic, aplite	12.60	0.03	0.59	4.80	0.07	0.01	0.27	0.02	81.16	0.12

Note. Analysis conducted by ALS Minerals Inc.; analytical code ME-XRF 26 was selected for whole-rock analysis. Sample numbers OF-35, OF-76, OF-79, and OF-83 are aplite samples; the rest are granite analysis. Analytical data normalized to 100% anhydrous but do not total 100% due to rounding.

Alteration types and corresponding values for the AI and CCPI are in table 3 and plotted on an alteration box diagram (fig. 5). By plotting the CCPI against the AI, unaltered and altered granite and aplite cluster in separate fields. Unaltered granite plots near the center of the diagram and sericitic-argillic and silicic alteration plot on the right side of the diagram near the sericite edge and K-feldspar corner. The AI for sericite-argillic and silicic alteration range from a low of 83.9 up to 98.2 (table 3), which indicates near complete replacement of the feldspars by quartz, sericite, or illite. No carbonate minerals or chlorite were detected in the sericitic-argillic

Table 3. Alteration index (AI) and chlorite-carbonate-pyrite index (CCPI) values and corresponding alteration, rock types, and sample numbers.

Sample Number	Rock Type	Alteration Type	AI	CCPI
OF-7	Granite	Silicic	94.6	45.0
OF-11	Granite	Silicic	95.6	28.7
OF-22	Granite	Unaltered	47.6	52.9
OF-31	Granite	Sericitic-argillic	96.6	29.0
OF-35	Aplite	Argillic	74.6	87.0
OF-38	Granite	Unaltered	45.5	48.3
OF-40	Granite	Silicic	93.1	34.0
OF-42	Granite	Silicic	98.1	51.4
OF-60	Granite	Unaltered	46.5	49.8
OF-65	Granite	Sericitic-argillic	98.2	44.5
OF-76	Aplite	Silicic	83.9	55.0
OF-79	Aplite	Unaltered	72.0	24.2
OF-83	Aplite	Sericitic-argillic	94.2	11.5
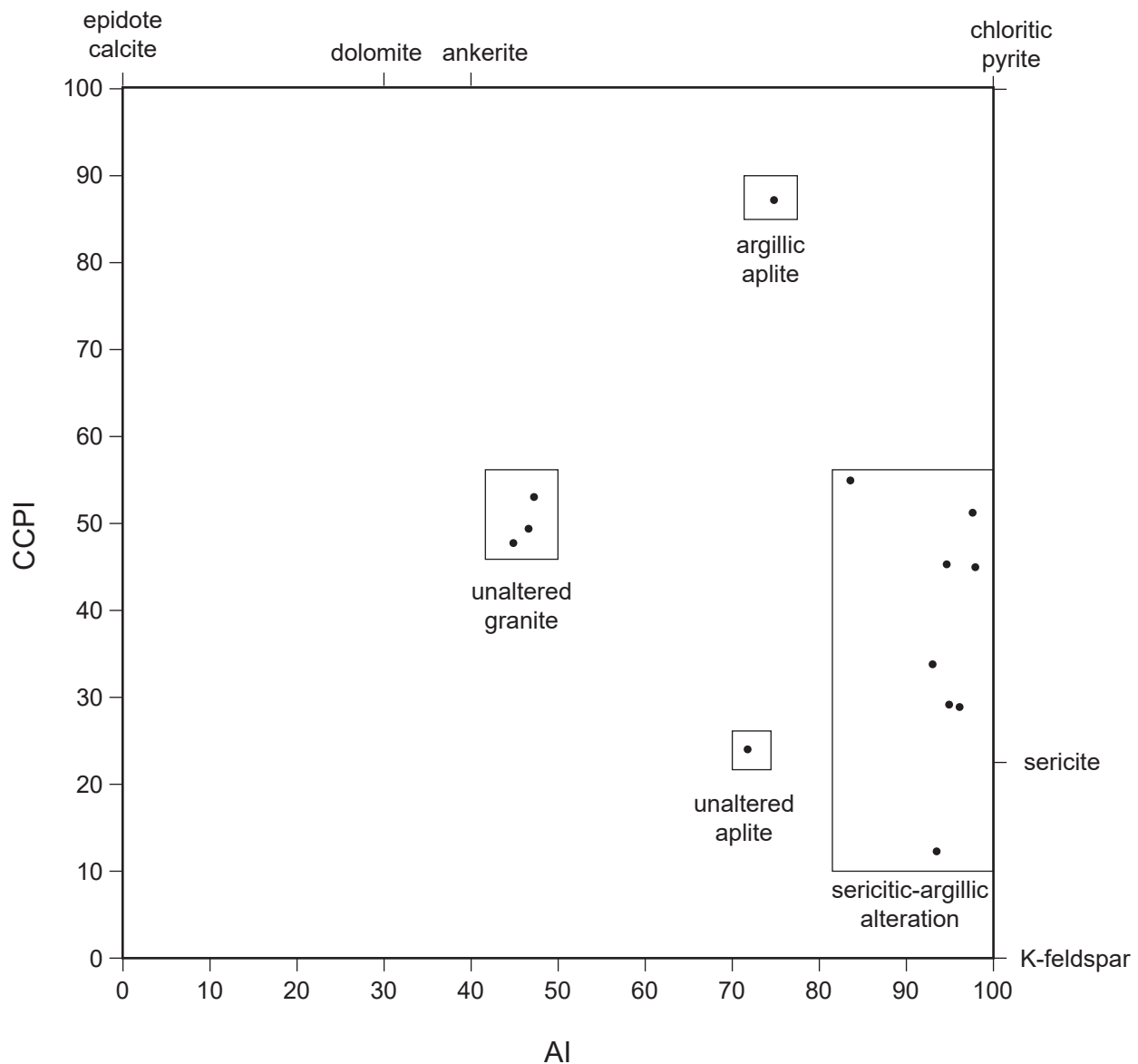
Figure 5. Alteration box diagram from Large and others (2001) showing fields of unaltered host rock, argillic, and sericitic-argillic alteration types. AI, Ishikawa alteration index; CCPI, chlorite-carbonate-pyrite alteration index.

and silicic altered granite and aplite, but disseminated pyrite and magnetite were observed, which is reflected by the CCPI varying from 11.5 for pyrite–magnetite depletion to 55 for pyrite–magnetite enrichment (table 3). Large and others (2001) noted that unaltered rocks plot in the center of the box diagram at the location of unaltered granite (fig. 5). Unaltered aplite is enriched in potassium and has a low iron content (table 2, OF-79), resulting in a CCPI of 24.2 and AI of 72, which plots near the K feldspar corner of the diagram.

One aplite sample shows argillic alteration with little sericite present; it is enriched in iron and depleted in potassium (table 2, OF-35) when compared to unaltered aplite. The AI for the argillic altered aplite is 74.6 and the CCPI is 87 approaching the chlorite–pyrite corner of the diagram.

Whole-rock oxides that show variations due to alteration (CaO, Fe_2O_3, MgO, NaO_2, and SiO_2) are plotted on isocon plots (fig. 6). The isocon was de-
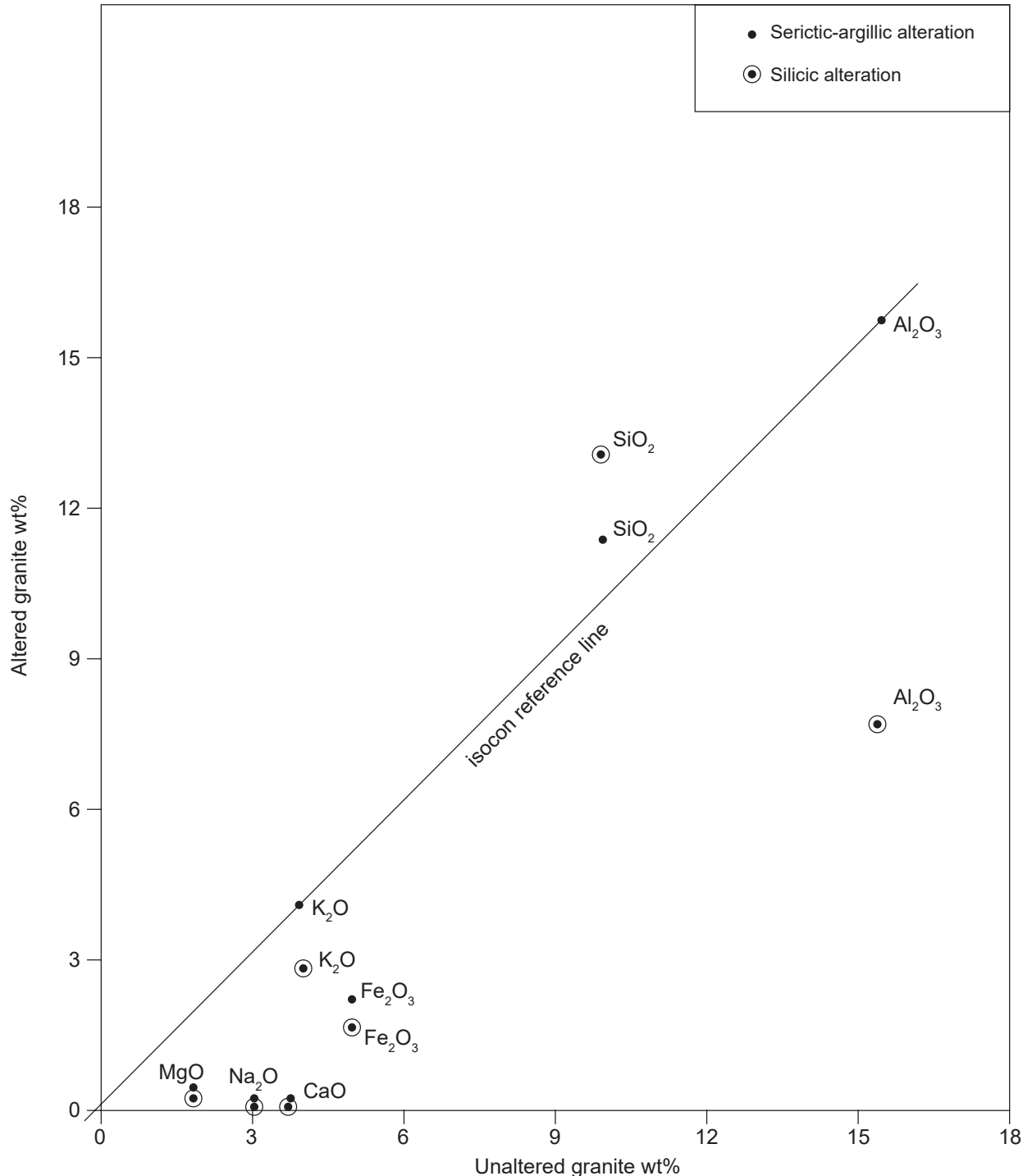
Figure 6. Isocon diagram for sericite-argillic and silicic alteration based on data from tables 4 and 5. Isocon reference line based on Al_2O_3 and K_2O analysis for unaltered granite and sericitic-argillic alteration.

Table 4. Isocon analysis of whole-rock averages in weight percent for granite alteration.

Oxides	C_{UA}	C_A ser-arg	C_A/C_{UA}	$\Delta C/C_{UA}$	ΔC
Al_2O_3	15.47	15.73	1.017	0.02	0.26
SiO_2	65.78	77.02	1.170	0.17	11.24
K_2O	4.01	4.10	1.022	0.02	0.09
CaO	3.81	0.06	0.015	-0.98	-3.75
Fe_2O_3	5.20	2.16	0.415	-0.59	-3.04
MgO	1.98	0.42	0.212	-0.78	-1.56
Na_2O	3.08	0.07	0.023	-0.98	-3.01

Oxides	C_{UA}	C_A silicic	C_A/C_{UA}	$\Delta C/C_{UA}$	ΔC
Al_2O_3	15.47	7.61	0.492	-0.51	-7.86
SiO_2	65.78	87.26	1.327	0.33	21.48
K_2O	4.01	2.96	0.738	-0.26	-1.05
CaO	3.81	0.08	0.021	-0.98	-3.73
Fe_2O_3	5.20	1.59	0.306	-0.69	-3.61
MgO	1.98	0.31	0.157	-0.84	-1.67
Na_2O	3.08	0.08	0.026	-0.97	-3.00

Note. C_{UA}, component averages for unaltered granite; C_A ser-arg, component averages for sericitic-argillic alteration; C_A silicic, component averages for silicic alteration; C_A/C_{UA}, slope of data points defining isocon; $\Delta C/C_{UA}$, gain or loss of oxides compared to unaltered granite; negative numbers indicate a loss, positive numbers indicate a gain; ΔC, gain or loss of oxides in wt%.

Table 5. Scaled whole-rock averages in wt% for granite alteration.

Oxide	C_{UA}	C_A ser-arg	Scale	C_{UA} scaled	C_A ser-arg scaled
SiO_2	65.78	77.02	0.15	9.9	11.6

Oxide	C_{UA}	C_A silicic	Scale	C_{UA} scaled	C_A silicic scaled
SiO_2	65.78	87.26	0.15	9.9	13.1

Note. C_{UA}, component averages for unaltered granite; C_A ser-arg, component averages for sericitic-argillic alteration; C_A silicic, component averages for silicic alteration; scale, factor used to scale down whole rock data to fit isocon plot; C_{UA} scaled, scaled components for unaltered granite; C_A ser-arg scaled, scaled components for sericitic-argillic alteration; C_A scilicic scaled, scaled components for silicic alteration.

fined using Al_2O_3 and K_2O, which shows little gain or loss between unaltered granite and sericitic-argillic alteration and are nearly immobile (tables 4, 5), indicated by C_A/C_{UA} (slope of the isocon) being close to 1 and $\Delta C/C_{UA}$ (gain or loss of oxide) having equal values and approaching 0. Kuwatani and others (2020) determined ΔC equal to zero and an isocon slope equal to one defines an immobile element and is used as a reference isocon. Silicic alteration shows a wide variation for Al_2O_3 and K_2O between unaltered and silicified granite and could not be used to define the isocon. Isocon analysis methods using mass balance equations from Grant (2005) and Kuwatani and others (2020) were used to determine the isocon reference line in figure 6.

In table 4, the $\Delta C/C_{UA}$ values for sericitic-argillic alteration oxides with the exception of Al_2O_3, K_2O, and SiO_2 are negative numbers, indicating a loss. Figure 6 show negative oxide averages (CaO, Fe_2O_3, MgO, and Na_2O) for sericitic-argillic alteration plotting below the Al_2O_3, K_2O isocon reference line, indicating a depletion in these oxides compared to unaltered granite. In contrast to sericitic-argillic alteration, silicic alteration shows a loss for all the oxides with the exception of silica oxide. Oxide losses for silicic alteration is greater than sericitic-argillic alteration, demonstrated by higher negative numbers for $\Delta C/C_{UA}$, and they plot the furthest below the isocon reference line (fig. 6).

The isocon plot in figure 6 shows SiO_2 plotting well above the isocon, indicating a gain of silica during alteration of the original granite. The plot also indicates a loss of Al_2O_3 and K_2O for the silicified granite (fig. 6). Silicic alteration and sericitic-argillic alteration have positive $\Delta C/C_{UA}$ values for SiO_2 (table 4), indicating a gain in silica for both alteration types. Silicic alteration has higher loss values (table 4) than sericitic-argillic alteration, indicating a stronger replacement of the original granite by silica. Some silicification took place during sericitic-argillic alteration, indicated by SiO_2 plotting above the isocon (fig. 6), but did not

Table 6. Trace element averages for three samples of unaltered granite (column 2) with corresponding sericitic-argillic (two samples), and silicic (six samples, except two for Au).

Element	Granite	Sericitic-Argillic	Silicic	Aplite	Silicic	Sericitic-Argillic	Argillic
Ag	0.59	2.21	11.4	0.16	4.19	0.46	1.77
Au	NA	NA	0.016	NA	NA	NA	NA
Al%	7.6%	7.7%	3.4%	5.71%	2.74%	5.95%	6.37%
As	3.1	79.8	53.1	3.8	512	13.9	41.9
Ba	830	155	201.7	380	200	80	100
Bi	0.06	0.24	1.0	0.08	0.05	0.29	0.92
Co	10.8	4.9	1.9	3.8	20.4	0.4	25.9
Cs	6.2	27.2	16.9	8.45	24.4	8.65	4.13
Cu	26	6.9	16.7	48.1	6.4	12.2	5.4
K%	3.3%	3.3%	1.9%	5.03%	1.3%	3.88%	0.70%
Li	33.2	26.7	83.3	12.6	171.0	60.2	32.5
Mn	583.3	65	89.8	141	58	86	195
Mo	2.8	2.4	8.0	1.99	16.8	2.17	5.69
Ni	8.1	6.8	2.7	4.7	1.7	1.2	9.0
Pb	15.5	13.4	14.8	21.2	6.1	43.9	55.3
Sb	0.57	10.2	24.3	0.48	28.0	6.46	11.45
Tl	0.73	3.87	1.2	1.02	1.84	1.40	0.43
W	1.3	6.7	8.7	2.7	6.1	4.6	3.1
Zn	9.5	10.0	18.8	18.0	19.0	57	70

Note. Aplite unaltered and corresponding silicic, sericitic-argillic, and argillic alteration is based on one sample for aplite and each alteration type. Values for Al and K are in weight percent (%) the rest are in parts per million. The major elements Al and K were used to define the isocon reference line. NA, not analyzed.

cause extensive mobilization of Al_2O_3 and K_2O. Aluminum oxide and K_2O remained nearly immobile during alteration of the original granite to sericitic-argillic alteration, indicated by the slope of the isocon C_A/C_{UA} being close to 1 and the $\Delta C/C_{UA}$ being 0.02. In contrast to sericitic-argillic alteration, during strong silicification of the original granite, Al_2O_3 and K_2O was lost, shown by Al_2O_3 and K_2O for silicic alteration plotting below the isocon (fig. 6).

Alteration Trace Elements

Trace element associations for epithermal vein systems and modern hot springs are geochemically unique (Mosier and others, 1987; Silberman and Berger, 1985; Simmons and Browne, 2000). Forty-eight trace elements were determined by ICP-MS methods for 15 samples representing two alteration types and unaltered host rocks (table 6; complete dataset is shown in appendix A). Trace elements that are known to be characteristic of epithermal vein systems, modern hot springs, and other elements consistently above instrument detection limits were selected from the total dataset and are shown in table 6. Analysis of unaltered host rocks were compared to altered rocks to determine the gain or loss of trace elements.

The degree of gain or loss of trace elements for silicic and sericitic-argillic alteration compared to unaltered granite are shown on an isocon plot (fig. 7, table 7). The isocon reference line was defined using Al and K, which showed little to no loss or gain between unaltered granite and sericitic-argillic alteration. Aluminum was nearly immobile, indicated by C_A/C_{UA} (slope of the isocon) being close to 1 and the $\Delta C/C_{UA}$ (gain or loss) approaching 0 (table 7), and K is determined to be immobile, indicated by the C_A/C_{UA} being 1 and the $\Delta C/C_{UA}$ equal to 0. The slope of the isocon reference line in figure 7 is similar to the reference isocon line in figure 6, indicating little to no difference between the two datasets. Silicic alteration shows a wide variation for Al and K (table 7) between unaltered granite and silicic alteration and could not be used to define an isocon. Isocon analysis methods from Grant (2005) and Kuwatani and others (2020) were used to determine the isocon reference line in figure 7 and determine loss or gain of individual elements (table 7). Analytical values that were too large to reasonably fit on the isocon diagram were scaled down (table 8) and values too low to be reasonably plotted were scaled up.

Compared to unaltered granite, sericitic-argillic alteration shows a loss in Ba, Co, Cu, Li, Mn, Mo, Ni, and Pb, indicated by the negative ΔC values (table 7) and plotting below the reference isocon (fig. 7). Sericitic-argillic alteration demonstrates a gain in Ag,

Figure 7. Isocon diagram based on data from tables 7 and 8 for silicic and sericitic-argillic alteration. Isocon reference line based on Al and K analysis for unaltered granite and sericitic-argillic alteration.
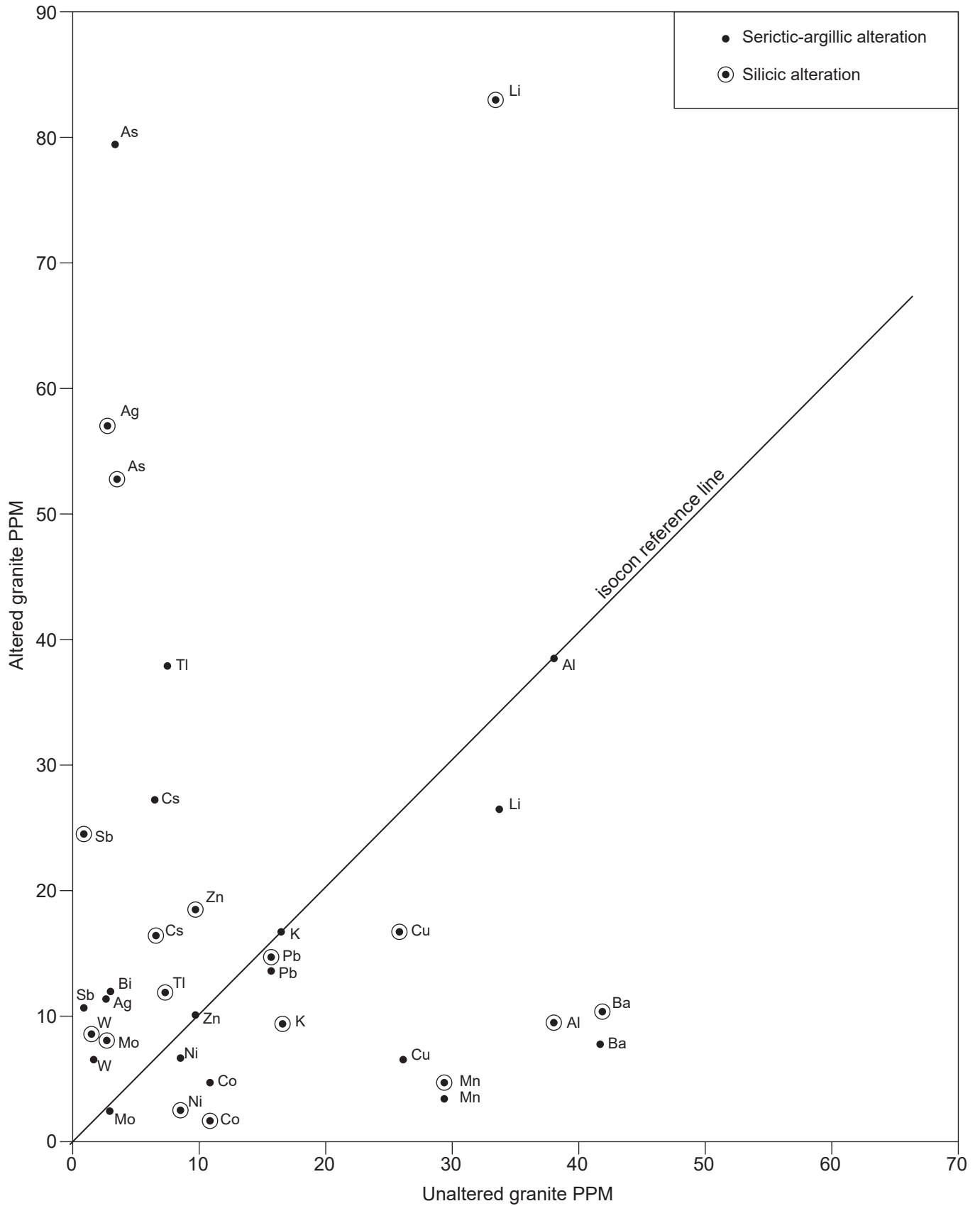
Table 7. Isocon analysis of ICP-MS averages in parts per million (ppm) for granite alteration.

Elements	C_{UA}	C_A ser-arg	C_A/C_{UA}	$\Delta C/C_{UA}$	ΔC
Ag	0.59	2.21	3.746	2.75	1.62
Al	76,000	77,000	1.013	0.01	1,000
As	3.1	79.8	25.742	24.74	76.7
Ba	830	155	0.187	-0.81	-675
Bi	0.06	0.24	4.00	3.0	0.18
Co	10.8	4.9	0.454	-0.55	-5.9
Cs	6.2	27.2	4.387	3.39	21.0
Cu	26	6.9	0.265	-0.74	-19.1
K	33,000	33,000	1.000	0.0	0.0
Li	33.2	26.7	0.804	-0.20	-6.5
Mn	583.3	65	0.111	-0.89	-518.3
Mo	2.8	2.4	0.857	-0.14	-0.4
Ni	8.1	6.8	0.840	-0.16	-1.3
Pb	15.5	13.4	0.865	-0.14	-2.1
Sb	0.57	10.2	17.895	16.90	9.63
Tl	0.73	3.87	5.301	4.30	3.14
W	1.3	6.7	5.154	4.15	5.4
Zn	9.5	10.0	1.053	0.05	0.5

Elements	C_{UA}	C_A silicic	C_A/C_{UA}	$\Delta C/C_{UA}$	ΔC
Ag	0.59	11.4	19.322	18.32	10.81
Al	76,000	34,000	0.447	-0.55	-42,000
As	3.1	53.1	17.129	16.13	50.0
Ba	830	201.7	0.243	-0.76	-628.3
Bi	0.06	1.0	16.667	15.67	0.94
Co	10.8	1.9	0.176	-0.82	-8.9
Cs	6.2	16.9	2.726	1.73	10.7
Cu	26	16.7	0.642	-0.36	-9.3
K	33,000	19,000	0.576	-0.42	-1.4
Li	33.2	83.3	2.509	1.51	50.1
Mn	583.3	89.8	0.154	-0.85	493.5
Mo	2.8	8.0	2.857	1.86	5.2
Ni	8.1	2.7	0.333	-0.67	-5.4
Pb	15.5	14.8	0.995	-0.05	-0.7
Sb	0.57	24.3	42.632	43.63	23.73
Tl	0.73	1.2	1.644	0.64	0.47
W	1.3	8.7	6.692	5.69	7.4
Zn	9.5	18.8	1.979	0.98	9.3

Note. C_{UA}, component averages for unaltered granite; C_A ser-arg, component averages for sericitic-argillic alteration; C_A silicic, component averages for silicic alteration; C_A/C_{UA}, slope of data points defining isocon; $\Delta C/C_{UA}$, gain or loss of elements compared to unaltered granite; negative numbers indicate a loss, positive numbers indicate a gain; ΔC, gain or loss of elements in ppm.

As, Bi, Cs, Sb, Tl, W, and Zn, indicated by these elements plotting above the reference isocon (fig. 7) and positive ΔC values in table 7. Silicic alteration compared to unaltered granite has a depletion in Ba, Co, Cu, Mn, Ni, and Pb, indicated by negative ΔC values and plotting below the reference isocon (fig. 7). Silicic alteration gained Ag, As, Bi, Cs, Li, Mo, Sb, Tl, W, and Zn compared to unaltered granite, indicated by positive ΔC values and plotting above the reference isocon line (fig. 7).

Aplite is not a common host mineral for the epithermal veins, and one sample of each alteration type was collected and analyzed. Sericitic-argillic altered aplite shows a gain in Ag, As, Bi, Li, Mo, Pb, Sb, Tl, W, and Zn compared to unaltered aplite (table 6). Silicic alteration is enriched in the same elements as sericitic-argillic alteration, with the addition of Co and Cs and a depletion of Pb. Argillic alteration is also enriched in the same elements as sericitic-argillic alteration with the loss of Tl. Silicic alteration of aplite caused a loss in Al, Ba, Ca, Cu, Fe, K, Mg, Mn, Na, and Ni. Sericitic-argillic and argillic alteration caused

Table 8. Scaled ICP-MS averages in ppm for granite alteration.

Elements	C_{UA}	C_A Ser-Arg	Scale	C_{UA} Scaled	C_A Ser-Arg Scaled
Ag	0.59	2.21	5	2.95	11.1
Al	76,000	77,000	0.0005	38.0	38.5
Ba	830	155	0.05	41.5	7.75
Bi	0.06	0.24	50	3.0	12.0
K	33,000	33,000	0.0005	16.5	16.5
Mn	583.3	65	0.05	29.2	3.25
Tl	0.73	3.87	10	7.3	38.7

Elements	C_{UA}	C_A Silicic	Scale	C_{UA} Scaled	C_A Silicic Scaled
Ag	0.59	11.4	5	2.95	57
Al	76,000	34,000	0.0005	38.0	17.0
Ba	830	201.7	0.05	41.5	10.1
Bi	0.06	1.0	50	3	50
K	33,000	19,000	0.0005	16.5	9.5
Mn	583.3	89.8	0.05	29.2	4.49
Tl	0.73	1.2	10	7.3	12.0

Note. C_{UA}, component averages for unaltered granite; C_A ser-arg, component averages for sericitic-argillic alteration; C_A silicic, component averages for silicic alteration; scale, factors used to scale up or down ICP-MS data to fit isocon plot; C_{UA} scaled, scaled components for unaltered granite; C_A ser-arg scaled, scaled components for sericitic-argillic alteration; C_A silicic scaled, scaled components for silicic alteration.

aplite to lose the same elements as silicic alteration, with the exception of Al, which has the same Al concentrations as unaltered aplite and a gain in Fe, Mg, and Ni for argillic alteration.

The trace elements Au, Ag, As, Sb, Tl, Pb, and Zn are characteristic of hydrothermal systems that are classified as epithermal (Silberman and Berger, 1985). Discharge waters from geothermal wells in New Zealand contain Au, Ag, As, Bi, Li, Mo, Pb, Sb, Tl, W, and Zn (Weissberg, 1969; Ewers and Keays, 1977; Simmons and Browne, 2000; Simmons and others, 2016). The suite of enriched trace elements found in the Oro Fino mining district altered rocks are the same as those found in active geothermal fields and are characteristic of epithermal systems. The enrichment of Cs in the Oro Fino veins is not known to be a characteristic trace element in epithermal systems.

VEIN MINERALS

Minerals were identified from 36 polished sections, 38 polished thin sections, and 23 thin sections. All three types of sections were examined using reflected light and transmitted light microscopy and scanning electron microscopic-energy dispersive spectroscopy (SEM-EDS) techniques. The SEM-EDS analysis was performed at the Center for Advanced Mineral and Metallurgical Processing, Montana Tech. Minerals were also identified by examination of hand specimens and cut slabs. Mineral grains and crystals were extracted from hand specimens and slabs for

analysis by SEM-EDS. A total of 37 minerals from nine groups were identified (table 9).

VEIN PARAGENESIS

The veins in the district are characterized by massive white quartz filling open fractures with included breccia fragments of altered granite host rock, disseminated sulfide minerals, and vugs lined with quartz crystals and, when present, scattered euhedral silver minerals in vugs. Vein widths varied from less than 0.3 m to over 1.8 m and were mined to depths up to 274 m at the Champion mine. The host granite was altered and replaced along the vein margins by quartz and disseminated pyrite. Where the veins are exposed in shaft collars and prospect pits, host rock alteration extends about 1 m from the vein contacts depending on degree of fracturing and brecciation.

Paragenesis refers to the sequence of mineralizing events that developed the Oro Fino veins. Characterization of the mineralizing events was determined from SEM-back scatter images, microscopic examination of polished sections, thin sections, polished thin sections, and examination of cut slabs and hand specimens. The mineralizing events can be broken into a series of stages represented by fissure veins, base metal mineralization, silver–gold mineralization, late stage mineralization, and supergene alteration.

Table 9. Summary of minerals identified from the Oro Fino veins.

Sulfides and Sulfosalts	Formula
Acanthite	Ag_2S
Arsenopyrite	$FeAsS$
Chalcopyrite	$CuFeS_2$
Covellite	CuS
Enargite	Cu_3AsS_4
Freibergite	$Ag_6Cu_4(Fe,Zn)_2Sb_4S_{13}$
Galena	PbS
Krupkaite	$PbCuBi_3S_6$
Marcasite	FeS_2
Miargyrite	$AgSbS_2$
Molybdenite	MoS_2
Polybasite	$(Ag,Cu)_{16}Sb_2S_{11}$
Pyrargyrite	Ag_3SbS_3
Pyrite	FeS_2
Sphalerite	ZnS
Tetrahedrite	$Cu_6Cu_4(Fe,Zn)_2(Sb,As)_4S_{13}$
Native Elements	
Gold variety electrum	XAu:Ag 0.3:0.7 to XAu:Ag 0.4-0.6
Silver	Ag
Sulfur	S
Oxides	
Hematite	$\alpha - Fe_2O_3$
Rutile	TiO_2
Scheelite	$CaWO_4$
Senarmontite	Sb_2O_3
Uraninite	UO_2
Phosphates	
Apatite-(caf)	$Ca_5(PO_4)F$
Monazite-(Ce)	$(Ce,La,Nd)PO_4$
Plumbogummite	$PbAl_3(PO_4)_2(OH,H_2O)_6$
Rhapdophane-(Ce)	$(Ce,La)PO_4 \cdot H_2O$
Arsenate	
Scorodite	$Fe^{3+}AsO_4 \cdot 2H_2O$
Sulfate	
Baryte	$BaSO_4$
Halide	
Fluorite	CaF_2
Carbonate	
Ankerite	$Ca(Fe^{2+},Mg,Mn)(CO_3)_2$
Calcite	$CaCO_3$
Silicates	
Chamosite	$(Fe,Al,Mg)_6(Si,Al)_4O_{10}(OH)_6$
Quartz	SiO_2
Schorl	$Na(Fe^{2+})_3Al_6(BO_3)_3[Si_6O_{18}](OH)_4$
Zircon	$ZrSiO_4$

Fissure Veins

The earliest veins are fissure veins filling fractures in the altered host granite. The fissure veins are characterized by quartz and pyrite with minor disseminated Ca, W, Ti, and rare earth oxide and phosphate minerals. As the wall rock altered by silicification and sericitic-argillic alteration, the quartz fissure veins were crystallizing in host rock fractures from invading hydrothermal fluids. When the quartz was crystallizing, disseminated scheelite, rutile, monazite-(Ce), and rhapdophane-(Ce) crystallized with the quartz. The granite accessory mineral zircon trapped in quartz veins as disseminated grains was possibly from the host wall rocks. Amphibole minerals in the host granite altered into chamosite.

Schorl is concentrated near the margins of veins filling open spaces in brecciated and altered aplite and granite, and brecciated quartz. SEM-EDS analyses show an intermediate composition between dravite and schorl, containing equal amounts of Fe and Mg. Schorl needles are included in vein quartz, pyrite, and chalcopyrite, suggesting an earlier crystallization than quartz, pyrite, and chalcopyrite. Molybdenite occurs as anhedral grains disseminated in quartz impregnated with schorl needles and masses.

Base Metal Mineralization

Base metal mineralization (figs. 8, 9) started with the alteration of the host granite near wall rock contacts and assimilated breccia fragments with the precipitation of pyrite, arsenopyrite, and chalcopyrite along with quartz and minor molybdenite. These early sulfide minerals form disseminations in quartz, fill open spaces, and wall rock fissures. Later sulfide and sulfosalt minerals encrust the early precipitated minerals in open space fillings. As quartz crystallization continued, other sulfide and sulfosalt minerals precipitated as disseminations in quartz, filling open spaces in crystallized quartz, and scattered in vugs as euhedral crystals attached to quartz crystals.

Two sphalerite generations were identified occurring as coarse anhedral grains crystallized on pyrite and chalcopyrite in open spaces, and a second generation replaces early precipitated pyrite. The first sphalerite generation (fig. 8B) to crystallize has a high iron content (1.95–3.39 atomic weight percent Fe) and a second generation replacing pyrite (fig. 8C) has a lower iron content (0.23 atomic weight percent Fe). The first sphalerite generation has inclusions of rounded chalcopyrite grains following cleavage planes. The second sphalerite generation is lacking chalcopyrite inclusions following cleavage planes and shows replacement textures along pyrite contacts.

Sphalerite occurs as individual grains on the margins of chalcopyrite grains in sulfide filled vugs (fig. 9A). Enargite and tetrahedrite occur on the margins of chalcopyrite grains (fig. 9A) and appear to have crystallized at the same time. Tetrahedrite appears to replace shalerite by displaying dissolution textures on
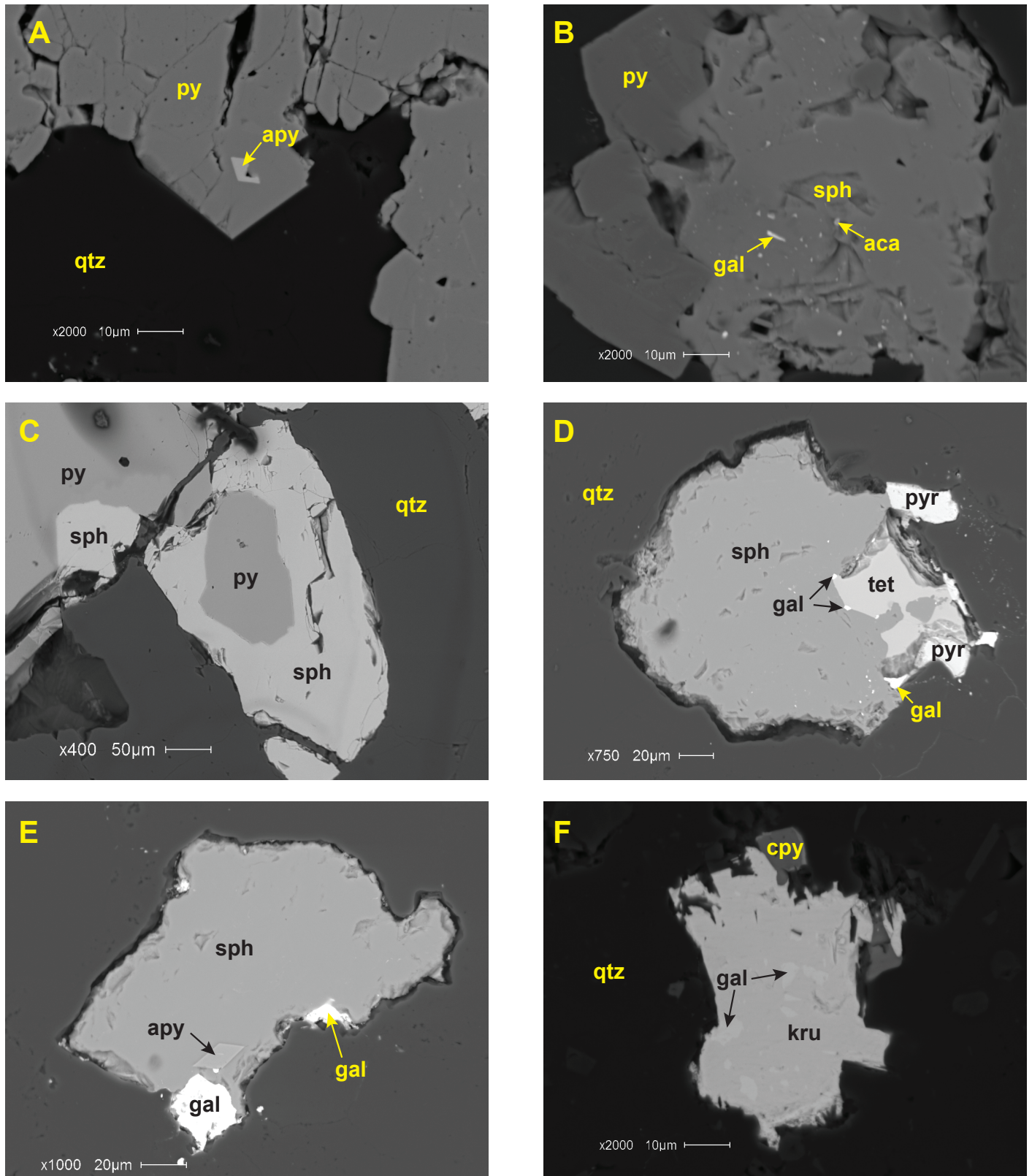
Figure 8. SEM-BSE images of minerals crystallized during base metal mineralization. (A) Euhedral apy grain included in py crystals. (B) Sph grain filling open space between py grains, minor gal, and aca filling open spaces in sph. (C) Second sph generation replacing py. (D) Tet replacing sph with minor gal and pyr association. (E) Euhedral apy grain in sph with gal on sph margin. (F) Kru included with partially replaced rounded gal grains with cpy on grain margin. Abbreviations: apy, arsenopyrite; aca, acanthite; cpy, chalcopyrite; gal, galena; kru, krupkaite; py, pyrite; pyr, pyrargyrite; qtz, quartz; sph, sphalerite; tet, tetrhedrite.
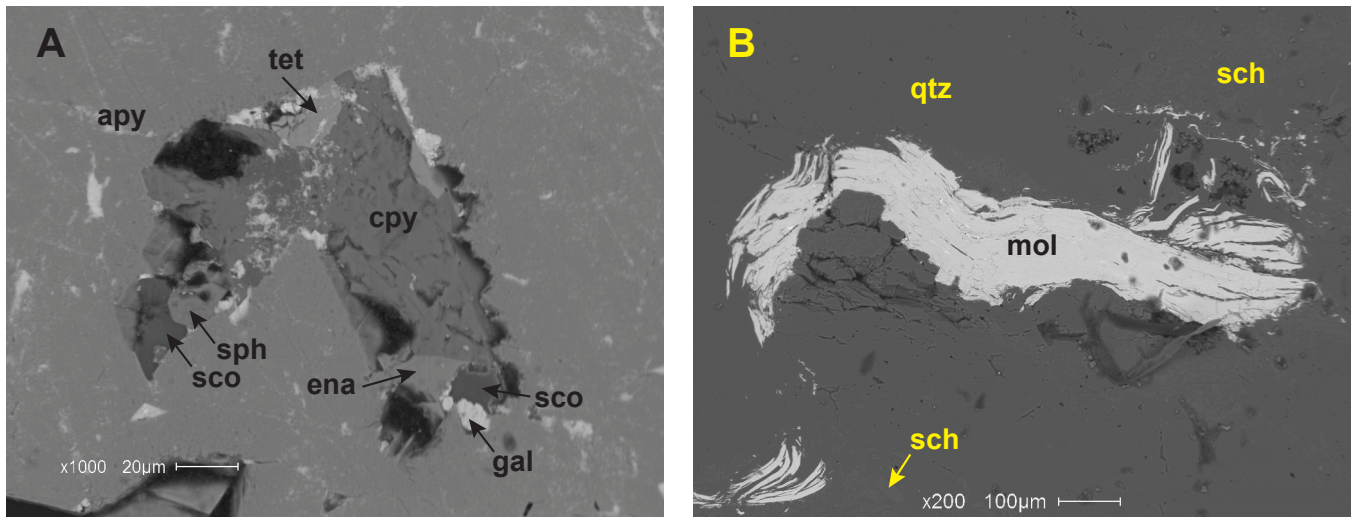
Figure 9. SEM-BSE images of minerals crystallized during base metal mineralization. (A) Cpy filling open space in apy. Tet, ena, gal, and sph formed on cpy grain margin. Minor sco replaces apy and fills open space in apy. (B) Mol grain filling open space in quartz associated with sch. Abbreviations: apy, arsenopyrite; cpy, chalcopyrite; ena, enargite; gal, galena; mol, molybdenite; qtz, quartz; sch, schorl; sco, scorodite; sph, sphalerite; tet, tetrahedrite.

grain boundaries between the two minerals (fig. 8D). Galena crystallized after the copper minerals, occurs as anhedral grains along grain boundaries (fig. 8E,F), and fills fractures in the early crystallized sulfide minerals. Krupkaite appears to replace galena by displaying a dissolution texture with rounded galena grains included in krupkaite (fig. 8F).

Silver–Gold Mineralization

The silver minerals fill fractures and open spaces in base metal sulfides and vein quartz, and occur as euhedral crystals in quartz vugs. Silver minerals occur as anhedral grains partially enclosing and on the margins of pyrite, sphalerite, and galena (fig. 10). Acanthite fills open spaces as anhedral grains with pyrite in previously crystallized quartz (fig. 10A). In hand specimens, acanthite was observed in quartz vugs as needle shaped crystals forming scattered clusters attached to quartz and pyrargyrite crystals. Pyrargyrite and acanthite occur together as intergrown anhedral grains filling open spaces in quartz and partially to completely enclose galena and sphalerite and fill fractures in sphalerite. Pyrargyrite occurs in quartz vugs as euhedral crystals attached to quartz crystals and acanthite grains (figs. 10B,C,D). Miargyrite is a rare mineral in the veins and was only found in one polished section where it occurs as inclusions in pyrite (fig. 10E). Native silver and electrum (a solid solution of silver and gold) occurs as individual particles included in and on the surface of acanthite and pyrargyrite (figs. 10A,B,C). Freibergite occurs as anhedral grains on the margins of pyrargyrite and displays a

dissolution texture along the contact with pyrargyrite. Polybasite was identified from hand specimens where it forms euhedral crystals attached to quartz crystals. Pyargyrite crystals adjacent to polybasite crystals display dissolution and polybasite crystals are attached to partially dissolved pyrargyrite.

Late Stage Mineralization

Baryte, calcite, ankerite, and fluorite fill fractures in brecciated quartz veins. At the Mystery mine (fig. 2), fluorite veins up to 0.30 m wide fill fractures and open spaces in brecciated vein quartz. Euhedral fluorite grains are enclosed in quartz and late stage quartz fills fractures in fluorite. Fluorite thus crystallized with vein quartz during the last stage of vein development.

At another location (fig. 2, location 66), coarsely crystallized baryte forming euhedral crystals fills fractures and open spaces in brecciated quartz. Baryte identified by SEM-EDS analysis was found in a polished section as inclusions in magnetite. Baryte occurring as fracture fillings suggests late crystallization during vein development. Ankerite was found in a vein south of the Champion mine (fig. 2, locations 86–87), where it fills fractures in quartz and altered aplite host rock. Fine-grained quartz occurs on the margins of ankerite filled fractures and can be included in the ankerite veins. Ankerite crystallized with late stage vein quartz near the end of vein development. Bladed calcite was found on the dump of a prospect adit (fig. 2, locations 58–60), where it occurs as compacted masses.
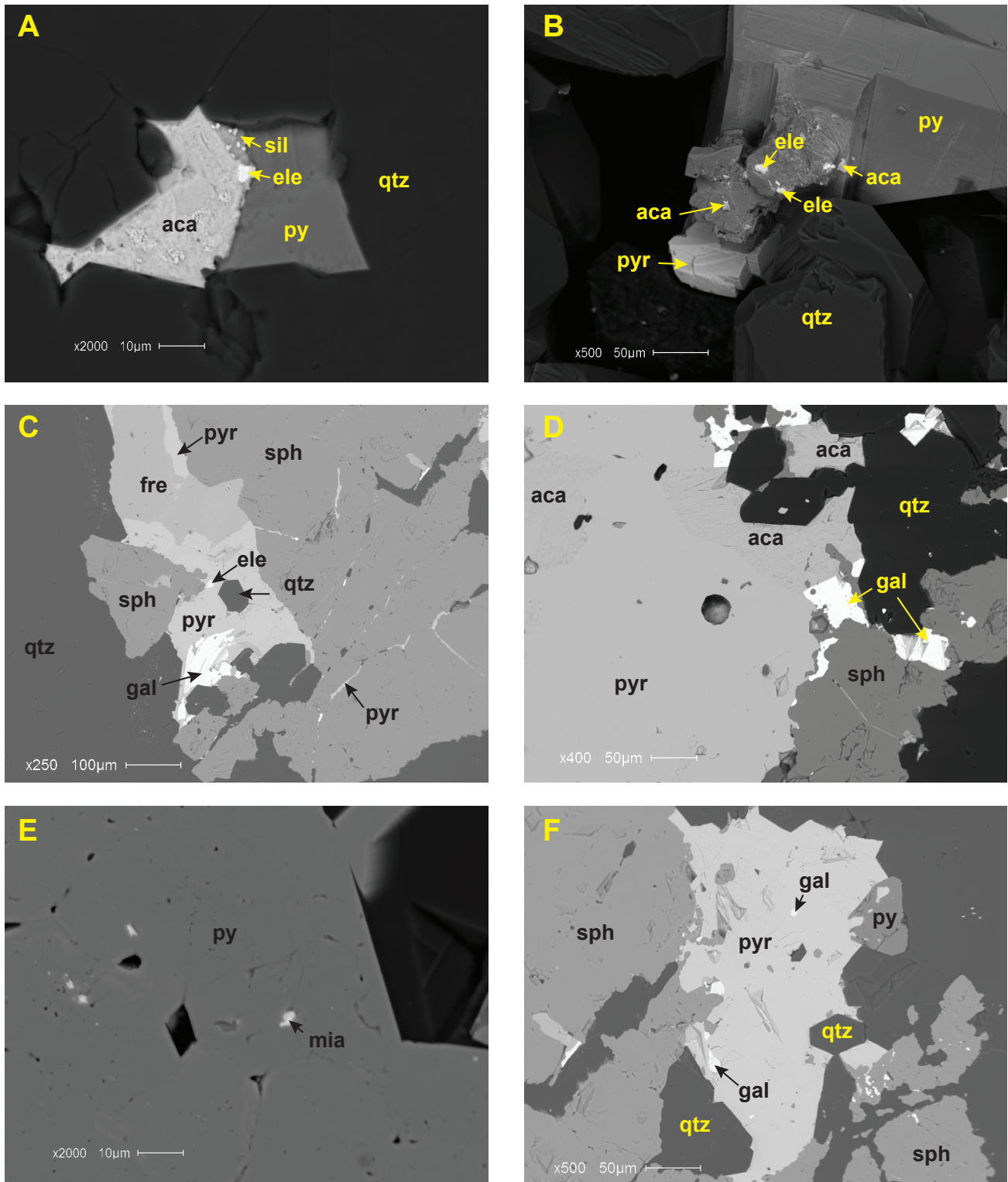
Figure 10. SEM-BSE images of minerals crystallized during silver-gold mineralization. (A) Aca filling open space in qtz with py. Aca crystallized with sil and ele grains. (B) Vug with euhedral pyr and qtz with scattered grains of aca and ele on py. (C) Fre replacing pyr overprinting sph and gal. Ele inclusion in pyr. Fractures in sph filled with pyr. (D) Co-genetic crystallization of aca and pyr overprinting sph, gal, and qtz. (E) Anhedral mia grains included in py. (F) Pyr overprinting sph, py, and gal. Abbreviations: aca, acanthite; ele, electrum; fre, freibergite; gal, galena; mia, miargyrite; py, pyrite; pyr, pyrargyrite; qtz, quartz; sil, silver; and sph, sphalerite.

Supergene Alteration

Supergene alteration produced oxide, arsenide, phosphate, and secondary sulfide minerals (fig. 11). Covellite identified from polished sections replaces chalcopyrite along fractures and grain boundaries. Scorodite deposited in fractured quartz (fig. 11A) directly replaces arsenopyrite along grain boundaries between quartz. Scorodite was also observed replacing enargite along grain boundaries. Sphalerite was replaced by sulfur along fractures and grain boundaries and displays replacement textures (fig. 11B). Pyrargyrite was replaced by minor senarmonite on a grain boundary between chalcopyrite and pyrargyrite (fig. 11C). Included in the senarmonite are rounded grains of silver that developed when the pyrargyrite was replaced. Pyrite was partially to completely replaced by hematite (fig. 11D) and is included with rounded fluorapatite grains and schorl needles. Plumbogummite is a rare mineral in the veins and was observed from one sample. Plumbogummite was not observed replacing any of the primary vein minerals and occurs as minor fracture fillings and coatings on rutile (fig. 11E).

Mineralizing Sequence

The paragenesis or mineralizing sequence shown in figure 12 reflects physical and geochemical changes that took place during vein development. Mineralization of the veins started with quartz filling fissures in the brecciated and fractured host granite. Along the fracture contacts, silicification altered the wall rock and breccia fragments, and under favorable conditions schorl crystallized along the vein margins.

Base metal mineralization overlaps fissure vein development and host rock alteration. Quartz was precipitated continuously throughout the mineralizing stages and is represented by a variety of generations from chalcedony to coarsely developed crystals filling open spaces and fractures. Pyrite, arsenopyrite, and chalcopyrite were the first sulfide minerals to crystallize along with minor molybdenite. With the introduction of Cu, Sb, and Zn, the hydrothermal fluids began reacting with pyrite and arsenopyrite. When the reaction between the hydrothermal fluids and earlier sulfide phases began, sphalerite precipitated and partially replaced pyrite and arsenopyrite. Early crystallized sphalerite was invaded by Cu-enriched fluids, causing chalcopyrite to replace sphalerite along cleavage planes. Following chalcopyrite precipitation, more complex copper minerals crystallized, represented by enargite and tetrahedrite.

After the copper minerals developed, lead and bismuth became active in the hydrothermal fluids, allowing galena and krupkaite to precipitate. Galena crystallized at the close of the copper mineralization event. Remaining copper and bismuth in the hydrothermal fluids reacted with galena and replaced it with krupkaite. Krupkaite replacing galena suggests that it was the last mineral to form during base metal mineralization.

Silver minerals were overprinted on base metal minerals as encrustations and fracture fillings, indicating a later crystallization sequence than base metal mineralization. During this stage, quartz was deposited as chalcedony, crystalline crusts, or euhedral crystals filling fractures in earlier deposited vein quartz and lining vugs. Acnathite and pyrargyrite crystallized together and were the first silver minerals to precipitate. They fill fractures and enclose earlier sulfide phases, occur as crystals in open vugs, and fill open spaces in vein quartz. Both minerals form intergrown grains, suggesting a co-genetic relationship. During silver–gold mineralization the hydrothermal fluids became enriched with silver and antimony. Native silver and electrum (a solid solution of silver and gold) was deposited as individual particles on pyrargyrite and acnathite.

The last silver minerals to be deposited were freibergite and polybasite. Pyrargyrite shows dissolution textures along grain boundaries, with freibergite replacing pyrargyrite. Polybasite was observed only in hand specimens as euhedral crystals in open vugs with acanthite and pyrargyrite. In the presence of polybasite, pyrargyrite displays dissolution textures and polybasite crystals are attached to the partially dissolved pyrargyrite. It appears the later silver minerals freibergite and polybasite crystallized from the reaction of hydrothermal fluids with pyrargyrite. Hydrothermal fluids containing As, Cu, Fe, and Zn reacted with pyrargyrite, causing freibergite and polybasite to replace pyrargyrite. The silver and antimony needed to generate freibergite and polybasite were probably sourced from the pyrargyrite during the replacement reaction.

Late stage mineralization characterized by baryte, calcite, ankerite, and fluorite filling fractures and open spaces in brecciated vein quartz. Euhedral to anhedral fluorite grains are enclosed in late stage vein quartz and fluorite fractures are filled with late stage vein quartz. Disseminated pyrite was the only sulfide mineral deposited during this mineralizing stage. This stage records the final stage of vein development and was most likely deposited from metal poor, low-temperature, hydrothermal fluids.
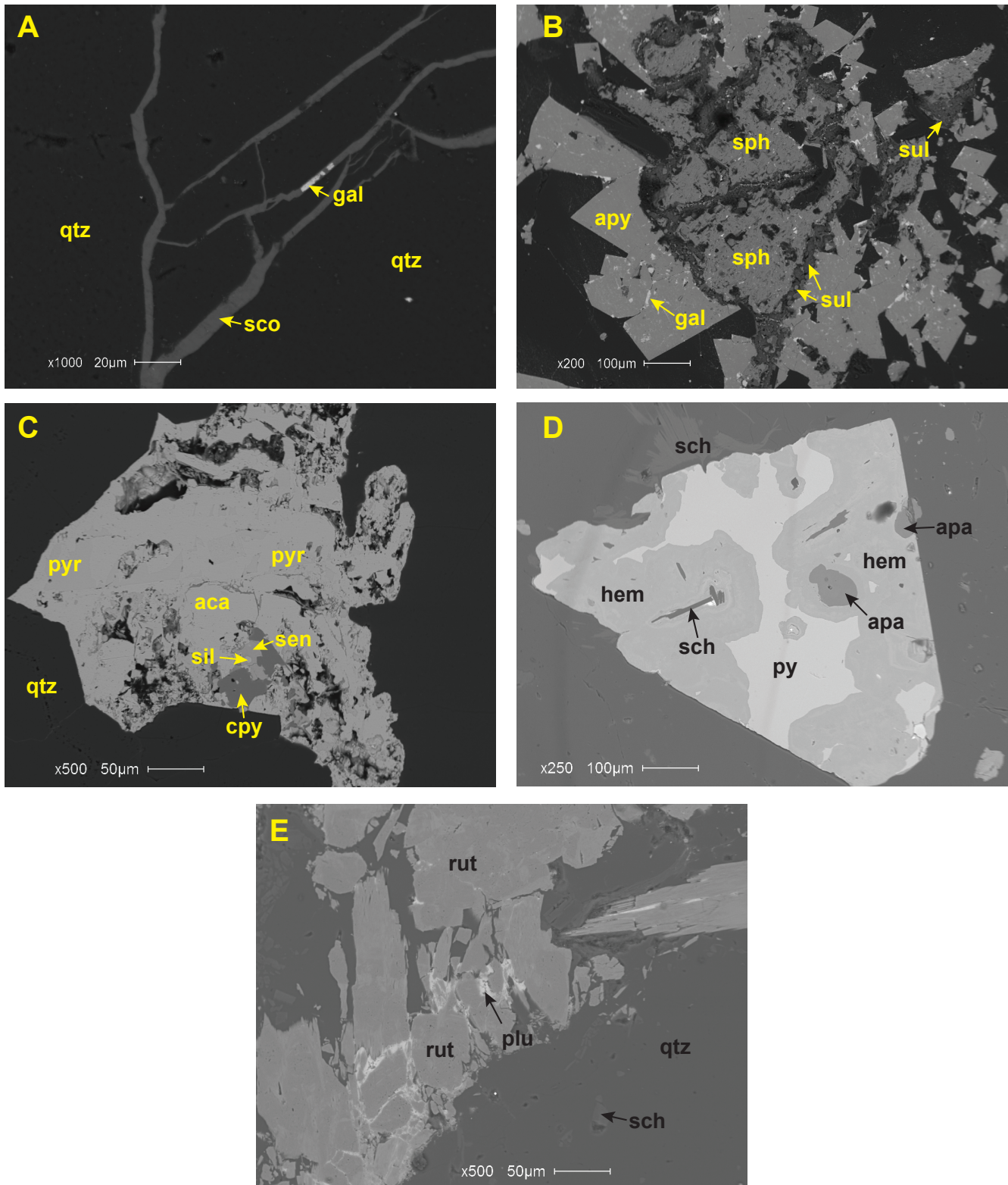
Figure 11. SEM-BSE images of minerals crystallized during supergene alteration. (A) Sco filling fractures in qtz. (B) Apy replaced by sph with sul replacing sph along grain boundaries and fractures. (C) Sen replacing pyr with sil inclusions. (D) Hem replacing py with preserved sch and apa inclusions from replaced py. (E) Plu filling factures in rut. Abbreviations: aca, acanthite; apa, apatite-(CaF); apy, arsenopyrite; cpy, chalcopyrite; gal, galena; hem, hematite; plu, plumbogummite; py, pyrite; pyr, pyrargyrite; qtz, quartz; rut, rutile; sch, schorl; sco, scorodite; sen, senarmontite; sil, silver; sph, sphalerite; and sul, sulfur.

	BASE METAL MINERALIZATION	SILVER-GOLD MINERALIZATION	LATE STAGE MINERALIZATION	SUPERGENE MINERALIZATION
QUARTZ	████████████████████████████████			
PYRITE	████████████████████████████████			
ARSENOPYRITE	██			
MOLYBDENITE	█			
CHALCOPYRITE	██			
SPHALERITE	███ ██			
ENARGITE	██			
TETRAHEDRITE		██	██	
GALENA		███		
KRUPKAITE		█		
MARCASITE			██	
COVELLITE				██
ACANTHITE		████		
PYRARGYRITE		███		
MIARGYRITE		███		
SILVER		███		██
GOLD		███		
FREIBERGITE			███	
POLYBASITE			███	
SULFUR				████
SCORODITE				████
MAGNETITE				███
SENARMONTITE				██
PLUMBOGUMITE				███
FLUORITE			████	
BARITE			████	
ANKERITE			██	

Figure 12. Paragenesis of base metal, silver–gold, late stage, and supergene mineralizing events for the Oro Fino veins.

Supergene alteration followed the hydrother-mal event and probably developed from meteoric flu-ids or groundwater reacting with the sulfide minerals, causing replacement by secondary minerals. Meteoric fluids reacting with sphalerite caused native sulfur to replace sphalerite on grain margins. The alteration of arsenopyrite caused arsenic and iron to go into solution, resulting in the development of scorodite in quartz fractures. Enargite and arsenopyrite were also replaced by scorodite on grain boundaries. Pyargyrite reacting with meteoric waters caused a minor replace-ment by senarmonite with native silver. Pyrite was partially to completely replaced by hematite. Plum-bogummite does not show a replacement texture with primary minerals and fills fractures in rutile.

VEIN TRACE ELEMENTS

Samples from veins across the district were analyzed by ALS Minerals, Inc. for 48 trace elements by four acid digestion ICP-MS methods. Gold was analyzed by fire assay with either an ICP-AES or gravimetric finish, and ore-grade elements were sub-sequently analyzed by four acid digestion and ICP-AES methods. Results are reported in appendix B for 18 elements that show anomalous concentrations compared to unaltered and altered granite. Average analytical results for 29 vein samples collected from mine dumps are shown in table 10.

Samples represent mined quartz veins with dis-seminated sulfide minerals. Quartz veins showed multiple stages of brecciated white to gray quartz and open space filling by multiple quartz crystal bands, with disseminated pyrite being the most common vis-

Table 10. Analytical averages for elements with anomalous results for quartz veins from mines and prospects throughout the Oro Fino mining district compared to unaltered granite.

Elements	Unaltered Granite Analytical Averages ppm	n	Quartz Veins Analytical Averages ppm	n
Au	NA		1.32	29
Ag	0.59	3	322.2	29
As	3.1	3	805.8	29
Ba	830	3	195.2	29
Bi	0.06	3	3.6	29
Co	10.8	3	7.5	29
Cs	6.2	3	16.7	29
Cu	26.0	3	169.5	29
Li	33.2	3	111.0	29
Mo	2.8	3	53.0	29
Pb	15.5	3	152.3	29
Rb	119.8	3	99.1	29
Sb	0.57	3	115.8	29
Sr	525.6	3	59.3	29
Te	<0.05	3	1.6	11
Tl	0.73	3	2.0	29
W	1.3	3	6.3	29
Zn	9.5	3	115.9	29

Note. ppm, parts per million; NA, not analyzed. Complete analytical results are in appendix B.

ible sulfide mineral. Sample size ranged from 0.5 to 1.5 kg, with most samples averaging about 1 kg.

Gains or losses of element concentrations for quartz veins as compared to host granite are shown on an isocon diagram (fig. 13) and table 11. Table 11 results show there are no conserved elements with equal concentrations between the unaltered granite and quartz veins, indicated by the isocon slopes C_{QV}/C_{UA} being well below or above 1, which means they cannot be used for an isocon reference line. The isocon reference line was taken from figure 7, which was used for the altered granite trace elements. Losses and gains of individual elements were determined using isocon analysis methods from Grant (2005) and Kuwatani and others (2020). Analytical values that were too small or large to reasonably fit on the isocon diagram were scaled either up or down (table 12).

The isocon analysis in table 11 indicates trace ele-

ment gains or losses illustrated by positive or negative values for $\Delta C/C_{UA}$ and ΔC. The trace elements Ba, Co, Rb, and Sr have negative values for $\Delta C/C_{UA}$ and ΔC, indicating a loss, and the rest of the elements have positive values, indicating a gain compared to unaltered granite. Elements plotting above the reference isocon in figure 13 indicate a compositional gain and those plotting below the reference isocon indicate a loss. The greater the positive values for ΔC (table 11), the greater the gain compared to unaltered granite. For example, As has the highest positive ΔC value and plots the highest on the isocon diagram, suggesting this element had the most gain compared to unaltered granite.

Elements plotting above the reference isocon indicate the hydrothermal fluids were enriched in these elements, and those plotting below the reference isocon indicate deficient concentrations. Compared to unaltered granite, elements with positive ΔC values represent anomalous concentrations and those with negative ΔC values represent non-anomalous concentrations. Gold and tellurium were not plotted on the isocon diagram because Au was not analyzed for the granite samples and Te is below the detection limit for granite (table 10). Analytical results revealed ore grade concentrations of Au and Ag from eight vein samples taken from eight different mining properties (appendix B), and Te was

Table 11. Isocon analysis of ICP-MS averages in parts per million (ppm) for quartz veins.

Elements	C_{UA}	C_{QV}	C_{QV}/C_{UA}	$\Delta C/C_{UA}$	ΔC
Ag	0.59	322.2	546.1	545.1	321.6
As	3.1	805.8	259.9	258.9	802.7
Ba	830.0	195.2	0.235	-0.765	-634.8
Bi	0.06	3.6	60.0	59.0	3.54
Co	10.8	7.5	0.694	-0.306	-3.3
Cs	6.2	16.7	2.69	1.69	10.5
Cu	26.0	169.5	6.52	5.52	143.5
Li	33.2	111.0	3.34	2.34	77.8
Mo	2.8	53.0	18.93	17.93	50.2
Pb	15.5	152.3	9.83	8.83	136.8
Rb	119.8	99.1	0.827	-0.173	-20.7
Sb	0.57	115.8	203.2	202.2	115.2
Sr	525.6	59.3	0.113	-0.887	-466.3
Tl	0.73	2.0	2.74	1.74	1.27
W	1.3	6.3	4.85	3.85	5.0
Zn	9.5	115.9	12.2	11.2	106.4

Note. C_{UA}, component averages for unaltered granite; C_{QV}, component averages for quartz veins; C_{QV}/C_{UA}, slope of data points defining isocon; $\Delta C/C_{UA}$, gain or loss of elements compared to unaltered granite, negative numbers indicate a loss, positive numbers indicate a gain; ΔC, gain or loss of elements in ppm.
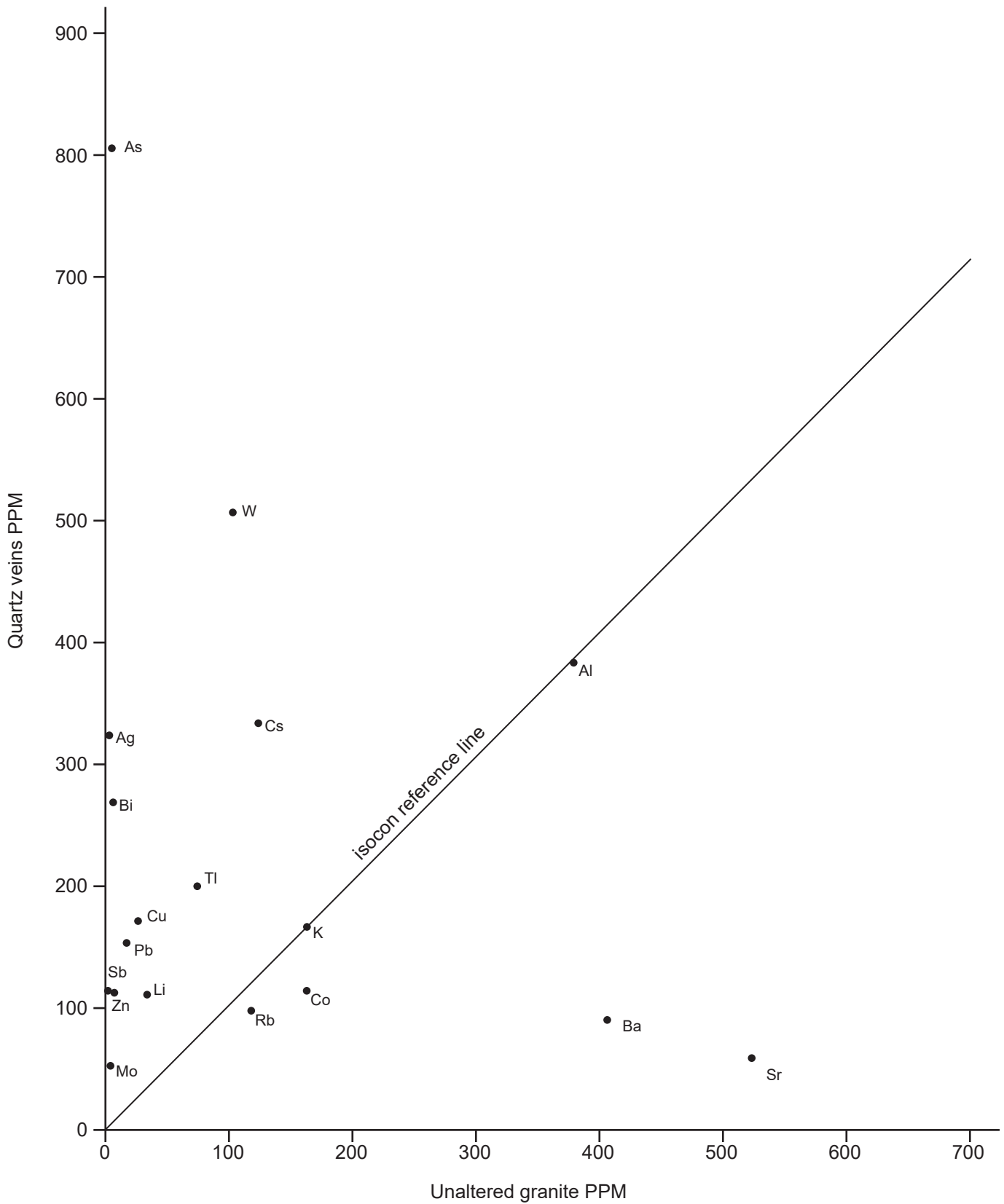
Figure 13. Isocon diagram based on data from tables 11 and 12 for quartz veins. Isocon reference line based on Al and K analysis for unaltered granite and sericitic-argillic alteration from figure 7 and data from table 7.

Table 12. Scaled ICP-MS averages in ppm for quartz veins.

Elements	C_{UA}	C_{QV}	Scale	C_{UA} Scaled	C_{QV} Scaled
Ba	830.0	195.2	0.5	415	96.6
Bi	0.06	3.6	75	4.5	270
Co	10.8	7.5	15	162	112.5
Cs	6.2	16.7	20	124	334
Tl	0.73	2.0	100	73	200
W	1.3	6.3	80	104	5.4

Note. C_{UA}, component averages for unaltered granite; C_{QV}, component averages for quartz veins; scale, factors used to scale up or down ICP-MS data to fit isocon plot; C_{UA} scaled, scaled components for unaltered granite; C_{QV} scaled, scaled components for quartz veins.

detected in 11 out of 29 quartz vein samples (table 10, appendix B).

QUARTZ CATHODOLUMINESCENCE AND TRACE ELEMENTS

Quartz is the most common mineral in the Oro Fino veins and found throughout the district. Hand specimens, cut slabs, and thin sections show quartz forming multiple generations. Quartz replaces brecciated host rock assimilated into the veins, and multiple quartz generations fill open spaces in the silicified granite. Quartz forms comb structures on vein margins, replaces bladed calcite, and occurs as crystals in open vugs and chalcedony bands. The paragenetic sequence and trace elements of these quartz generations were used to trace the physical and chemical changes that took place during vein development.

Cathodoluminescence (CL) response in conjunction with trace Ti and Al enables us to identify different quartz generations and trace their paragenetic sequence (figs. 14–17). Cathodoluminescence analysis was conducted at the scanning electron microscope laboratory located at Montana State University, Bozeman, using a Jeol JSM-6100 scanning microscope equipped with an Oxford CL detector. To measure the CL response, the SEM was set for an acceleration voltage of 10 kV, a working distance of 15 mm, and a magnification of 190X.

Quartz with distinct CL responses was analyzed for titanium and aluminum using the Cameca SX 100 electron microprobe at the Electron Microprobe Laboratory, College of Earth, Ocean, and Atmospheric Sciences, Oregon State University, Corvallis, Oregon. Detection limits were 21 ppm for Ti and 13 ppm for Al, which were determined using a quartz standard from Shandong province, China (Audétat and others, 2015).

The vein quartz cathodoluminescence ranges from no response, giving a black image, to a strong response, yielding bright white (figs. 18–21). Quartz crystals that precipitated in open spaces showed oscillatory growth consisting of black to white concentric growth zones. The CL images revealed four quartz generations with variable Al and Ti concentrations.

Huang and Audétat (2012) derived a thermobarometer for quartz crystallization based on Ti concentration and pressure. Quartz growth rate has an impact on the concentration of Ti, where a slow growth rate will concentrate more Ti than a rapid growth rate (Huang and Audétat, 2012). Quartz grown from hydrothermal fluids has a variable growth rate, making the thermobarometer more suitable for quartz crystallized from a magma. Acosta and others (2018) successfully applied the thermobarometer to hydrothermal quartz veins from the Butte district and obtained temperatures similar to those from fluid inclusion temperatures. Quartz from the Oro Fino veins having a Ti concentration below the detection limit (21 ppm) could be a reflection of rapid crystallization and precipitation at low temperatures.

Aluminum concentration in hydrothermal quartz does not reflect precipitation temperature but may reflect aqueous Al concentration, which is pH dependent (Rusk and others, 2008). Rusk and others (2008) determined that in the presence of kaolinite as an equilibrating mineral and at a temperature of 200ºC and pH of 1.5, Al solubility in hydrothermal fluids is 6 orders of magnitude higher than at a pH of 3.5 in the presence of muscovite. At high temperatures of 500ºC, Al solubility and pH vary only slightly regardless of the equilibrating mineral. Rusk and others (2008) measured quartz Al concentrations exceeding 2,000 ppm in Butte main stage veins bordered by alteration kaolinite, indicating acidic pH in some stages of vein development. The large Al solubility in low-pH hydrothermal fluids suggests quartz enriched in Al may have precipitated from Al-rich acidic fluids (Rusk and others, 2008). At low temperatures, quartz may also incorporate significant quantities of Al upon precipitation due to kinetic factors and does not reflect chemical equilibrium (Rusk and others, 2006). Kaolinite and sericite identified from the Oro Fino mining district quartz veins and altered wall rocks indicate periods of acidic hydrothermal fluids.

First stage quartz occurs as stringers and veinlets filling fractures in brecciated granite and contributes to

Al and Ti distribution of
1st generation quartz
vein in brecciated quartz

	Al ppm	Ti ppm	T(C)
1.	137	158	779
2.	91	179	797
3.	4,752	<21	
4.	11,802	116	600
5.	5,424	272	702
6.	95	104	729
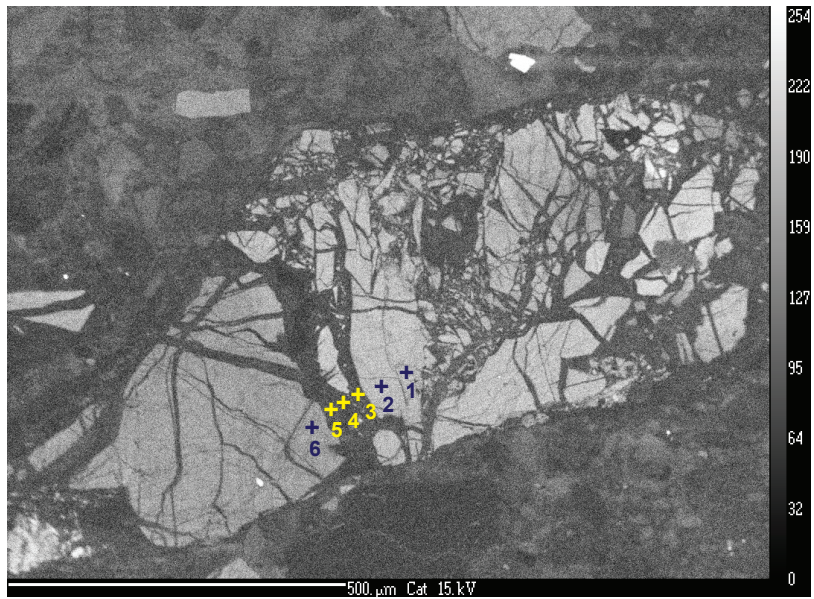
Al and Ti distribution of
assimilated quartz and
2nd generation low
temperature quartz vein

	Al ppm	Ti ppm	T(C)
1.	125	102	724
2.	85	90	710
3.	123	85	705
4.	1,888	<21	
5.	3,835	<21	
6.	2,435	<21	
7.	142	109	732
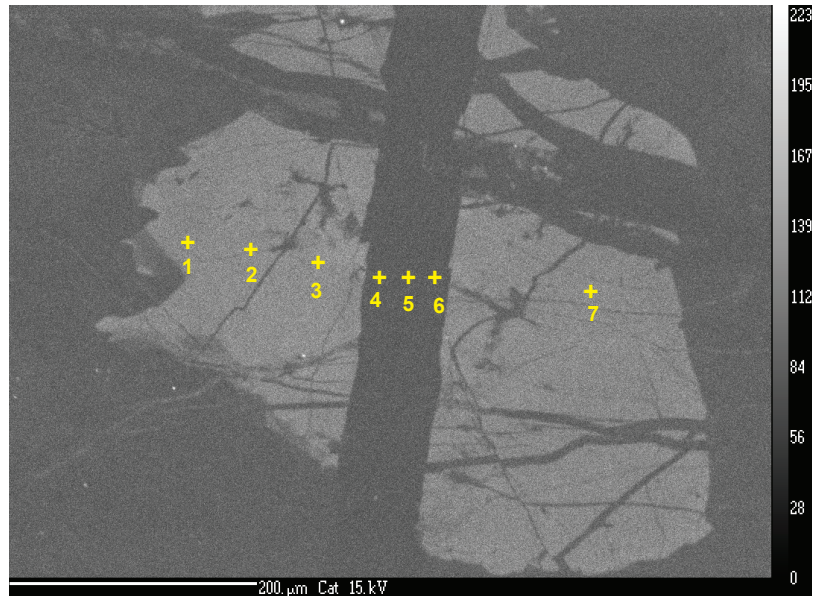
Figure 14. Cathodoluminescence response of quartz showing first and second generation quartz veins cutting brecciated primary granite quartz grains and EMP analysis points with corresponding Al and Ti analytical results and calculated crystallization temperatures using formula from Huang and Adétat (2012). ppm, parts per million; T(C), degrees centigrade.

granite silicification. These quartz strings and veinlets occur along the vein contacts within a fractured and brecciated granite host. The first generation quartz veinlets revealed by CL imaging (fig. 14) gave a low CL response and appear as black veinlets in brecciated plutonic quartz grains of the host granite, which give a bright to moderate CL response. The fractured anhedral primary quartz grains are the remains of the original granite, which was brecciated, al-

tered, and assimilated into the quartz veins. The brecciated quartz grains have a Ti concentration ranging from 85 to 179 ppm and Al concentration from 85 to 142 ppm.

The Butte Granite hosting the veins may have crystallized at the same depth as the Butte district, which crystallized at 6 to 9 km (Houston and Dilles, 2013). Using hornblende barometry, Houston and Dilles (2013) determined the Butte Granite crystal-

Al and Ti distribution in 3rd generation quartz crystals associated with pyrite

	Al ppm	Ti ppm
1.	3,441	<21
2.	2,947	<21
3.	2,550	<21
4.	359	<21
5.	644	<21
1.	1,182	<21
2.	57	<21
3.	1,102	<21

Al and Ti distribution of assimilated quartz and 4th generation low temperature quartz vein

	Al ppm	Ti ppm
1.	0	<21
2.	0	<21
3.	0	<21
4.	0	<21
5.	0	<21
6.	0	<21
7.	0	<21
8.	0	<21
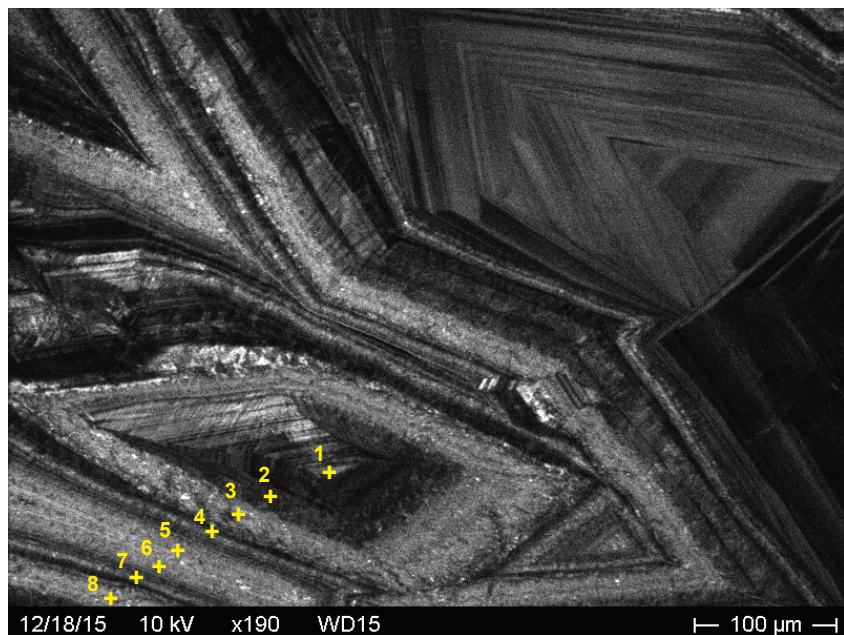
Figure 15. Cathodoluminescence response of third and fourth generation quartz crystals showing oscillatory growth and EMP analysis points with corresponding Al and Ti analysis. ppm, parts per million.

lized at a pressure of 2 to 2.5 kbar. Based on pressure determinations by Houston and Dilles (2013), a pressure of 2 kbar for the crystallization of the host granite and the measured Ti concentration was used to estimate the crystallization temperature from the thermobarometer derived by Huang and Adétat (2012). An estimated crystallization temperature ranging from 705º to 797ºC was determined, which is expected from quartz that crystallized from a granitic magma.

The first stage quartz vein (fig. 14) has a variable Ti concentration ranging from <21 to 272 ppm and Al concentration ranging from 4,752 to 11,802 ppm. Temperatures estimated from the Ti concentration using the thermobarometer derived by Huang and Adétat (2012) and a pressure of 0 and 0.15 kbar (from fluid inclusion data) range from 506º to 597ºC and 600º to 702ºC, respectively, which are abnormally high for quartz that crystallized from a hydrothermal fluid. The abnormally high Ti concentrations

Al and Ti distribution of 4th generation quartz crystals

	Al ppm	Ti ppm
1.	0	<21
2.	0	<21
3.	0	<21
4.	0	<21
5.	0	<21
6.	0	<21
7.	0	<21
8.	0	<21
9.	0	21

Figure 16. Cathodoluminescence response of fourth generation quartz crystals showing oscillatory growth and EMP analysis points with corresponding Al and Ti analysis. ppm, parts per million.

were most likely caused by dissolution of the primary quartz host by the invading hydrothermal fluids, which incorporated excessive Ti into the crystallizing quartz vein. Probe point 3 (fig. 14) with Ti <21 is a reflection of the true Ti content for first stage quartz veins and is what would be expected for a low-temperature hydrothermal vein (Rusk and others, 2008). The high Al content above 2,000 ppm and the close proximity to sericite, illite, and kaolinite in the altered granite suggest the early quartz vein crystallized from an acidic aqueous fluid saturated in Al.

Cutting and offsetting the first generation quartz veinlets are second generation quartz veinlets that also have a low CL response and appear as black on CL images (fig. 14). These veins stand out in contrast to brecciated plutonic quartz grains of the host gran-
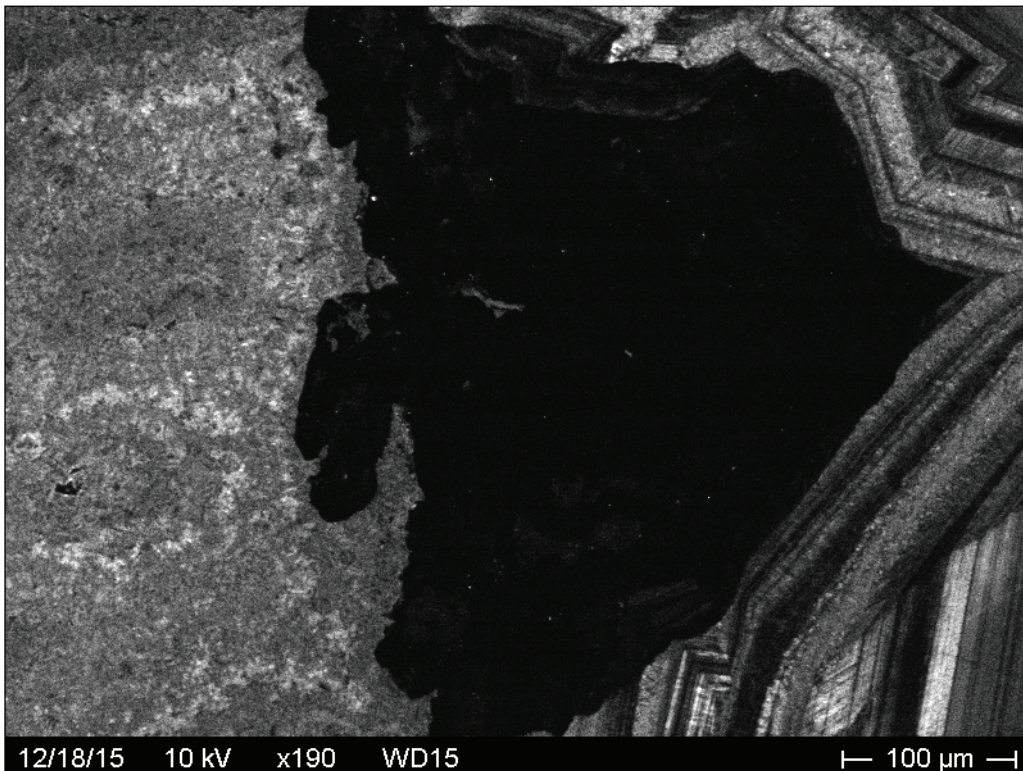
Figure 17. Cathodoluminescence response of silicified granite and fourth generation quartz showing oscillatory growth overprinting pyrargyrite and acanthite grain.

ite, which give a moderate to bright CL response. The Ti concentration is <21 ppm, reflecting a low-temperature origin for these veins or rapid precipitation. The Al concentration ranges from 1,888 to 3,835 ppm and is in close proximity with kaolinite, sericite, and illite, suggesting these veins precipitated from an aqueous solution less acidic than the first generation veins.

Third generation quartz is related to sulfide precipitation and developed in conjunction with metal sulfide mineralization. The third quartz generation fills open spaces in brecciated first and second generation vein quartz and occurs as bands of euedral to anhedral coarse-grained crystals. Third generation quartz is accompanied by sulfides and occurs as well-formed crystals with oscillatory CL banding, as in figure 15, which shows bladed quartz enclosed by euhedral quartz crystals. Pyrite (black Cl) fills open spaces between the quartz crystals. The bladed quartz is probably pseudomorphic after bladed calcite, which is common in the veins (fig. 18).

The bladed quartz crystal has a Ti concentration <21 ppm and Al shows a zoning pattern reflecting the CL response. The core of the crystal has an Al concentration of 57 ppm and the edges have an Al concentration of 1,102 ppm and 1,182 ppm (fig. 15). The crystal enclosing the bladed crystal has a Ti concentration <21 ppm and Al concentrations that increase from the core to the margin. Aluminum concentrations near the center of the crystal range from 359 ppm to 644 ppm and increase outward from 2,550 ppm to 3,441 ppm at the margin (fig. 15).

A fourth quartz generation gives a CL response of concentric white to black bands showing fine- to coarse-grained crystal outlines and coarse-grained crystals filling open spaces (figs. 15–17). This quartz generation occurs as concentric bands of chalcedony with fine-grained quartz crystals filling open spaces, forming a colloform texture (fig. 19). The fourth quartz generation fills fractures and lines open spaces in brecciated second and third quartz generations. The CL response for coarse-grained quartz crystals
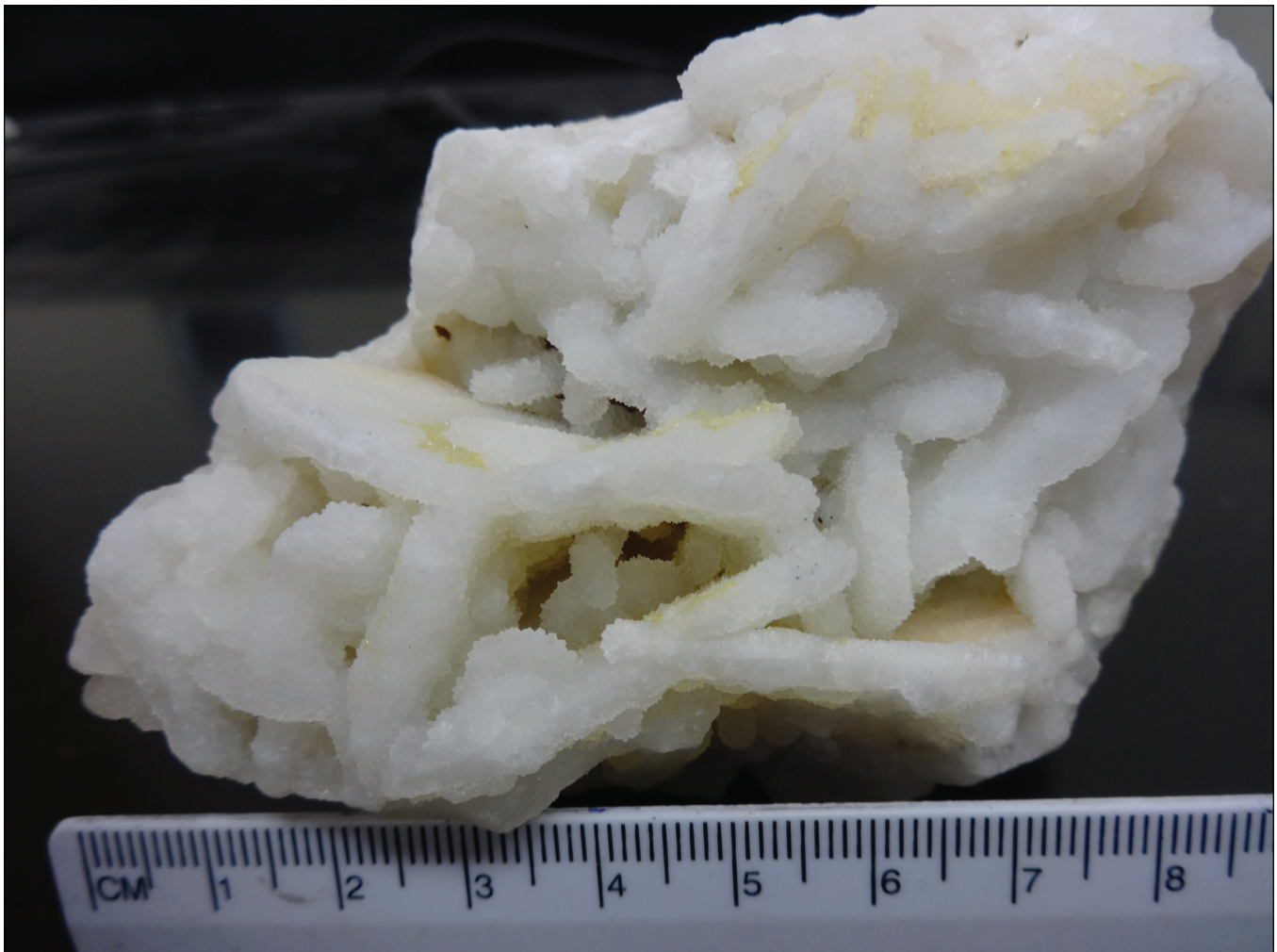
Figure 18. Quartz pseudomorphing bladed calcite, specimen from the Ruby vein (location 10, fig. 2, and plate 1).
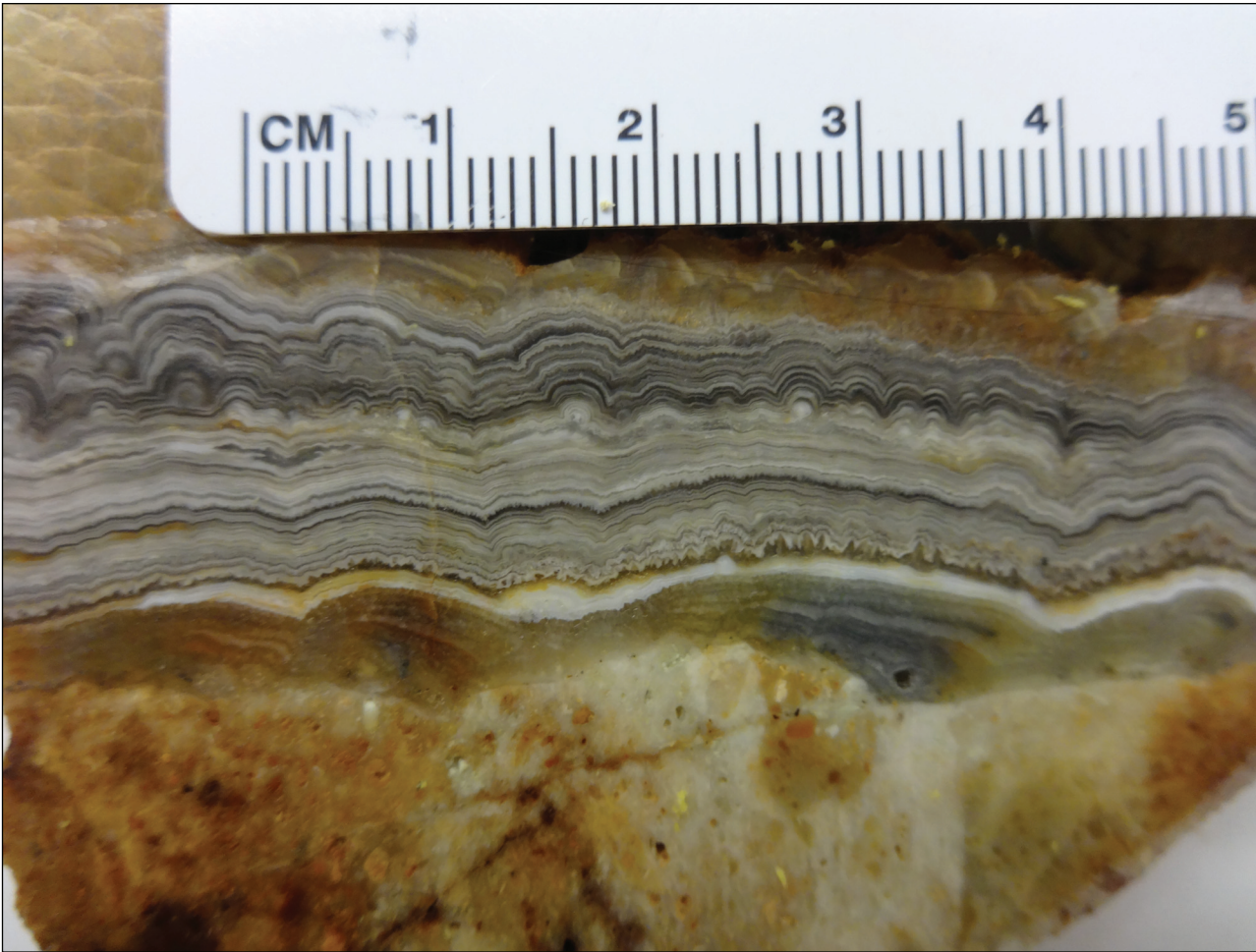
Figure 19. Chalcedony showing banded colloform texture from rapid decompression of hydrothermal fluids. Sample from dump of caved adit at location OF-28.

shows oscillatory growth consisting of black to white bands (fig. 16). Aluminum was not detected in these crystals and the Ti concentration is <21 ppm. Concentric fine-grained quartz bands giving a white to black CL response, illustrated in figure 17, show oscillatory growth bands. EMPA showed no variations in the Al or Ti concentrations among the different CL intensities.

The Al deficiency in the recrystallized chalcedony may be related to kinetics. Concentrically banded chalcedony forming a colloform texture indicates rapid silica deposition (Moncada and others, 2012). Since Al substitution in quartz is related to kinetics (Rusk and others, 2006), the rapid deposition of the original chalcedony may not have allowed sufficient time to incorporate Al into the silica. Huang and Adétat (2012) determined that rapid quartz crystallization lowers Ti concentrations. The deficiency of Ti in chalcedony (fig. 16) may reflect rapid crystallization. The cause of the CL response of the recrystallized quartz is unknown since Al and Ti were not detected. The overgrowth of crystallized quartz on silver minerals (fig. 17) suggests silver mineralization took place during deposition of chalcedony.

The first stage is related to the silicification of the host granite and the second stage appears to be the beginning of vein development. The first quartz stage occurs as veinlets in fractured and brecciated host granite. The second stage occurs in fractures as veins and veinlets with minor disseminated pyrite that crosscut the first stage. The third stage formed with base metal mineralization and the fourth stage crystallized with silver–gold mineralization. The third and fourth stages filled open spaces in the fractured and brecciated granite and faults occupied by the veins. Quartz crystallized during the third and fourth stages consists of clear to milky euhedral to anhedral quartz grains and banded chalcedony. Early formed bladed calcite was pseudomorphed by clear to milky quartz during the third stage (fig. 18). Included in third and fourth stage quartz gains are sulfide minerals and euhedral quartz crystals, which enclose sulfide minerals filling open spaces. Fluid inclusions trapped in the third and fourth stages reflect the hydrothermal events that took place when base metal and silver–gold mineralization was taking place.

FLUID INCLUSIONS

To gain an understanding of the salinities and provide temperature estimates and temporal evolution for the hydrothermal fluids that developed the veins, microthermometric measurements of fluid inclusions were conducted. The third and fourth quartz stages identified by cathodoluminescence yielded the best fluid inclusions for analysis. Fluid inclusions in the other quartz stages were too small for analysis. Fluid inclusions were selected from quartz crystals inter-grown with sulfide minerals and bands of coarse-grained crystals filling open spaces and vugs in base metal and silver–gold mineralization stages and from fluorite and baryte veins. Fluid inclusions were ana-lyzed on a Fluid Inc. adapted USGS-type gas-flow heating/freezing stage mounted on an Olympus BH-2 microscope located at the Geological Engineering Department, Montana Tech.

Five identified fluid inclusion types were type I, type II, liquid, vapor, and three phase inclusions (fig. 20). Type I inclusions are the most common and consist of liquid and <50 vol% vapor bubble (fig. 20). Type II inclusions are vapor dominated (fig. 20A), and in some the vapor phase exceeds 70 vol% with a thin outer rim of liquid (fig. 20C). Single phase inclusions consisting of all liquid or vapor are common. Three phase inclusions with a halite daughter mineral, liquid, and vapor are rare and occur particularly in quartz intergrown with chalcopyrite (fig. 20D).

Primary and secondary inclusions were identi-fied using the criteria by Roedder (1984). Primary inclusions occur as groups trapped in quartz growth zones. Inclusions in baryte and fluorite crystals occur in healed fractures in rows following fracture planes and as scattered individuals between fracture planes. Secondary inclusions of type I and II occur in healed

fractures in the host crystals. These inclusions are elongated to rounded and occur in rows. Secondary inclusions can give information on the nature of later-stage fluids.

A total of 307 inclusions were analyzed, of which 176 inclusions yielded both homogenization tempera-ture (Th) and wt% NaCl eq data (table 13), 82 type I and II inclusions yielded exclusively Th, 48 liquid inclusions yielded only wt% NaCl eq data, and 1 inclusion generated clathrate on freezing (table 14). Homogenization temperatures and wt% NaCl eq are summarized in table 13, and the complete dataset is shown in appendix C. Primary and secondary type I and II inclusions hosted by quartz, baryte, and fluo-rite homogenized to a liquid phase. Type II inclusions with the vapor phase exceeding 70% of the inclu-sion volume homogenized to vapor and did not yield salinity data. Homogenization temperatures for both type I and type II inclusions were the same for those in assemblages formed of 3D clusters. Fluid salinities for liquid and type I and II inclusions were determined by freezing with liquid nitrogen, then melting the ice and recording the melting temperature (Tm) when the last ice crystal melted. From the Tm, fluid salinity was calculated using the methods by Roedder (1984).

Three phase inclusions with liquid, vapor, and a halite daughter mineral homogenized in steps yielding homogenization and halite dissolution temperatures. Homogenization temperature was reached when both the vapor and halite phases assimilated into the liquid phase, yielding a homogenized liquid filled inclusion. To determine salinities, inclusions were heated until the halite completely dissolved, yielding a dissolution temperature. The wt% NaCl eq was calculated from the halite dissolution temperature using the method determined by Sterner and others (1988).

Table 13. Summary of 176 fluid inclusions that yielded both salinity and Th data from veins throughout the Oro Fino district.

Inclusion Types	Type I + Halite	Type I and II	Type I and II	Type I and II
Host mineral	Quartz	Quartz	Quartz	Fluorite, baryte, quartz
Th°C range	197.1–362.7	175.2–314.7	192.9–346.5	129.6–189.5
Th°C average	273.5	232.9	244.4	167.6
Tm°C halite range	166.0–293.4			
Tm°C halite average	212.4			
Tm°C ice range		-5.7 to -11.9	0.0 to -4.1	0.0 to -1.4
Tm°C ice average		-8.4	-1.1	-0.4
Wt% NaCl eq range	30.34–37.66	8.81–15.99	0.0–6.58	0.0–2.4
Wt% NaCl eq average	32.70	12.18	1.5	0.65
n for all averages	17	16	87	56

Note. Th°C, temperature of homogenization to liquid in degrees centigrade; Tm°C halite, melting temperature for halite in degrees centigrade; Tm°C ice, melting temperature for ice in degrees centigrade; Wt% NaCl eq, weight percent NaCl equivalent; *n*, number of inclusions used for averages.
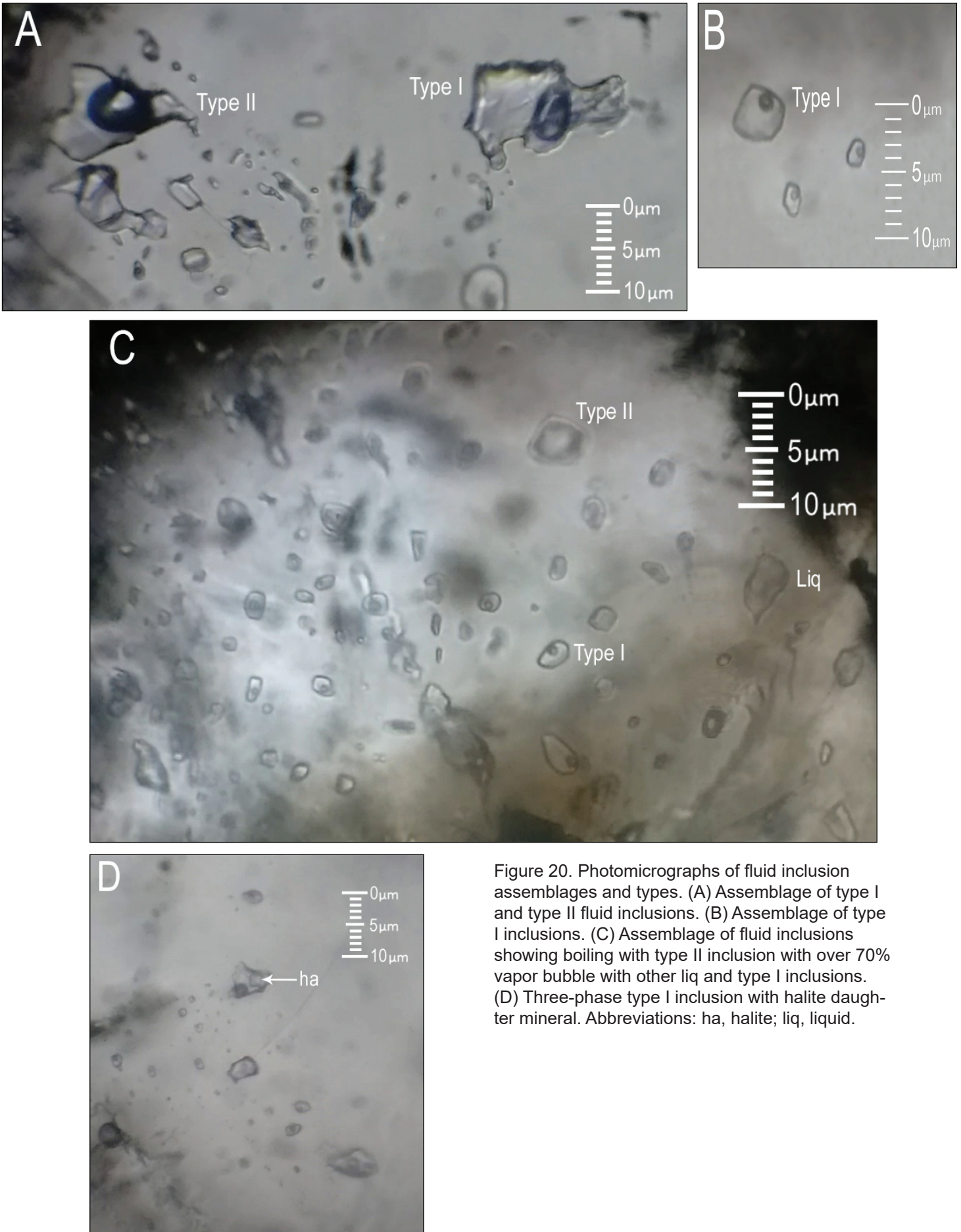
Figure 20. Photomicrographs of fluid inclusion assemblages and types. (A) Assemblage of type I and type II fluid inclusions. (B) Assemblage of type I inclusions. (C) Assemblage of fluid inclusions showing boiling with type II inclusion with over 70% vapor bubble with other liq and type I inclusions. (D) Three-phase type I inclusion with halite daughter mineral. Abbreviations: ha, halite; liq, liquid.

Table 14. Summary of 48 liquid inclusions that yielded salinity data, 82 type I and II inclusions that yielded only Th data, and one type I inclusion that formed clathrate on freezing.

Inclusion Type	Liquid	Type I and II	Type I Clathrate
Host mineral	Quartz	Quartz, fluorite, baryte	Quartz
Th°C range		148.6–406.1	442.1
Th°C average		206.0	442.1
Tm°C clathrate			9.2
Tm°C ice range	0.0 to -21.6		
Tm°C ice average	-1.67		
Wt% NaCl eq range	0.0–23.77		1.64
Wt% NaCl eq average	2.23		1.64
n for all averages	48	82	1

Note. Th°C, temperature of homogenization to liquid in degrees centigrade; Tm°C clathrate, melting temperature for clathrate in degrees centigrade; Tm°C ice, melting temperature for ice in degrees centigrade; Wt% NaCl eq, weight percent NaCl equivalent; n, number of inclusions used for averages.

Temperature plotted against salinity (fig. 21) reveals four distinct fields representing salinity changes for the hydrothermal fluid and equivalent temperatures. One fluid inclusion with the highest Th (442.1°C) generated clathrate on freezing, indicating dissolved CO_2 is present in the trapped fluid (table 14). Using the equation from Darling (1991), a salinity of 1.64 wt% NaCl eq was calculated from the clathrate melting temperature (table 14). Most fluid inclusions reflect the low salinity of the high-temperature inclusion, averaging 1.5 wt% NaCl eq. (table 13), and plot in a field near the bottom of figure 21. The high-temperature inclusion was isolated and trapped under non-boiling conditions, preserving dissolved CO_2 in the trapped fluid.

Bodnar and others (1985) determined that coexisting liquid and vapor-rich inclusions indicate boiling conditions. The Oro Fino inclusions show evidence of boiling consisting of coexisting vapor, liquid, and type I and II inclusions. Boiling conditions drive CO_2 out of hydrothermal fluids (Simmons and others, 2005), resulting in a CO_2-free fluid trapped in the Oro Fino fluid inclusions. Boiling causes increases in salinity by generating an evaporative concentration of salts caused by steam loss in open systems (Cooke and Simmons, 2000). The two fields with the highest salinities (fig. 21), ranging from 8.81 to 15.99 and 30.34 to 37.66 wt% NaCl eq (table 13), are interpreted to represent a high-salinity fluid generated by boiling conditions. Temperature is also affected by boiling, which causes water vaporization and steam loss resulting in temperature decreases (Lynch and others, 1990). The decrease in temperature from the initial hydrothermal fluid, represented by the carbon dioxide-enriched fluid inclusion, to the lower temperature fluid inclusions (fig. 21, tables 13 and 14) is related to boiling in the hydrothermal system.

Fluorite and baryte fill fractures and open spaces in fractured and brecciated vein quartz, and fluorite occurs as massive veins in fractured white quartz veins, indicating a final crystallization during vein development. Primary fluid inclusions trapped in fluorite, and baryte and secondary inclusions trapped in quartz and fluorite, plot in a field with the lowest temperatures and salinities (fig. 21). These inclusions could represent the close of vein development and have salinities ranging from 0.0 to 2.4 wt% NaCl eq and lowest temperatures ranging from 129.6° to 189.5°C (table 13).

Homogenization temperatures illustrated on a histogram plot in figure 22 show two distinct populations between 120° to 190°C and 190° to 440°C. The population of inclusions from 120° to 190°C are hosted by baryte, fluorite, and quartz, and secondary inclusions trapped in healed fractures in quartz and fluorite. These lower temperature inclusions may represent an influx of meteoric water into the hydrothermal system. The population of inclusions between 190° and 360°C represents a fluid trapped during mineralizing and boiling events, and suggest mineralization took place within this temperature range. Hydrothermal fluids with carbon dioxide are exsolved from cooling magmas (Sharma and Srivastava, 2014), suggesting the fluid inclusion with the highest Th (442.1°C) with dissolved CO_2 in the trapped fluid may have originated from a magmatic source.

Illustrated on a histogram (fig. 23) are three distinct populations of 0 to 6, 7 to 16, and 23 to 37 wt% NaCl eq. Most fluid inclusions fall within the 0 to 7 wt% NaCl eq population, which is typical for epithermal systems that commonly have salinities ranging from 0 to 10 wt% NaCl eq (Simons and others, 2005). Hydrothermal fluids with a magmatic origin also have salinities ranging from 0 to 10 wt% NaCl eq and can be as high as >50 wt% NaCl eq depending on the physicochemical conditions of the magmatic source (Sharma and Srivastava, 2014). The fluid inclusion with dissolved CO_2, high Th (442.1°C), and a salinity of 1.64 wt% NaCl eq (table 14) falls in the range of a low-salinity magmatic fluid. The presence of CO_2 in the trapped fluid and high Th (for epithermal veins) further suggest a magmatic origin for the hydrothermal fluid trapped in this inclusion.
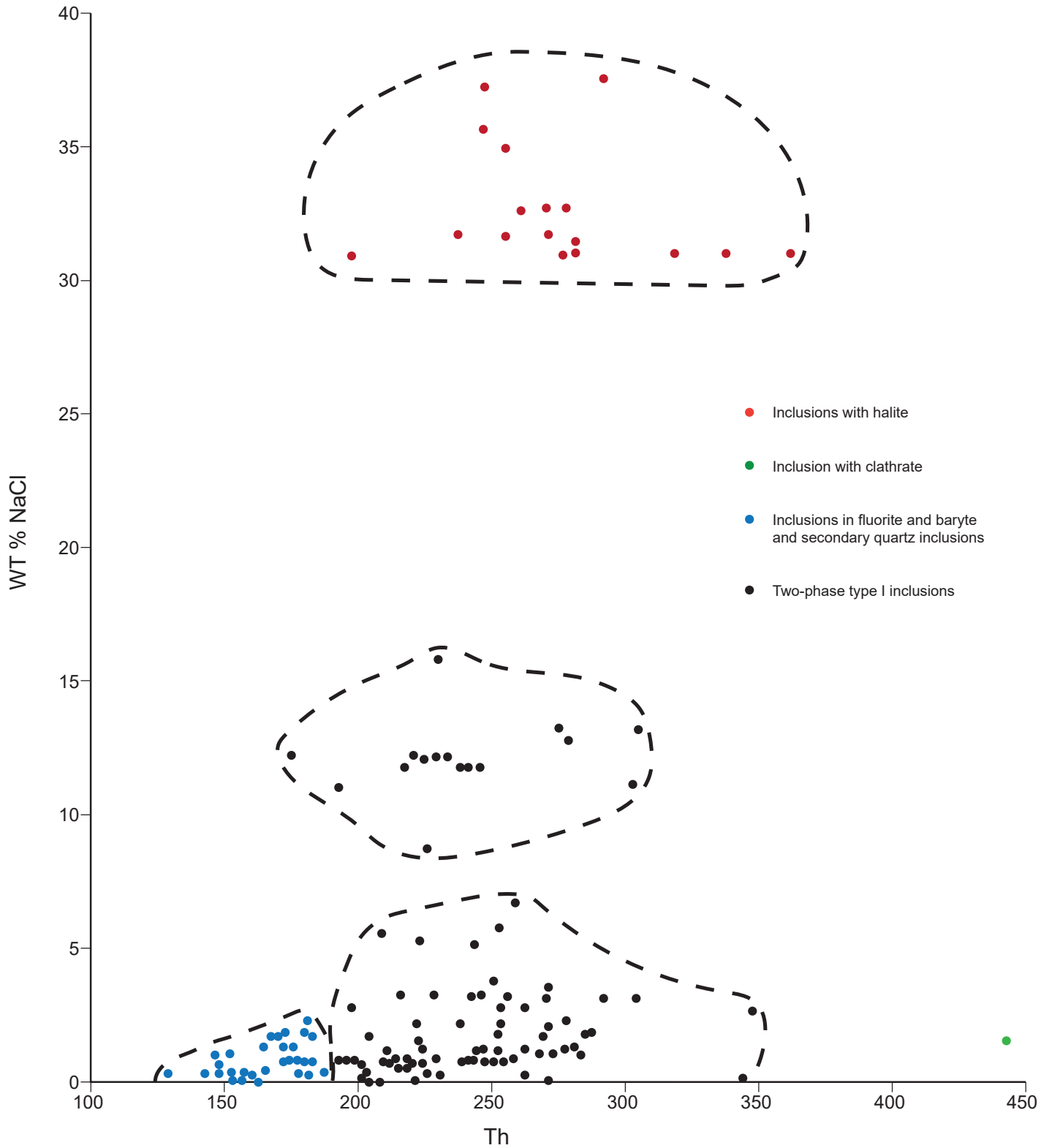
Figure 21. Plot of fluid inclusion homogenization temperature versus weight % equivalent NaCl showing different fields representing changes from low to high salinity and temperature variations. Th, homogenization temperature in degrees centigrade. WT% NaCl, weight % equivalent NaCl.
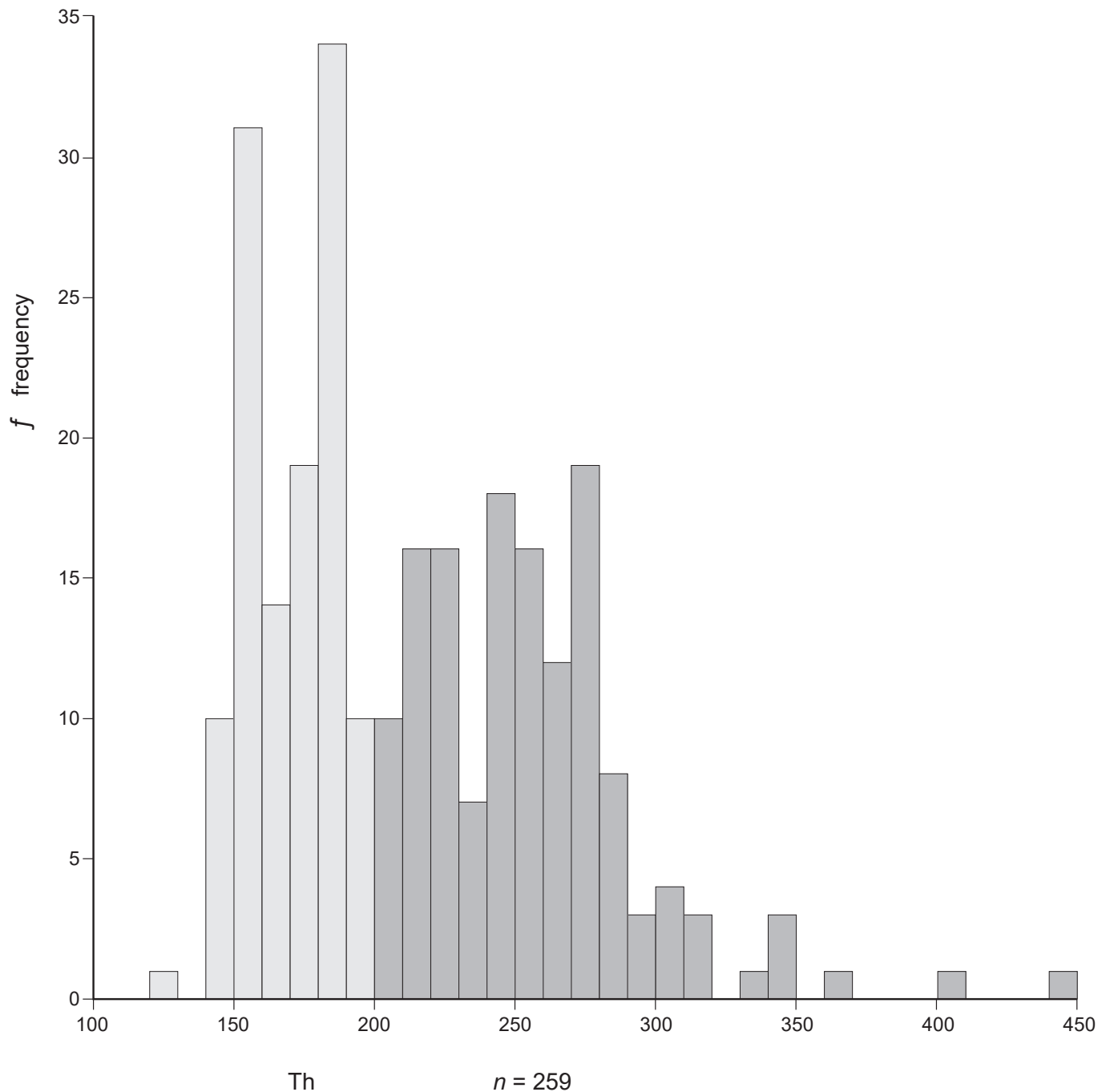
Figure 22. Histogram plot for 259 type I and II fluid inclusion homogenization temperatures showing two populations. Th, temperature of homogenization in degrees centigrade. Complete data set shown in appendix C.

Most fluid inclusions were trapped at a temperature ranging from 193° to 347°C, with salinities varying from 0 to 6.50 wt% NaCl eq and averaging 1.6 wt% NaCl eq. Using the average salinity and temperature range, fluid densities determined from a diagram in Roedder (1984) ranged from 0.60 to 0.90 g/cm³. Applying these densities to the boiling curve on a diagram from Fisher (1976), a pressure of near 0 to 150 bars was determined, assuming NaCl was the only salt present in the fluid inclusions. The pressure indicates the Oro Fino hydrothermal system was a shal-

low system that formed near the paleo surface. The common occurrence of assemblages of vapor-rich and liquid-rich inclusions suggest boiling was common during mineralization. Physical evidence that boiling was taking place is the presence of bladed calcite, quartz replacing bladed calcite, and colloform quartz banding (Simmons and Browne, 2000; Moncada and others, 2012). From the fluid inclusion evidence, the Oro Fino hydrothermal system was a shallow system and evolved from the mixing and boiling of a magmatic and meteoric fluid.

SULFUR ISOTOPES

Sulfur isotope analyses on 29 sulfide samples were conducted at the U.S. Geological Survey Crustal Geophysics Geochemistry Science Center in Denver, Colorado. Analysis involved a vacuum-line conversion to SO_2 followed by an elemental analyzer using a Thermo Delta Plus XP mass spectrometer. Samples were extracted under a microscope from cut slabs using a Dremel tool and diamond bit, or were hand picked from specimens. All isotope values are reported in the standard $\delta^{34}S$‰ notation relative to Vienna Canyon Diablo Troilite (VCDT) standard.

Sulfur isotopic data for 27 pyrite and 2 chalcopyrite samples (fig. 24, appendix D) show two different $\delta^{34}S$ populations: one that ranges from -3 to 2‰ and another that ranges from 3 to 9‰. The -3 to 2‰ samples are from locations that have pyrite intergrown with schorl. Pyrite and chalcopyrite intergrown with schorl is brecciated with quartz filling open spaces between breccia fragments. The brecciated sulfides are early and crystallized during or shortly after schorl crystallization. Subsequently precipitated pyrite and chalcopyrite sampled from the rest of the vein locations yield $\delta^{34}S$ values within the 3 to 9‰ population.

DISCUSSION

The Oro Fino mining district veins are hosted by the Butte Granite of the Boulder Batholith, and age dating suggests they formed at the end of Eocene Lowland Creek volcanism. Age dating of the veins indicate they developed 45.26 ± 0.11 Ma after active Lowland Creek volcanism eruptions took place at 52.9 to 48.6 Ma (Dudás and others, 2010). Located east of the district is a caldera that developed as a result of Eocene Lowland Creek volcanism. As the caldera cooled, a hydrothermal system was initiated on the caldera margin and west of the caldera ring fracture. The hydrothermal system could have been driven by intrusions following the last volcanic event that developed the Lowland Creek volcanic field. Fractures in the Butte
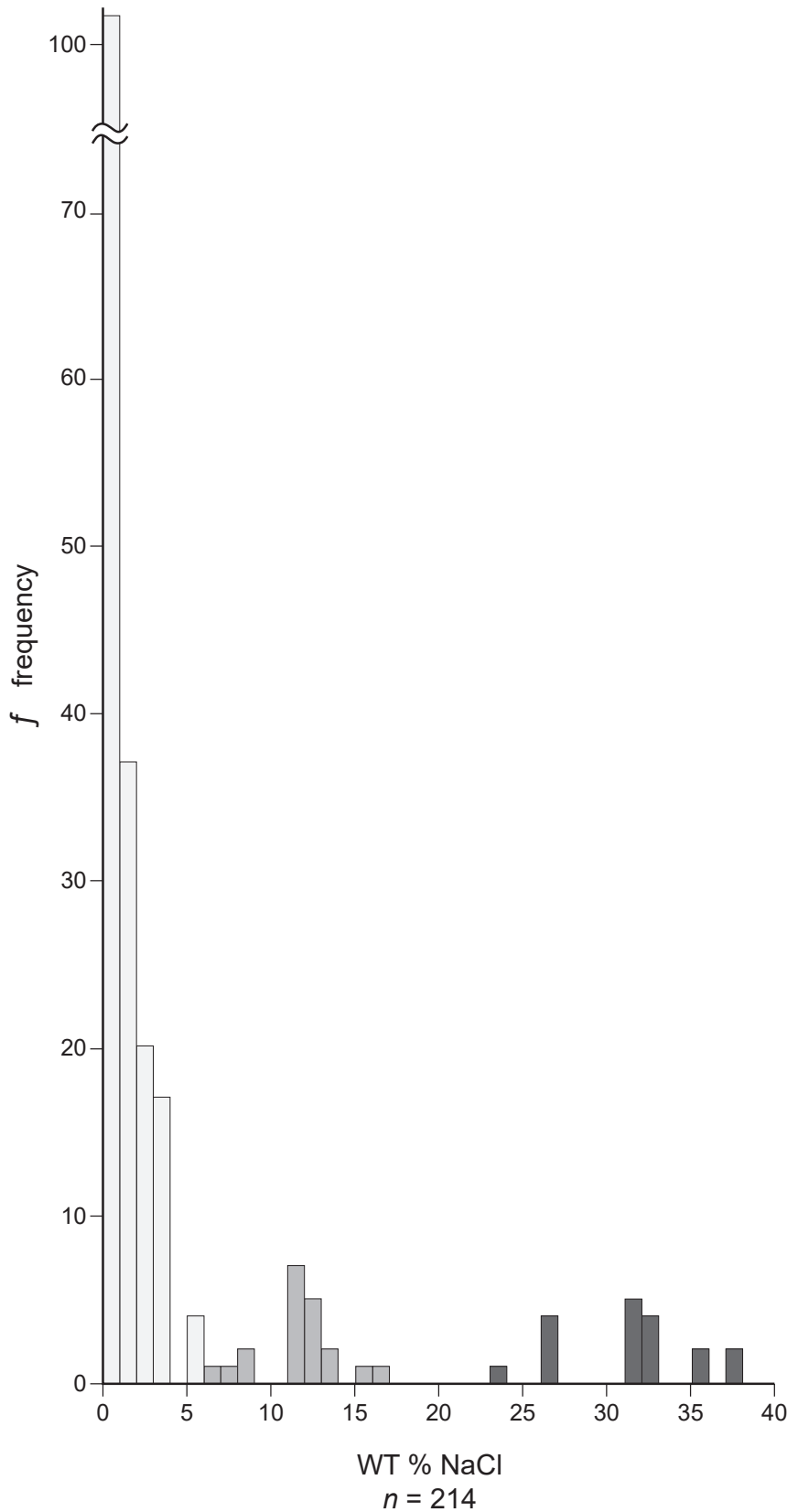
Figure 23. Histogram plot for fluid inclusion salinities showing salinity changes. WT % NaCl, weight % NaCl equivalent. Complete data set shown in appendix C.
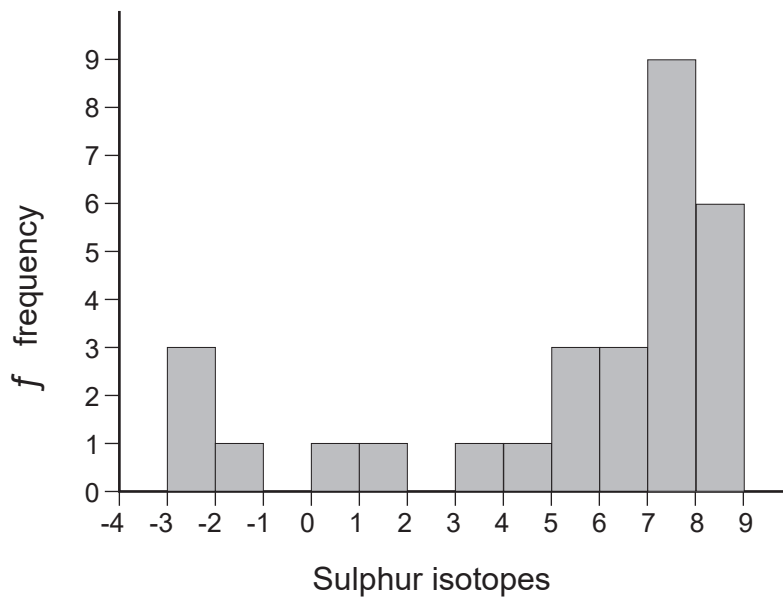
Figure 24. Histogram plots for sulfur isotope values (‰ relative to CDT standard) for pyrite and chalcopyrite. Complete data set listed in appendix D.

Granite provided channel ways for hydrothermal fluids to vent to the surface, thus leading to the development of the Oro Fino veins.

The veins in the Oro Fino mining district have many features found in both epithermal low and intermediate sulfidation systems, and can be classified as a low to intermediate sulfidation system. Alteration adjacent to the Oro Fino veins contains variable amounts of adularia, sericite, illite, kaolinite, and pyrite with quartz and chalcedony, an assemblage that is characteristic of low and intermediate sulfidation veins (Cooke and Simmons, 2000). Silicification of the host granite and the strongly elevated Al concentrations in vein quartz indicate higher sulfidation levels than low sulfidation systems. Platy calcite pseudomorphed by quartz (fig. 18), and vein quartz forming crustiform and colloform bands (fig. 19) are a common feature of low sulfidation veins, indicating periods of low sulfidation (Simmons and others, 2005; Cooke and Simmons, 2000). For both low and intermediate sulfidation systems, fluid inclusions generally show a temperature range from 150º to 300ºC and salinities <3.5 wt% NaCl equiv (Cooke and Simmons, 2000). Most fluid inclusions from the Oro Fino veins fall within the salinity and temperature range that is characteristic of a low to intermediate sulfidation system.

The Oro Fino veins contain trace elements characteristic of epithermal veins, including Au, Ag, As, Bi, Li, Mo, Pb, Sb, Tl, W, and Zn (Weissberg, 1969; Silberman and Berger, 1985; Ewers and Keays, 1977; Simmons and Browne, 2000; Simmons and others,

2016). Trace Cs, Cu, and Te occur in anomalous concentrations in the Oro Fino veins (table 10 and appendix B) and occur in fluids from active hydrothermal vents, precipitates, and sulfide minerals in modern volcanic back-arc environments (Fouquet and others, 1993; Berkenbosch and others, 2012). Comparison of trace elements found in modern back-arc environments with trace elements from the Oro Fino veins (table 10) suggests a genetic link with back-arc magmatism. Trace elements further show the Oro Fino veins are a silver-dominated system with a silver range (0.45–3,000 ppm) dominating over a gold range of (0.002–10.95 ppm). Silver dominating over gold and the presence of other trace elements As, Sb, and Tl are characteristic of a shallow (0–300 m) low to intermediate sulfidation epithermal system (Hedenquist and others, 2000).

Hydrothermal System Evolution

Fluid inclusion, sulfur isotope, cathodoluminescence and EMP analyses, along with alteration and vein mineralogy, suggest that Oro Fino veins developed from an evolving hydrothermal fluid. Fluid inclusion data from one inclusion show a period when the hydrothermal fluids had a high CO_2 concentration, low salinity (1.66 wt% NaCl eq), and high Th (442.1ºC; table 14). Magmatic derived fluids have elevated concentrations of CO_2 and low salinities (Sharma and Srivastava, 2014), suggesting the fluids trapped by the fluid inclusion had a magmatic origin. EMP analysis of the first quartz stage veinlets (fig. 14) reveals a high Al concentration (up to 11,802 ppm), indicating the quartz crystallized from an Al-saturated aqueous fluid with an acid pH. Sulfur isotope data from early pyrite and chalcopyrite that crystallized and is intergrown with schorl showed a depletion to minor enrichment in $\delta^{34}S$ (-2.7‰ to 1.2‰). Fluids that crystallized schorl had a high boron concentration. The fluid inclusion and sulfur isotope data, high Al concentration for first stage quartz veins, and sufficient boron to generate schorl suggest these early hydrothermal fluids had a magmatic origin. The initial magmatic fluids mixed with an influx of heated meteoric fluids.

The hydrothermal fluids that developed the Oro Fino veins may have originated from both a magmatic and meteoric source. Epithermal systems in volcanic arcs have deep convective circulating meteoric water that mixes with magmatic waters from an intrusive source (Simons and others, 2005). Mixing of heated meteoric water with a low-salinity, CO_2-enriched mag-

matic water in the Oro Fino hydrothermal system may have kept fluid salinities low, which is represented by the large population of 0 to 6 wt% NaCl eq fluid inclusions (fig. 23). The population of inclusions from 7 to 16 wt% NaCl eq and 23 to 37 wt% NaCl eq could have been produced by boiling events from a single fluid. Water vapor as steam driven from the hydrothermal fluids during boiling will increase salinity by producing a concentration of salts in the remaining fluid. The presence of type II inclusions with vapor exceeding 70 vol% indicate steam was being generated during boiling. Boiling of the hydrothermal fluid also drove CO_2 out of the hydrothermal system, producing a CO_2-free brine trapped in the fluid inclusions.

Boiling and mixing with meteoric fluids caused the magmatic hydrothermal fluids to evolve into a fluid with lower Al saturation and low to high salinity, and approached a moderately acidic to neutral pH. EMP analysis of a second quartz generation identified by cathodoluminescence (fig. 14) had an Al concentration ranging from 1,888 ppm to 3,835 ppm. The Al composition suggests this quartz crystallized from an Al-saturated aqueous fluid with a moderately acidic to near neutral pH. A third quartz generation (fig. 15) had a variable Al concentration (57–3,441 ppm), indicating fluctuating changes from neutral to acidic conditions. Base metal mineralization took place at the same time the third quartz stage was crystallizing. No detected Al occurs in the fourth quartz stage (figs. 15–17) that crystallized with silver–gold mineralization, suggesting a neutral or basic fluid pH. The shift in pH from acidic to near neutral to basic will lead to the precipitation of sulfide minerals (Reed and Palandri, 2006) found associated with the third and fourth quartz generation.

There is fluid inclusion and physical evidence that boiling was taking place when the third and fourth quartz stages crystallized. Clusters of liquid and vapor fluid inclusions trapped in third stage quartz indicate crystallization from a boiling hydrothermal fluid (Bodnar and others, 1985). Physical evidence for a boiling system are lattice textures found in quartz replacing bladed calcite (fig. 18) and colloform chalcedony (fig. 19; Simmons and Christenson, 1994; Simmons and others, 2005; Moncada and others, 2012). Most calcite in the veins was pseudomorphed by quartz, suggesting a downward boiling front in the hydrothermal system (Simmons and Browne, 2000). Boiling increases the fluid pH by driving CO_2 from the hydrothermal fluids and increases salinity by vaporizing water into steam (Simmons and others, 2005; Cooke and Simmons, 2000). Carbonate minerals precipitate from boiling near neutral, chloride-hydrothermal fluids due to pH increases from CO_2 loss (Browne and Ellis, 1970). During this stage in the life of the hydrothermal system, boiling was widespread and most mineralization took place, generating base metal sulfides, silver sulfides, and electrum.

Silver minerals occur with a fourth quartz generation identified by cathodoluminescence (fig. 17). This quartz generation is colloform–crustiform banded (fig. 19) and cathodoluminescence reveals a microcrystallized texture (Fig. 15). Banded colloform textures form from chalcedony being deposited during rapid opening of a fracture, causing a pressure decrease and rapid temperature drops caused by boiling or flashing of hydrothermal fluids (Moncada and others, 2012; Henley and Hughes, 2000). The presence of colloform chalcedony indicates the hydrothermal system underwent periods of rapid decompression and temperature drops causing rapid mineralization to take place (Moncada and others, 2012). In the Oro Fino veins, silver minerals and chalcedony occurring together indicate they formed at the same time during rapid mineralization. The presence of chalcedony suggests periods of rapid pressure and temperature drops accompanied with boiling during vein development. In the Guanajuato district, Mexico, colloform texture chalcedony is related to silver and gold mineralization (Moncada and others, 2012).

Buffering of the initial hydrothermal fluid by wall rock reactions could have an impact on the hydrothermal fluid pH. Alteration of the host rock feldspar and development of sericite and illite could shift the pH from strongly acidic to moderately acidic to neutral. Illite is the first clay mineral to form caused by acidic hydrothermal fluids reacting with feldspar at temperatures of 230° to 320°C (Reyes, 1990; Simmons and others, 2005). At lower temperatures, below 230°C, montmorillonite will develop along with kaolinite at temperatures ranging from 120° to 200°C (Simmons and others, 2005).The first quartz stage identified by cathodoluminescence (fig. 14) has an Al concentration ranging from 4,752 to 11,802 ppm, indicating crystallization from an acidic fluid. The acidic hydrothermal fluids that precipitated the first quartz stage also altered the host granite feldspars into clay minerals. A second quartz stage following the first has an Al concentration ranging from 1,888 to 3,835 ppm (fig. 14), indicating crystallization from a less acidic fluid. The change in pH to less acidic conditions may have resulted from a buffering of the hydrothermal fluid by replacing the feldspars with clay minerals.

Sulfur isotopes show an enrichment in $\delta^{34}S$ (3.6‰ to 8.5‰) averaging 6.9‰, suggesting the veins devel-

oped from a hydrothermal fluid influenced by crustal contamination. An inferred source for the enrichment of $\delta^{34}S$ in the Oro Fino veins could be Proterozoic Belt Supergroup sediments enriched in heavy isotopic sulfur. Diagenetic pyrite from the Newland Formation has an average $\delta^{34}S$ value of 7.6‰ (Lyons and others, 2000), and baryte can have $\delta^{34}S$ values ranging from 13.6‰ to 18.3‰ (Strauss and Schieber, 1990). Hydrothermal fluids from the Revett Formation developed the Spar Lake Cu-Ag-Co deposit. Sulfides precipitated from these hydrothermal fluids have $\delta^{34}S$ values ranging from 3‰ to 23‰, suggesting the $\delta^{34}S$ and metal source was the Revett Formation (Hayes and Einaudi, 1986; Hayes and others, 1989). The Belt Supergroup underlies the Boulder Batholith and Oro Fino mining district (Harrison, 1972), and could have served as a source of heavy isotopic sulfur and metals found in the Oro Fino veins. In comparison, Field and others (2005) argued Proterozoic Belt Supergroup sediments are the source of heavy isotopic sulfur for pre-Main stage veins in the Butte mining district.

Near the end of the hydrothermal system, salinities and temperatures of the aqueous fluids dropped. Fluid inclusions trapped in baryte, fluorite, and quartz that crystallized during the final stage of hydrothermal activity have low salinities (0.0–2.4 wt% NaCl equiv.), averaging 0.65 wt% NaCl equiv., and low Th (130º–190ºC), averaging 168ºC. The low salinity and temperatures suggest an influx of a low-salinity and low-temperature fluid into the hydrothermal system that may have had a meteoric origin near the close of mineralization.

Schorl Genesis

Tourmaline is relatively common in epithermal silver–gold veins within the Boulder Batholith (Cox, 2015; Sillitoe and others, 1985). Schorl identified at isolated locations (16–21, 34–35, 55–56, and 77–79, fig. 2) in the epithermal veins of the Oro Fino mining district occurs as needles included in vein quartz, attached to the altered granite and aplite host rocks, and fills open spaces as black crystalline masses in brecciated quartz and host rock. Schorl crystallized early during vein development in conjunction with silica host rock alteration. Early magmatic acidic fluids containing sufficient boron to crystallize schorl reacted with the granite and aplite host rock, generating schorl and quartz with sericite at the contact between the host rock and quartz veins.

Within the Oro Fino veins, schorl occurs in isolated locations due to restricted geochemical condi-

tions required for tourmaline precipitation. Restricted geochemical conditions consisted of sufficient boron to precipitate schorl and high Al and Na saturation (von Goerne and others, 2001). The early hydrothermal fluids were saturated in Al determined by EMP analysis of first stage quartz veinlets identified by cathodoluminescence (fig. 14) as having an acidic pH, and sufficient boron to precipitate schorl.

The early hydrothermal fluids that precipitated schorl in the Oro Fino veins may have originated from a magma source enriched in boron that assimilated marine sediments (London and others, 2002). The magma source for the LCVF suggested by Dudás and others (2010) is partially melted Proterozoic crustal rocks and lithospheric mantle. Proterozoic Belt Supergroup formations are known to contain tourmalinites (Beaty and others, 1988; Slack, 1993), suggesting a B enrichment in these formations, which could have been passed to partial melts in the LCVF and then to magmatic-hydrothermal fluid.

Vein Genesis

The veins exposed on the surface in the Oro Fino district are apparently the lower section of an epithermal system that formed about 0.8 km below the surface, as indicated by pressure determined from measurements of fluid inclusions formed in a boiling fluid (fig. 21). Boiling is further indicated by bladed calcite, lattice-textured quartz (fig. 25), and adularia, which are produced by boiling low-salinity near neutral pH fluids (Simmons and Browne, 2000). Subsurface boiling and a retreating boiling front generate quartz pseudomorphs after bladed calcite (fig. 18; Simmons and Browne, 2000).

Boiling occurs 1,500 to 1,800 m below the water table in active hydrothermal systems in New Zealand (Simmons and Browne, 2000; Hedenquist, 1990). Fluctuations in the elevation of the regional water table may control the vertical position of boiling in the epithermal environment by changing the hydrostatic pressure gradient (Simmons, and others, 2005). A rapid fall in the water table causing a hydrostatic pressure drop can trigger hydrothermal eruptions, brecciation, and precious metal mineralization, and a slow drop in the water table caused by uplift can result in telescoped mineralization and alteration (Simmons and others, 2005). Fluctuations in the water table elevation could have changed the vertical distribution of ores and alteration assemblages of the Oro Fino veins. In epithermal systems with a dropping water table, cooler mineral assemblages (precious metals) can be overprinted on hotter mineral assemblages

Figure 25. Top photograph, quartz showing lattice texture (Champion mine, location 1-3, fig. 2). Bottom photograph, compacted bladed calcite (location 58-60, fig. 2). Both textures caused by boiling events.

(base metals), resulting in telescoped mineralization (Simmons and others, 2005). A retreating paleo water table may have occurred in the Oro Fino veins, causing the silver–gold stage to overprint on the base metal stage (figs. 10C,D,F).

Geologic Model

The Oro Fino mining district hosted by the Butte Granite developed during back arc magmatism that erupted the Eocene Lowland Creek volcanic field (LCVF). The LCVF erupted in three cycles starting with rhyolites at the base, middle dacites, and ending with andesites (Dudás and others, 2010), representing a reverse sequence of bimodal volcanism. Age dating of the alteration along the Oro Fino veins shows that mineralization took place ~3.3 Ma after the late andesite eruption phase.

Low to intermediate sulfidation epithermal veins, such as those in the Oro Fino mining district, form in arc terranes when extensional tectonism is advanced (Sillitoe and Hendenquist, 2003). The LCVF erupted in a half graben formed from Laramide Eocene extension (Scarberry and others, 2015; Dudàs and others, 2010). The veins developed near the west margin of the caldera and the caldera could plausibly have contained a resurgent magma body (e.g., Hayba and others, 1985; Lipman and others, 1976).

Exploration Potential

Elliott and others (1993) gave the northeastern part of the Oro Fino district a moderate to high potential for undiscovered porphyry and stockwork copper–molybdenum deposits, and disseminated/stockwork gold and silver deposits. Their assessment was based on a computer model from the compilation of past geologic investigations and studies consisting of geochemistry, geophysics, and geologic modeling and examination of mines and prospects. A magnetic high in the district reported by Hanna and others (1994) represents the Butte Granite host rock. Elliott and others (1993) gave the district a high to moderate potential for the occurrence of porphyry and stockwork deposits.

It is inferred that a porphyry system underlies the Oro Fino veins and was a fluid source for the epithermal veins. Sillitoe (2010) suggests intermediate sulfidation vein systems can be peripheral or overlie porphyry deposits. Since the Oro Fino veins have features related to both low and intermediate sulfidation epithermal veins, they could overlie or are peripheral to a deep-seated porphyry deposit. Deep geophysical surveys within and adjacent to the district will be required to locate potential drill targets underlying or hosted by the Butte Granite.

In addition to a porphyry system, the veins themselves can be exploration targets. Epithermal veins are highly variable in form caused by variations in vein permeability and structural controls of the hydrothermal fluids (Hedenquist and others, 2000). The past producing mines were developed on silver–gold, base metal bonanza ore shoots with barren sections of quartz veins between the shoots. It is possible additional ore shoots can occur along strike and at depth in the past producing mines. At depth, below the silver–gold mineralization, a base metal horizon could be present that developed from a retreating boiling front.

There are a number of veins in the district that were not fully developed into operating mines. These veins were explored by shallow prospect pits and shafts, and are inferred to extend beyond these known exposures. Inferred locations for these vein extensions were mapped (plate 1 and fig. 2). Exploration for additional ore shoots in the undeveloped veins would be difficult due to soil and forest cover and would require a detailed geophysical survey to locate veins and possible drill targets. On completion of a geophysical survey, precise drilling targeting geophysical anomalies would be needed to confirm the presence of ore shoots.

ACKNOWLEDGMENTS

REFERENCES

Acosta, M.D., Reed, M.H., and Watkins, J.M., 2018, Cathodoluminescent quartz textures reveal importance of recrystallization in veins formed in the Butte porphyry Cu-Mo deposit, Scarberry, K.C., and Barth, S., Proceedings, Montana Mining and Minerals Symposium 2018 technical papers and abstracts: Montana Bureau of Mines and Geology Special Publication 120, p. 121–125.

Audétat, A., Garbe-Schönberg, D., Kronz, A., Pettke, T., Rusk, B., Donovan, J.J., and Lowers, H.A., 2015, Characterization of a natural quartz crystal as a reference material for microanalytical determination of Ti, Al, Li, Fe, Mn, Ga and Ge: Geostandards and Geoanalytical Research, v. 39, p. 171–184.

Beaty, D.W., Hahn, G.A., and Threlkeld, W.E., 1988, Field, isotopic, and chemical studies of tourmaline- bearing rocks in the Belt-Purcell Supergroup: Genetic constraints and exploration significance for Sullivan type ore deposits: Canadian Journal of Earth Science, v. 25, p. 392–402.

Berg, R.B., 2007, Sapphires in the Butte-Deer Lodge area, Montana: Montana Bureau of Mines and Geology Bulletin 134, 59 p.

Berger, B.R., Hildenbrand, T.G., and O'Neill, J.M., 2011, Control of Precambrian basement deformation zones on emplacement of the Laramide Boulder Batholith and Butte mining district, Montana, United States: U.S. Geological Survey Scientific Investigations Report 2011-5016, 29 p.

Berkenbosch, H.A., de Ronde, C.E.J., Gemmell, J.B., McNeill, A.W., and Goemann, K., 2012, Mineralogy and formation of black smoker chimneys from Brothers submarine volcano, Kermadec arc: Economic Geology, v. 107, p. 1613–1633.

Bodnar, R.J., Reynolds, T.J., and Kuehn, C.A., 1985, Fluid inclusion systematics in epithermal systems, Berger, B.R. and Bethke, P.M., eds.: Geology and geochemistry of epithermal systems: Reviews in Economic Geology v. 2, p. 73–97.

Browne, P.R.L., and Ellis, A.J., 1970, The Ohaki-Broadlands hydrothermal area New Zealand: Mineralogy and related geochemistry: American Journal of Science, v. 269, p. 97–131.

Cooke, D.R., and Simmons, S.F., 2000, Characteristics and genesis of epithermal gold deposits, Hagemann, S.G., and Brown, P.E., eds., Gold in 2000: Reviews in Economic Geology, v. 13, p. 221–224.

Cox, B.E., 2015, Boron minerals of western Montana—Occurrences and ore deposit models, 2015 Mining and Minerals Symposium: Montana Bureau of Mines and Geology Open-File Report 669, p. 34–46.

Darling, R.S., 1991, An extended equation to calculate NaCl contents from final clathrate melting temperatures in H_2O-CO_2-NaCl fluid inclusions: Implications for P-T isochore locations: Geochimica et Cosmochimica Acta, v. 55, p. 3869–3871.

Derkey, R.E., Watson, M., Bartholomew, M.J., Stickney, M.C., and Downey, P.J., 2004, Geologic map of the Deer Lodge 15' quadrangle, southwest Montana, revised May 2004: Montana Bureau of Mines and Geology Open-File Report 271, 2 sheets, scale 1:48,000.

Dudás, F.O., Ispolatov, V.O., Harlan, S.S., and Snee, L.W., 2010, 40Ar/39Ar geochronology and geochemical reconnaissance of the Eocene Lowland Creek volcanic field, west-central Montana: Journal of Geology, v. 118, p. 295–304.

Elliott, J.E., Wallace, C.A.., Lee, G.K., Antweiler, J.C., Lidke, D.J., Rowan, L.C., Hanna, W.F., Trautwein, C.M., Dwyer, J.L., and Moll, S.H., 1993, Maps showing mineral resource assessment for porphyry and stockwork deposits of copper, molybdenum, and tungsten and for stockwork and disseminated deposits of gold and silver in the Butte 1o X 2o quadrangle, Montana: U.S. Geological Survey Miscellaneous Investigations Series Map I-2050-F, scale 1:250,000 and 1:500,000, 30 p.

Ewers, G.R., and Keays, R.R., 1977, Volatile and precious metal zoning in the Broadlands geothermal field, New Zealand: Economic Geology, v. 72, p. 1337–1354.

Feely, T.C., 2003, Origin and tectonic implications of across-strike geochemical variations in the Eocene Absaroka Volcanic Province, United States: Journal of Geology, v. 111, p. 329–346.

Field, C.W., Zhang, L., Dilles, J.H., Rye, R.O., and Reed, M.H., 2005, Sulfur and oxygen isotopic record in sulfate and sulfide minerals of early, deep, pre-main stage porphyry Cu-Mo and late main stage base-metal mineral deposits, Butte district, Montana: Chemical Geology, v. 215, p. 61–93.

Fisher, J.R., 1976, The volumetric properties of H_2O—A graphical portrayal: Journal of Research, U.S. Geological Survey, v. 4, no. 2, p. 189–193.

Foster, Fess, 1987, Epithermal precious metal systems associated with an Eocene cauldron: Lowland Creek volcanic field, southwestern Montana,

Berg, R.B., and Breuninger R.H., eds.: Guidebook of the Helena area, west-central Montana: Montana Bureau of Mines and Geology Special Publication 95, p. 53–54.

Fouquet, Y., Stackelberg, U.V., Charlou, J.L., Erzinger, J., Herzig, P.M., Mühe, R., and Wiedicke, M., 1993, Metallogenesis in back-arc environments: The Lau basin example: Economic Geology, v. 88, p. 2154–2181.

Grant, J.A., 2005, Isocon analysis: A brief review of the method and applications: Physics and Chemistry of the Earth, v. 30, p. 997–1004.

Hanna, W.F., Hassemer, J.H., Elliott, J.E., Wallace, C.A., and Snyder, S.L., 1994, Maps showing gravity and aeromagnetic anomalies in the Butte 1o X 2o quadrangle, Montana: U.S. Geological Survey Miscellaneous Investigations Series Map I-2050-I, scale 1:250,000 and 1:500,000, 35 p.

Hargrave, P.A., 1990, Geology of the Browns Gulch and Flume Gulch area, Deer Lodge, Jefferson and Silver Bow Counties, Montana: Butte, Montana Technological University, M.S. thesis, 95 p., scale 1:24,000.

Hargrave, P.A., and Berg, R.B., 2013, Geologic map pf the Lockhart Meadows 7.5' quadrangle, west central Montana: Montana Bureau of Mines and Geology Open-File Report 629, 1 sheet, scale 1:24,000.

Harrison, J.E., 1972, Precambrian Belt Basin of northwestern United States: Its geometry, sedimentation, and copper occurrences: Geological Society of America Bulletin, v. 83, p. 1215–1240.

Hayba, D.O., Bethke, P.M., Heald. P., and Foley, N.K., 1985, Geologic, mineralogic, and geochemical characteristics of volcanic-hosted epithermal precious-metal deposits, Berger, B.R., and Bethke, P.M., eds., Geology and geochemistry of epithermal systems: Reviews in Economic Geology, v. 2, p. 129–167.

Hayes, T.S., and Einaudi, M.T., 1986, Genesis of the Spar Lake strata-bound copper–silver deposit, Montana: Part I: Controls inherited from sedimentation diagenesis: Economic Geology, v. 81, p. 1899–1931.

Hayes, T.S., Rye, R.O., Whelan, J.F., and Landis, G.P., 1989, Geology and sulfur isotope geothermometry of the Spar Lake strata-bound Cu-Ag deposit in the Belt Supergroup, Montana, Boyle, R.W., Brown, A.C., Jowett, E.C., and Kirkham, R.V., eds.: Sediment-hosted strata-bound copper Deposits: Geological Association of Canada Special Paper, v. 36, p. 319–338.

Hedenquist, J.W., 1990, The thermal and geochemical structure of Broadlands-Ohaaki geothermal system, New Zealand: Geothermics, v. 19, p. 151–185.

Hedenquist, J.W., Arribas, R.A., and Gonzalez-Urien, E., 2000, Exploration for epithermal gold Deposits, Hagemann, S.G., and Brown, P.E., eds., Gold in 2000: Reviews in Economic Geology, v. 13, p. 245–277.

Henley, R.W., and Hughes, G.O., 2000, Underground fumaroles: "Excess heat" effects in vein formation: Economic Geology, v. 95, p. 453–466.

Houston, R.A., and Dilles, J.H., 2013, Structural geologic evolution of the Butte district, Montana: Economic Geology, v. 108, p. 1397–1424.

Huang, R., and Audétat, A., 2012, The titanium-in-quartz (TitaniQ) thermobarometer: A critical examination and re-calibration: Geochimica et Cosmochimica Acta, v. 84, p. 75–89.

Kennedy, A.K., Wotzlaw, J.F., Schaltegger, U., Crowley, J.L., and Schmitz, M., 2014, Eocene zircon reference material for microanalysis of U-Th-Pb isotopes and trace elements: Canadian Mineralogist, v. 52, p. 409–421.

Klepper, M.R., Weeks, R.A., and Ruppel, E.T., 1957, Geology of the southern Elkhorn Mountains, Jefferson and Broadwater Counties, Montana: U.S. Geological Survey Professional Paper 292, 82 p.

Kuwatani, T., Yoshida, K., Ueki, K., Oyanagi, R., Uno, M., and Akaho, S., 2020, Sparse isocon analysis: A data-driven approach for material transfer estimation: Chemical Geology, v. 532, article 119345, in progress.

Large, R.R., Gemmell, J.B., and Paulick, H., 2001, The alteration box plot: A simple approach to understanding the relationship between alteration mineralogy and lithogeochemistry associated with volcanic-hosted massive sulfide deposits: Economic Geology, v. 96, p. 957–971.

Lipman, W.P., Fisher, F.S., Mehnert, H.H., Naeser, C.W., Luedke, R.G., and Steven, T.A., 1976, Multiple ages of mid-Tertiary mineralization and alteration in the western San Juan Mountains, Colorado: Economic Geology, v. 71, p. 571–588.

London, D., Morgan VI, G.B., and Wolf, M.B., 2002, Boron in granitic rocks and their contact aureoles, Grew, E.S., and Anovitz, L.M., eds.: Boron mineralogy, petrology and geochemistry: Reviews in

Mineralogy, Mineralogical Society of America, v. 33, p. 299–330.

Lonn, J.D., and Elliott, C., 2010, A walking tour of the Eocene Anaconda detachment fault on Stucky Ridge near Anaconda, Montana: Northwest Geology, v. 39, p. 81–90.

Lund, K., Aleinikoff, J.N., Kunk, M.J., Unruh, D.M., Zeihen, G.D., Hodges, W.C., Du Bray, E.A., and O'Neill, J.M., 2002, SHRIMP U-Pb and 40Ar/39Ar age constraints for relating plutonism and mineralization in the Boulder Batholith region, Montana: Economic Geology, v. 97, p. 241–267.

Lynch, J.V.G., Longstaffe, F.J., and Nesbitt, B.E., 1990, Stable isotopic and fluid inclusion indications of large-scale hydrothermal paleoflow, boiling, and fluid mixing in the Keno Hill Ag-Pb-Zn, Yukon Territory, Canada: Geochemica et Cosmochimica Acta, v 54, p. 1045–1059.

Lyons, T.W., Luepke, J.J., Madeline, E.S., and Zieg, G.A., 2000, Sulfur geochemical constraints on Mesoproterozoic restricted marine deposition: Lower Belt Supergroup, northwestern United States: Geochimica et Cosmochimica Acta v. 64, p. 427–437.

Mahoney, J.B., Pignotta, G.S., Ihinger, P.D., Wittkop, C., Balgord, E.A., Potter, J.J., and Leistikow, A., 2015, Geologic relationships in the northern Helena salient, Montana: Geology of the Elliston region: Northwest Geology, v. 44, p. 109–135.

Moncada, D., Mutchler, S., Nieto, A., Reynolds, T.J., Rimstidt, J.D., and Bodnar, R.J., 2012, Mineral textures and fluid inclusion petrography of the epithermal Ag-Au deposits at Guanajuato, Mexico: Application to exploration: Journal of Geochemical Exploration, v. 114, p. 20–35.

Mosier, D.L., Sato, T., Page, N.J., Singer, D.A., and Berger, B.R., 1987, Descriptive model of Creede epithermal veins, Cox, D.P., and Singer, D.A., eds.: Mineral deposit models: U.S. Geological Survey Bulletin 1693, p. 145–149.

Mosolf, J.G., 2015, Geologic field guide to the Tertiary volcanic rocks in the Elliston 30' X 60' quadrangle, west-central Montana: Northwest Geology, v. 44, p. 213–231.

Pardee, J.T., and Schrader, F.C., 1933, Metalliferous deposits of the greater Helena mining region, Montana: U.S. Geological Survey Bulletin 842, 318 p.

Portner, R.A., Hendrix, M.S., Stalker, J.C., Miggins, D.P., and Sheriff, S.D., 2011, Sedimentary response to orogenic exhumation in the Northern Rocky Mountain Basin and Range province, Flint Creek basin, west-central Montana: Canadian Journal of Earth Sciences, v. 48, p. 1131–1153.

Reed, M.A., and Palandri, J., 2006, Sulfide mineral precipitation from hydrothermal fluids, Vaughan, D.J., ed., Sulfide mineralogy and geochemistry: Geochemical Society, Mineralogical Society of America, Reviews in mineralogy and geochemistry, v. 61, p. 609–631.

Reyes, A.G., 1990, Petrology of Philippine geothermal systems and the application of alteration mineralogy to their assessment: Journal of Volcanology and Geothermal Research, v. 43, p. 279–309.

Reynolds, M.W., 1979, Character and extent of Basin-Range faulting, western Montana and east-central Idaho, Newman, G.W., and Goode, H.D., eds.: Rocky Mountain Association of Geologists and Utah Geological Association Basin and Range Symposium, Denver, CO, and Great Basin Field Conference, p. 185–193.

Rivera, T.A., Storey, M., Schmitz, M.D., and Crowley, J.L., 2013, Age intercalibration of 40Ar/39Ar sanidine and chemically distinct U/Pb zircon populations from Alder Creek Rhyolite Quaternary geochronology standard: Chemical Geology, v. 345, p. 87–98.

Roedder, Edwin, 1984, Fluid inclusions: Mineralogical Society of America, Reviews in Mineralogy, v. 12, 646 p.

Rusk, B.G., Lowers, H.A., and Reed, M.H., 2008, Trace elements in hydrothermal quartz: Relationships to cathodoluminescent textures and insights into vein formation: Geology, v. 36, p. 547–550.

Rusk, B.G., Reed, M.H., Dilles, J.H., and Kent, A.J.R., 2006, Intensity of quartz cathodoluminescence and trace-element content in quartz from the porphyry copper deposit at Butte, Montana: American Mineralogist, v. 91, p. 1300–1312.

Rutland, C., Smedes, H., Tilling, R., and Greenwood, W., 1989, Volcanism and plutonism at shallow crustal levels: The Elkhorn Mountains Volcanics and the Boulder Batholith, southwestern Montana, Henshaw, P., ed.: Volcanism and plutonism of western North America; Volume 2, Cordilleran volcanism, plutonism, and magma generation at various crustal levels, Montana and Idaho, Field trips for the 28th International Geological Congress: American Geophysical Union, Monograph, p. 16–31.

Scarberry, K.C., 2016, Geologic map of the Sugarloaf Mountain 7.5' quadrangle, Deer Lodge, Jefferson, and Powell Counties, MT: Montana Bureau of Mines and Geology Open-File Report 674, scale 1:24,000.

Scarberry, K.C., and Smith, M.G., 2014, Eocene volcanic stratigraphy and Tertiary fault geometry of the southern Deer Lodge Valley, SW Montana: Geological Society of America Abstracts with Programs, v. 46, issue 5, no. 72.

Scarberry, K.C., Korzeb, S.L., and Smith, M.G., 2015, Origin of Eocene volcanic rocks at the south end of the Deer Lodge Valley, Montana, Mosolf, J., and McDonald, C., eds.: 40th annual field conference, geology of the Elliston area, Montana and other papers: Northwest Geology, v. 44, p. 201–212.

Scarberry, K.C., Kallio, I.M., Olson III, N., Dilles, J.H., Older, C.W., Horton, T., and English, A.R., 2016, Large-volume pyroclastic deposits along the eastern edge of the Boulder Batholith, southwestern Montana: Geological Society of America Abstracts with Programs, v. 48, issue 4, abstract no. 21-3.

Silberman, M.L., and Berger, B.R., 1985, Relationship of trace-element patterns to alteration and morphology in epithermal precious-metal deposits, Berger, B.R., and Bethke, P.M., eds.: Geology and geochemistry of epithermal systems: Reviews in Economic Geology, v. 2, p. 203–232.

Sillitoe, R.H., 2010, Porphyry copper systems: Economic Geology, v. 105, p. 3–41.

Sillitoe, R.H., Grauberger, G.L., and Elliott, J.E., 1985, A diatreme-hosted gold deposit at Montana Tunnels, Montana: Economic Geology v. 80, p. 1707–1721.

Sillitoe, R.H., and Hedenquist, J.W., 2003, Linkages between volcanotectonic settings, ore-fluid compositions, and epithermal precious metal deposits, Simmons, S.F., and Graham, I eds.: Volcanic, geothermal, and ore-forming fluids: Rulers and witnesses of processes within the earth: Society of Economic Geologists Special Publication 10, p. 315–343.

Simmons, S.F., Brown, K.F., and Tutolo, B.M., 2016, Hydrothermal transport of Ag, Au, Cu, Pb, Te, Zn, and other metals and metalloids in New Zealand geothermal systems: Spatial patterns, fluid- mineral equilibria, and implications for epithermal mineralization: Economic Geology, v. 111, p. 589–618.

Appendix A

Complete ICP-MS analytical results for altered and unaltered granite and aplite. Analysis conducted by ALS Minerals Inc. ALS analytical code ME-MS 61 was selected for trace element analysis. Results are in parts per million (ppm), or weight percent (%). Gold was not analyzed in all samples. NA, not analyzed; ser-arg, sericitic-argillic alteration.

Sample No.	Granite Alteration	Au ppm	Ag ppm	Al %	As ppm	Ba ppm	Be ppm	Bi ppm	Ca %	Cd ppm	Ce ppm	Co ppm	Cr ppm
OF-7	Silicic	NA	12.4	2.37	32.4	160	1.74	0.07	0.05	0.02	11.05	1.2	54
OF-11	Silicic	NA	24.5	3.63	37.3	420	0.98	0.07	0.04	<0.02	68.5	0.6	18
OF-14	Silicic	0.030	6.63	3.70	13.2	100	1.57	5.11	0.08	0.10	34.9	1.5	33
OF-22	Unaltered	NA	1.35	7.51	5.1	700	1.70	0.07	2.59	0.04	68.2	12.3	29
OF-31	Ser-arg	NA	3.35	7.44	56.5	140	1.51	0.06	0.08	<0.02	40.9	1.7	25
OF-36	Silicic	0.002	0.75	1.66	8.7	120	1.57	0.63	0.08	0.05	24.1	2.8	40
OF-38	Unaltered	NA	0.27	8.02	2.3	970	1.78	0.05	2.64	0.03	74.5	9.8	18
OF-40	Silicic	NA	0.96	4.99	9.2	300	1.54	0.14	0.15	0.03	45.1	2.8	21
OF-42	Silicic	NA	22.9	4.28	218	110	1.10	0.08	0.02	0.02	40.9	2.6	32
OF-60	Unaltered	NA	0.14	7.32	2.0	820	1.96	0.06	2.83	0.05	65.1	10.4	25
OF-65	Ser-arg	NA	1.07	7.90	103.0	170	0.69	0.41	0.05	<0.02	31.4	8.1	30

Sample No.	Granite Alteration	Cs ppm	Cu ppm	Fe %	Ga ppm	Ge ppm	Hf ppm	In ppm	K %	La ppm	Li ppm	Mg %	Mn ppm
OF-7	Silicic	28.3	7.1	0.66	6.29	0.16	0.5	0.009	1.22	5.6	148.0	0.14	38
OF-11	Silicic	10.05	7.6	1.17	6.53	0.21	0.6	0.009	3.78	39.0	90.7	0.09	40
OF-14	Silicic	11.25	9.6	2.69	9.57	0.15	0.3	0.098	0.90	18.6	18.1	0.41	84
OF-22	Unaltered	6.61	36.0	3.56	17.40	0.20	0.4	0.045	3.22	34.3	39.0	1.10	502
OF-31	Ser-arg	20.7	4.1	0.86	21.8	0.18	1.8	0.023	3.15	23.5	36.2	0.16	57
OF-36	Silicic	8.67	31.3	1.28	4.48	0.11	0.1	0.018	0.72	12.5	101.0	0.08	257
OF-38	Unaltered	5.26	22.7	3.46	18.20	0.19	0.6	0.034	3.33	39.5	29.9	0.96	669
OF-40	Silicic	17.50	31.9	0.87	11.45	0.13	0.4	0.015	2.55	27.9	81.5	0.17	75
OF-42	Silicic	25.8	12.4	1.47	11.75	<0.05	0.4	0.017	2.05	22.4	60.2	0.21	45
OF-60	Unaltered	6.60	19.3	3.44	17.30	0.11	0.7	0.031	3.42	33.2	30.7	1.00	579
OF-65	Ser-arg	33.7	9.6	1.97	18.35	0.06	0.4	0.025	3.45	16.6	17.1	0.19	73

Sample No.	Granite Alteration	Mo ppm	Na %	Nb ppm	Ni ppm	P ppm	Pb ppm	Rb ppm	Re ppm	S %	Sb ppm	Sc ppm	Se ppm
OF-7	Silicic	18.85	0.02	2.2	4.4	70	16.5	121.0	<0.002	0.32	15.80	2.6	<1
OF-11	Silicic	3.05	0.12	5.3	1.5	290	18.7	171.0	<0.002	0.05	10.90	2.1	1
OF-14	Silicic	6.49	0.14	3.5	2.5	550	11.6	50.6	<0.002	0.21	46.5	5.4	3
OF-22	Unaltered	3.77	2.07	14.6	10.3	800	17.8	117.0	<0.002	0.04	1.12	11.9	1
OF-31	Ser-arg	1.88	0.05	7.4	3.1	190	18.7	259	<0.002	0.05	9.85	3.8	<1
OF-36	Silicic	7.56	0.05	2.0	2.6	140	7.3	45.9	<0.002	0.02	31.3	2.1	1
OF-38	Unaltered	1.16	2.36	14.8	6.2	950	14.4	125.0	<0.002	0.01	0.27	8.6	1
OF-40	Silicic	2.14	0.06	7.5	2.0	320	22.4	153.5	<0.002	0.01	13.25	3.2	1
OF-42	Silicic	10.05	0.02	8.4	3.3	80	12.7	172.5	<0.002	1.10	28.0	6.5	<1
OF-60	Unaltered	3.33	2.18	13.4	7.9	840	14.2	117.5	<0.002	0.04	0.33	10.1	1
OF-65	Ser-arg	2.95	0.05	13.5	10.4	80	8.1	248	<0.002	1.86	10.45	10.4	1

Sample No.	Granite Alteration	Sn ppm	Sr ppm	Ta ppm	Te ppm	Th ppm	Ti %	Tl ppm	U ppm	V ppm	W ppm	Y ppm	Zn ppm	Zr ppm
OF-7	Silicic	0.5	34.7	0.12	<0.05	1.74	0.071	1.78	1.0	38	1.5	2.3	14	15.8
OF-11	Silicic	0.5	84.6	0.57	<0.05	11.60	0.079	1.57	2.5	18	3.4	7.5	6	13.2
OF-14	Silicic	3.8	64.5	0.26	1.63	9.63	0.093	0.48	4.5	52	14.2	5.2	24	7.7
OF-22	Unaltered	1.6	456	1.02	<0.05	20.1	0.337	0.75	3.8	103	1.4	19.2	57	6.5
OF-31	Ser-arg	1.3	32.0	0.50	<0.05	8.24	0.195	3.79	3.3	28	4.9	6.0	12	51.9
OF-36	Silicic	0.5	37.6	0.16	<0.05	4.39	0.040	0.39	8.6	21	6.1	10.9	27	3.1
OF-38	Unaltered	1.5	613	1.13	<0.05	18.10	0.285	0.67	3.5	82	1.1	18.5	55	10.8
OF-40	Silicic	0.06	43.6	0.68	<0.05	15.00	0.103	1.23	5.6	28	8.2	8.2	29	7.5
OF-42	Silicic	1.2	17.8	0.71	<0.05	9.66	0.194	1.97	2.7	55	18.9	6.7	13	8.8
OF-60	Unaltered	1.5	508	1.07	<0.05	17.05	0.313	0.78	2.7	95	1.3	17.4	45	11.3
OF-65	Ser-arg	2.2	7.7	0.97	<0.05	9.84	0.380	3.95	1.4	107	8.4	5.1	8	7.2

Sample No.	Aplite Alteration	Au ppm	Ag ppm	Al %	As ppm	Ba ppm	Be ppm	Bi ppm	Ca %	Cd ppm	Ce ppm	Co ppm	Cr ppm
OF-35	Argillic	NA	1.77	6.37	41.9	100	1.04	0.92	0.26	0.09	11.25	25.9	48
OF-76	Silicic	NA	4.19	2.74	512	200	2.89	0.05	0.22	0.07	20.4	1.5	25
OF-79	Unaltered	NA	0.16	5.71	3.8	380	1.16	0.08	0.43	0.08	83.5	3.8	20
OF-83	Ser-arg	NA	0.46	5.95	13.90	80	1.29	0.29	0.03	0.54	87.9	0.4	24

Sample No.	Aplite Alteration	Cs ppm	Cu ppm	Fe %	Ga ppm	Ge ppm	Hf ppm	In ppm	K %	La ppm	Li ppm	Mg ppm	Mn ppm
OF-35	Argillic	4.13	5.4	5.68	23.4	0.08	0.2	0.411	0.70	6.4	32.5	1.42	195
OF-76	Silicic	24.4	6.4	1.15	7.59	<0.05	0.2	0.011	1.30	11.1	171.0	0.13	58
OF-79	Unaltered	8.45	48.1	1.51	10.55	0.10	0.7	0.010	5.03	39.1	12.6	0.15	141
OF-83	Ser-arg	8.65	12.2	0.39	11.15	0.12	2.9	0.016	3.88	47.1	60.2	0.02	86

Sample No.	Aplite Alteration	Mo ppm	Na %	Nb ppm	Ni ppm	P ppm	Pb ppm	Rb ppm	Re ppm	S %	Sb ppm	Sc ppm	Se ppm
OF-35	Argillic	5.69	0.62	0.7	9.0	140	55.3	38.1	<0.002	0.28	11.45	7.4	1
OF-76	Silicic	16.80	0.03	3.9	1.7	260	6.1	153.0	<0.002	0.03	28.0	3.6	1
OF-79	Unaltered	1.99	1.32	7.1	4.7	140	21.2	187.0	<0.002	0.15	0.48	2.3	<1
OF-83	Ser-arg	2.17	0.20	14.8	1.2	110	43.9	181.5	<0.002	0.01	6.46	2.0	1

Sample No.	Aplite Alteration	Sn ppm	Sr ppm	Ta ppm	Te ppm	Th ppm	Ti %	Tl ppm	U ppm	V ppm	W ppm	Y ppm	Zn ppm	Zr ppm
OF-35	Argillic	7.3	337	0.14	0.18	11.15	0.075	0.43	6.0	99	3.1	3.4	70	3.1
OF-76	Silicic	0.5	48.7	0.32	<0.05	5.05	0.094	1.84	10.4	32	6.1	9.5	19	4.4
OF-79	Unaltered	0.7	204	0.78	<0.05	36.0	0.094	1.02	4.4	16	2.7	9.1	18	17.2
OF-83	Ser-arg	0.6	44.1	2.38	0.06	54.7	0.067	1.40	8.0	3	4.6	14.3	57	69.4

Appendix B

Trace element results in parts per million (ppm) for vein samples analyzed by four acid digestion and ICP-MS methods. Gold analyzed by fire assay with either ICP-AES or gravimetric finish. Analysis was conducted by ALS Minerals Inc., ALS analytical code ME-MS 61 was selected for trace element analysis and Au-ICP21 was selected for gold analysis.

Sample No.	Mine/Claim/ Prospect	Au ppm	Ag ppm	As ppm	Ba ppm	Bi ppm	Co ppm	Cs ppm	Cu ppm	Li ppm
OF-4	Champion	10.95	3,000	601	420	0.08	4.2	16.25	25.8	98.0
OF-6	Champion	2.29	826	286	70	0.10	4.6	19.15	12.6	97.4
OF-8	Ruby	0.961	277	197.5	170	41.2	28.9	7.16	6.9	68.5
OF-14	Prospect shaft	0.030	6.63	13.2	100	5.11	1.5	11.25	9.6	18.1
OF-19	Prospect adit	0.093	4.31	19.1	20	6.55	97.3	1.54	21.1	19.9
OF-27	Ruby Queen	1.18	984	2,390	120	0.35	1.5	13.20	180	163.5
OF-28	Prospect adit	0.112	17.95	1,010	120	0.08	0.8	14.15	6.7	144.5
OF-33	Banker	0.568	49.4	1,100	260	0.07	3.0	24.5	20.4	88.9
OF-34	Prospect adit	0.168	23.5	391	280	0.31	6.1	15.76	16.7	88.5
OF-36	Bernice	0.002	0.75	8.7	120	0.63	2.8	8.67	31.3	101.0
OF-44	Prospect pit	0.708	26.6	1,210	1,320	0.08	1.1	15.75	119	111.0
OF-46	Silver Queen	0.084	4.91	808	280	0.06	1.0	25.5	18.1	203.0
OF-47	Little Darling	0.178	37.8	150	110	0.19	0.6	17.40	8.2	244.0
OF-48	Little Darling	0.491	88.8	874	330	0.06	3.3	23.4	18.4	140.5
OF-50	Princess shaft	5.64	40.2	33.7	160	4.43	13.7	19.55	3,840	98.8
OF-52	Princess shaft	0.491	115	3,150	160	0.27	3.2	21.8	120.5	138.5
OF-53	Forlorn Hope	6.64	36.1	171.5	50.0	42.0	9.8	3.44	24.0	34.4
OF-55	Prospect pit	0.012	2.48	61.6	90.0	0.36	0.8	3.76	12.8	63.2
OF-57	Prospect pit	0.027	0.45	23.2	150	0.85	17.4	10.30	10.4	64.3
OF-61	Banker	0.064	3.61	123	110	0.76	4.2	13.20	7.6	33.8
OF-62	Banker	1.405	618	160.5	200	0.04	0.6	53.1	27.6	51.6
OF-63	Banker	0.084	7.87	78.2	70.0	0.05	0.6	30.2	4.3	55.7
OF-64	Banker	0.043	25.2	37.5	100	0.16	1.6	20.5	4.6	76.5
OF-66	Prospect pit	0.255	47.6	2,330	200	0.20	1.4	19.85	13.1	122.0
OF-67	Mystery	2.66	1,765	1,190	180	0.06	2.4	17.65	197.5	166.0
OF-70	Mystery	0.058	15.90	146.5	80.0	0.02	1.3	12.20	6.3	150.0
OF-72	Mystery	2.08	587	5,460	100	0.09	2.4	17.65	96.8	176.0
OF-74	Mystery	0.399	79.5	415	130	0.28	0.8	16.25	5.8	239.0
OF-80	Little Darling	0.616	652	930	160	0.16	0.7	10.40	50.0	163.0

Sample No.	Mine/Claim/ Prospect	Mo ppm	Pb ppm	Rb ppm	Sb ppm	Sr ppm	Te ppm	Tl ppm	W ppm	Zn ppm
OF-4	Champion	10.75	251	232	298	71.8	<0.05	4.47	3.2	287
OF-6	Champion	105.5	350	191.5	156.5	21.5	<0.05	2.56	3.5	45
OF-8	Ruby	19.20	129.5	100.5	28.2	31.9	13.80	1.70	5.3	8
OF-14	Prospect shaft	6.49	11.6	50.6	46.5	64.5	1.63	0.48	14.2	24
OF-19	Prospect adit	5.66	29.7	11.5	7.09	25.1	1.78	0.13	1.0	197
OF-27	Ruby Queen	184.5	48.7	60.0	512	27.3	0.11	2.33	2.5	55
OF-28	Prospect adit	14.10	4.9	32.4	99.3	27.7	<0.05	0.64	1.1	9
OF-33	Banker	7.49	35.9	158.0	53.9	57.1	<0.05	2.49	8.3	32
OF-34	Prospect adit	8.77	25.5	67.1	37.7	39.3	<0.05	1.30	7.3	39
OF-36	Bernice	7.56	7.3	45.9	31.3	37.6	<0.05	0.39	6.1	27
OF-44	Prospect pit	116.0	37.9	56.2	123.5	317	0.10	7.73	3.6	49
OF-46	Silver Queen	10.80	6.4	83.6	56.2	32.9	<0.05	1.10	14.5	10
OF-47	Little Darling	87.4	9.9	54.8	41.2	38.7	0.05	0.97	3.2	4
OF-48	Little Darling	105.5	48.3	130.0	68.8	38.8	<0.05	2.60	6.0	40
OF-50	Princess shaft	10.55	28.9	97.0	29.4	101.0	0.09	0.74	3.5	66
OF-52	Princess shaft	238.0	51.7	127.0	177.5	34.2	<0.05	4.34	9.1	41
OF-53	Forlorn Hope	46.3	1,940	26.2	31.9	114.5	0.12	0.66	6.3	129
OF-55	Prospect pit	6.94	80.5	43.8	10.70	149.0	<0.05	0.55	7.2	51
OF-57	Prospect pit	2.77	49.5	84.1	24.3	159.0	0.05	0.77	7.9	63
OF-61	Banker	43.9	286	130.0	35.4	12.3	<0.05	4.51	9.1	134
OF-62	Banker	10.85	67.9	308	116.5	23.3	<0.05	4.21	8.9	28
OF-63	Banker	10.45	84.0	172.5	20.5	14.0	<0.05	2.48	8.2	23
OF-64	Banker	5.31	62.3	109.5	41.8	17.7	<0.05	1.93	2.8	34
OF-66	Prospect pit	18.10	20.1	125.5	48.0	62.0	<0.05	1.77	15.6	9
OF-67	Mystery	345.0	489	107.5	620	33.2	<0.05	2.14	3.6	1,460
OF-70	Mystery	10.50	7.4	54.4	20.3	71.2	<0.05	0.75	4.9	19
OF-72	Mystery	63.2	148.0	71.0	344	23.2	<0.05	1.54	3.3	296
OF-74	Mystery	26.1	11.1	72.9	41.7	37.8	0.05	1.37	2.7	5
OF-80	Little Darling	11.60	94.7	71.2	237	34.4	0.05	1.09	9.7	178

Dump samples of vein sections with potential ore grade analysis. Gold and silver ICP-AES and ICP-MS ppm results calculated to troy oz/t. Conversion factor 1 troy oz/t = 34.3 ppm used in calculations. AN, anomalous concentration but is not considered to be ore grade.

Sample No.	Mine/Claim/ Prospect	Au troy oz/ton	Ag troy oz/ton
OF-4	Champion	0.3	87.5
OF-6	Champion	0.07	24.1
OF-8	Ruby	0.03	8.1
OF-27	Ruby Queen	0.03	28.7
OF-50	Princess shaft	0.16	AN
OF-53	Forlorn Hope	0.19	AN
OF-62	Banker	0.04	18.0
OF-67	Mystery	0.08	51.5
OF-72	Mystery	0.06	17.1

Appendix C

Summary of fluid inclusion data, Tm ice, average melting temperature for ice; Tm halite, homogenization temperature for halite; Tm clath, melt temperature for clathrate; Th, vapor to liquid (l) homogenization temperature; salinity given as equivalent Wt% NaCl. All temperatures given in °C.

Sample No.	Location Coordinates	Host Mineral	Tm Ice	Tm Halite	Tm Clath	Th l	Equivalent Wt% NaCl
OF-3	46.1411.89 N -112.3609.86 W	Quartz	-0.4			217.0	0.70
			-0.4			213.9	0.70
			-0.2			202.5	0.35
			-0.1			182.1	0.18
			0			208.9	0.0
			-0.3			216.2	0.53
			-0.3			215.4	0.53
			-0.4			208.2	0.70
			-0.4			211.6	0.70
			-0.1				0.18
			-0.3				0.53
			-0.2				0.35
			-0.3				0.53
OF-5	46.1404.28 N -112.3640.68 W	Quartz	-0.6			262.3	1.05
			-0.4			257.6	0.70
			-0.4			250.5	0.70
			-0.4			250.5	0.70
			-0.5			246.7	0.87
			-0.5			255.6	0.87
			-0.3				0.53
			-0.5				0.87
			0				0.0
OF-6	46.1404.28 N -112.3640.68 W	Quartz	-0.5			229.5	0.87
						261.4	
						285.6	
			-0.4			239.0	0.70
			-0.2			263.3	0.35
						246.2	
						245.7	
						268.3	
						254.0	
						248.0	
						301.6	
			-0.6			243.8	1.05
OF-7	46.1404.28 N -112.3640.68 W	Quartz	-0.1			202.6	0.18
			-0.4			195.0	0.70
			-0.4			197.2	0.70
			-0.5			193.3	0.87
OF-7	46.1404.28 N -112.3640.68 W	Quartz	-0.3			147.3	0.53
			-0.6			163.2	1.05
			-0.4			183.4	0.70
			-0.4			172.0	0.70
			-0.4			172.0	0.70
			-0.2			177.1	0.35
			0.0			220.3	0.0
			-0.5				0.87
			-0.4				0.70
			0				0

Sample No.	Location Coordinates	Host Mineral	Tm Ice	Tm Halite	Tm Clath	Th I	Equivalent Wt% NaCl
			0				0
			0				0
OF-8	46.1432.87 N -112.3644.67 W	Quartz	-1.8			303.8	3.05
			-1.7			261.5	2.89
			-1.8			291.3	3.05
			-1.3			237.7	2.23
						200.6	
OF-12	46.1422.11 N -112.3625.11 W	Quartz	-3.4			209.8	5.55
			-1.9			215.4	3.21
			-1.9			292.5	3.21
			-1.9			215.3	3.21
			-0.4			219.8	0.70
			0.0			344.7	0.0
			-0.3			189.5	0.53
			-0.3			224.8	0.53
			0.0			221.4	0.0
			-0.2			230.5	0.35
						300.4	
						314.6	
			-1.9				3.21
OF-13	46.1422.11 N -112.3625.11 W	Quartz	-0.2			225.9	0.35
			-0.4			290.5	0.70
			-0.1			193.8	0.18
			-0.3			210.6	0.53
			-0.2			204.6	0.35
			0.0			204.7	0.0
			-0.5			221.6	0.87
			-0.6			196.4	1.05
			-0.5			192.9	0.87
			0.2				0.35
OF-20	46.1434.90 N -112.3649.70 W	Quartz		166.2		318.4	30.35
			-1.6			197.4	2.73
				170.0		338.0	30.50
				177.3		197.1	30.79
OF-20	46.1434.90 N -112.3649.70 W	Quartz		216.0		277.0	32.70
				200.0		237.1	31.87
				216.0		270.0	32.70
				290.5		249.7	37.44
				293.4		272.2	37.66
						342.0	
				166.0		362.7	30.34
						225.7	
				214.6		261.2	32.63
				200.0		271.4	31.87
			-3.6			252.0	5.85
			-5.2				8.13
			-0.5				0.87
OF-27	46.1300.56 N -112. 3734.52 W	Quartz	-0.3			199.5	0.53
			-0.2			182.0	0.35
			0.0			270.4	0.0
			-5.2				8.13
OF-28	46.1317.82 N -112.3731.34 W	Quartz	-0.8			280.8	1.39
			-0.8			280.0	1.39
			-0.7			173.1	1.22
			-0.7			277.7	1.22
			-0.7			165.0	1.22

Sample No.	Location Coordinates	Host Mineral	Tm Ice	Tm Halite	Tm Clath	Th l	Equivalent Wt% NaCl
			-0.6			273.3	1.05
			-0.7			210.5	1.22
			-0.7			268.8	1.22
			-0.7			224.7	1.22
			-0.4				0.70
OF-30	46.1310.00 N -112.3721.29 W	Quartz	-1.1			182.5	1.90
			-1.1			171.5	1.90
			-1.0			183.7	1.73
			-1.4			181.6	2.40
			-1.1			181.5	1.90
			-1.1			180.5	1.90
			-1.2				2.06
OF-32	46.1328.16 N -112.3714.61 W	Quartz	-3.3			222.8	5.40
			-0.6			282.6	1.05
			-0.8			276.1	1.39
			-1.0			284.1	1.73
			-1.4			277.9	2.40
			-1.5			346.5	2.56
OF-33	46.1328.16 N -112.3714.61 W	Quartz	-8.5			229.2	12.30
			-2.0			228.4	3.37
			-5.7			225.6	8.81
						243.9	
OF-33	46.1328.16 N -112.3714.61 W	Quartz				243.8	
						232.8	
						248.9	
						275.8	
			-11.9			229.0	15.99
			-3.2			243.6	5.25
			-8.1			244.3	11.83
			-8.1			238.8	11.83
			-7.5			193.5	11.05
						275.6	
						246.6	
						227.0	
OF-34	46.1217.46 N -112.3729.25 W	Quartz	-0.5			174.3	0.87
			-0.6			147.9	1.05
			-0.6			152.5	1.05
			-0.7			165.5	1.22
			-0.5			149.0	0.87
			-0.7			174.9	1.22
			-0.9			204.5	1.56
			-0.9			172.2	1.56
			-0.9			204.9	1.56
OF-36	46.1435.64 N -112.3229.13 W	Quartz	-8.7			226.6	12.48
			-8.7			175.2	12.48
			-8.2			240.1	11.95
			-8.4			219.0	12.19
			-0.4			213.6	0.70
			-8.1			217.8	11.83
					9.2	442.1	1.64
			-8.2			216.5	11.89
						406.1	
			-0.4			220.2	0.70
OF-42	46.1158.64 N -112.3738.65 W	Quartz	-2.3			250.9	3.85
			-1.2			270.5	2.06
			-1.1			251.1	1.90

Sample No.	Location Coordinates	Host Mineral	Tm Ice	Tm Halite	Tm Clath	Th I	Equivalent Wt% NaCl
			-0.6			253.1	1.05
			-1.1			285.1	1.90
			-7.5			302.5	11.11
			-1.8			255.0	3.05
			-1.4				2.39
			-0.7				1.21
OF-45	46.1208.94 N -112.3738.18 W	Barite				169.7	
						172.2	
						181.5	
						181.7	
OF-45	46.1208.94 N -112.3738.18 W	Barite				172.2	
						169.7	
						181.5	
						181.7	
			0.0			153.0	0.0
			0.0			152.4	0.0
			0.0			154.0	0.0
			0.0			152.6	0.0
			0.0			154.7	0.0
			0.0			154.6	0.0
			0.0			156.2	0.0
						169.3	
						170.8	
						143.4	
						165.1	
						154.3	
						166.0	
						163.7	
						169.1	
OF-55	46.1234.50 N -112.3705.88 W	Quartz		255.5		255.3	35.03
				194.9		255.4	31.62
				203.2		277.5	32.04
				189.0		279.4	31.34
						242.5	
						267.3	
						282.4	
				194.0		280.0	31.58
				264.0		247.8	35.58
						245.9	
						214.3	
OF-67	46.1232.93 N -112.3822.85 W	Quartz	-1.2			223.5	2.06
			-0.9			224.4	1.56
			-0.4			185.1	0.70
			-0.3			210.9	0.53
			-0.3			165.2	0.53
			-0.5			178.7	0.87
			-0.4			182.9	0.70
			-0.4			175.3	0.70
			-0.5			183.8	0.87
			-1.0				1.73
			-1.0				1.73
			-0.4				0.70
			-0.3				0.53
			-1.3				2.23
OF-67	46.1232.93 N -112.3822.85 W	Quartz	-1.3				2.23
			-0.4				0.70

Sample No.	Location Coordinates	Host Mineral	Tm Ice	Tm Halite	Tm Clath	Th l	Equivalent Wt% NaCl
			-0.6				1.05
OF-70	46.1222.53 N -112.3824.37 W	Quartz	-0.2			147.5	0.35
			-0.2			157.0	0.35
			-0.2			153.2	0.35
			-0.1			159.1	0.18
			-0.2			155.9	0.35
			-0.2			157.0	0.35
			-0.2			157.0	0.35
						162.0	
						153.6	
			-0.1				0.18
			0				0.0
			0				0.0
			-0.2				0.35
			-0.2				0.35
			-0.2				0.35
			-0.2				0.35
			-0.1				0.18
			0.0			161.1	0.0
			-0.2			149.9	0.35
			0.0			152.2	0.0
			-0.2			156.9	0.35
			-0.2			129.6	0.35
OF-73	46.1232.12 N -112.3825.55 W	Fluorite				149.8	
						152.3	
						151.2	
						152.6	
						151.1	
						152.3	
						151.2	
						151.2	
						151.9	
						148.6	
						148.6	
						148.6	
						151.2	
						153.1	
						153.1	
OF-75	46.1228.59 N -112.3826.44 W	Fluorite	-0.2			183.0	0.35
			-0.2			178.8	0.35
			-0.2			187.4	0.35
			-0.2			179.1	0.35
OF-75	46.1228.59 N -112.3826.44 W	Fluorite				180.3	
						182.0	
						182.0	
						183.9	
						185.0	
						179.9	
						181.8	
						177.5	
			-0.2			182.5	0.35
			-0.2			184.7	0.35
			-0.2			182.6	0.35
						184.0	
						179.9	
						182.8	

Sample No.	Location Coordinates	Host Mineral	Tm Ice	Tm Halite	Tm Clath	Th l	Equivalent Wt% NaCl
						183.1	
						181.4	
						181.4	
						181.3	
OF-81	46.1213.06 N -112.3830.39 W	Quartz	-1.6			262.4	2.72
			-1.6			268.8	2.72
			-1.9			269.7	3.21
			-2.1			270.7	3.53
			-1.2			253.7	2.06
			-1.9			245.6	3.21
			-1.6			253.3	2.72
			-1.5			263.5	2.56
			-0.7			268.8	1.22
			-2.1				3.53
			-1.4				2.39
OF-82	46.1058.10 N -112.3940.15 W	Quartz	-8.8			278.1	12.71
			-9.3			275.3	13.22
			-4.1			258.7	6.58
			-9.9			314.7	13.33
						274.3	
						255.3	
						274.3	
			-1.6				2.81
			-4.5				7.15
OF-86	46.1355.89 N -112.3602.74 W	Quartz	-2.1				3.53
			-1.3				2.23
			-1.9				3.21
			-1.8				3.05
			-21.6				23.77
			-1.8				3.05
OF-86	46.1355.89 N -112.3602.74 W	Quartz	-12.2				16.24
						252.2	
						187.5	
						237.9	
						240.3	

Appendix D

Summary of sulfur isotope data. Sulfur isotope results are reported in the standard notation $\delta^{34}S‰$ relative to the Canyon Diablo Troilite standard.

Sample No.	Location Coordinates		Mineral Analyzed	$\delta^{34}S$ VCDT Results
OF-1	46.1411.89 N	-112.3609.86 W	Pyrite	5.1
OF-1-1	46.1411.89 N	-112.3609.86 W	Pyrite	8.3
OF-4	46.1404.28 N	-112.3640.68 W	Pyrite	7.6
OF-4-1	46.1404.28 N	-112.3640.68 W	Pyrite	7.3
OF-4-2	46.1404.28 N	-112.3640.68 W	Pyrite	8.1
OF-6	46.1404.28 N	-112.3640.68 W	Pyrite	7.2
OF-8	46.1432.87 N	-112.3644.67 W	Pyrite	-2.3
OF-8-1	46.1432.87 N	-112.3644.67 W	Pyrite	-2.7
OF-12	46.1422.11 N	-112.3625.11 W	Pyrite	6.0
OF-16	46.1442.28 N	-112.3656.51 W	Pyrite	3.6
OF-19	46.1434.90 N	-112.3649.70 W	Pyrite	-2.9
OF-20	46.1434.90 N	-112.3649.70 W	Pyrite	-1.2
OF-24	46.1405.17 N	-112.3589.26 W	Pyrite	8.0
OF-26	46.1300.56 N	-112.3734.52 W	Pyrite	6.9
OF-29	46.1310.00 N	-112.3721.29 W	Pyrite	8.0
OF-33	46.1328.16 N	-112.3714.61 W	Pyrite	8.5
OF-35	46.1217.46 N	-112.3729.25 W	Pyrite	4.1
OF-44	46.1208.94 N	-112.3738.18 W	Pyrite	7.9
OF-49	46.1214.49 N	-112.3828.96 W	Pyrite	7.7
OF-50	46.1219.67 N	-112.3828.96 W	Chalcopyrite	6.5
OF-53	46.1224.59 N	-112.3723.94 W	Pyrite	7.0
OF-54	46.1224.59 N	-112.3723.94 W	Pyrite	7.1
OF-56	46.1234.50 N	-112.3705.88 W	Pyrite	5.5
OF-61	46.1310.00 N	-112.3721.29 W	Pyrite	7.5
OF-61-1	46.1310.00 N	-112.3721.29 W	Pyrite	7.4
OF-67	46.1232.93 N	-112.3822.85 W	Pyrite	8.0
OF-77	46.1145.74 N	-112.3806.00 W	Chalcopyrite	1.2
OF-77	46.1145.74 N	-112.3806.00 W	Pyrite	0.4
OF-86	46.1355.89 N	-112.3602.74 W	Pyrite	5.4